Nano Energy 83 (2021) 105789

Contents lists available at ScienceDirect

Nano Energy

journal homepage: http://www.elsevier.com/locate/nanoen

Review

Polarity in ZnO nanowires: A critical issue for piezotronic and piezoelectric devices

Vincent Consonni [a,*], Alex M. Lord [b]

[a] Univ. Grenoble Alpes, CNRS, Grenoble INP, LMGP, F-38000 Grenoble, France
[b] Centre for NanoHealth, College of Engineering, Swansea University, Swansea SA2 8PP, United Kingdom

ARTICLE INFO

Keywords:
Crystal polarity
ZnO nanowires
Chemical bath deposition
Piezoelectric devices
Piezotronic devices

ABSTRACT

The polar and piezoelectric nature of the wurtzite structure of ZnO nanowires with a high aspect ratio at nanoscale dimensions is of high interest for piezotronic and piezoelectric devices, but a number of issues related to polarity are still open and deserve a particular attention. In this context, chemical bath deposition offers a unique opportunity to select the O- or Zn-polarity of the resultant nanowires and is further compatible with the fabrication processes of flexible devices. The control and use of the polarity in ZnO nanowires grown by chemical bath deposition open a new way to greatly enhance the performance of the related piezotronic and piezoelectric devices. However, polarity as an additional tunable parameter should be considered with care because it has a strong influence on many processes and properties. The present review is intended to report the most important consequences related to the polarity in ZnO nanowires for piezotronic and piezoelectric devices. After introducing the basic principles involving crystal polarity in ZnO, a special emphasis is placed on the effects of polarity on the nucleation and growth mechanisms of ZnO nanowires using chemical bath deposition, defect incorporation and doping, electrical contacts and device properties.

1. Introduction

The wurtzite structure of ZnO belonging to the *6mm* point group confers its piezoelectric and polar character along the <0001> direction (*i.e.*, the so-called *c*-axis). The definition of polarity is related to the direction of the cation-anion bond that is collinear to the *c*-axis. By convention, when the vector starts from a zinc (resp. oxygen) atom to an oxygen (resp. zinc) atom in the tetrahedral environment, the [0001] (resp. $[000\bar{1}]$) direction is Zn- (resp. O-) polar. In ZnO single crystals and epitaxial thin films, the spontaneous polarization field along the *c*-axis has been found to greatly affect surface configuration and reactivity, nucleation and growth mechanisms, defect incorporation and doping, electro-optical properties, contact properties, as well as the performances of the resulting devices [1–3]. In ZnO nanostructures, the influence of crystal polarity is still open to a large extent despite its primary importance [3–5]. A striking example was reported in 2003 by Kong et al. showing that the shape of ZnO nanostructures grown by thermal evaporation can be selected by using the polar character of the structure [6]. The resulting formation of nano-helixes, nano-springs, and nano-rings was revealed [7]. Another important example showed that the chemical reactivity required to form ZnO nanowires (NWs) by thermal evaporation strongly depends on the polarity of the nucleation surfaces [8]. The Zn-polar surfaces were found to be much more reactive than the O-polar surfaces.

Among the wide variety of nanostructures [9,10], NWs or nanorods (NRs), when the NW diameter is larger than 100 nm, exhibit a high aspect ratio at nanoscale dimensions, grow along the piezoelectric and polar *c*-axis, and offer a high capability of integration into real-world devices. They benefit from a large number of attractive properties, including a high crystalline quality, an efficient strain relaxation from the lateral surfaces favorable for heteroepitaxy [11], and possible dielectric and quantum confinements to name a few [12,13]. ZnO NWs have thus been considered as building blocks in a wide variety of devices in the fields of electronics and optoelectronics [14,15], photovoltaics [16], and sensing [17]. In particular, as an abundant, non-toxic compound semiconductor with relatively high piezoelectric coefficients, ZnO NWs further represent a great alternative to lead zirconate titanate films for the development of eco-friendly piezotronic and piezoelectric devices in micro- and nano-technology [18–21]. The shape of ZnO NWs is expected to outperform the conventional ZnO thin films by i) resisting

* Corresponding author.
E-mail address: vincent.consonni@grenoble-inp.fr (V. Consonni).

https://doi.org/10.1016/j.nanoen.2021.105789
Received 16 November 2020; Received in revised form 15 January 2021; Accepted 15 January 2021
Available online 19 January 2021

extremely large elastic strain without plastic strain or fracture, and by taking profit from ii) larger piezoelectric coefficients when the nanoscale diameter is small [22,23] and from iii) surface Fermi level pinning to reduce the screening potential originating from the high density of free charge carriers in their center [24]. These assets are liable to drastically boost the performances of the piezotronic and piezoelectric devices. Additional advantages of using ZnO NWs include higher force-to-displacement sensitivities, low voltage and power, high speed and lightness to name a few [25]. The related piezoelectric nano-generators [26–28] and strain/pressure sensors [29–31] have emerged for a broad range of applications harvesting/detecting the mechanical energy from different sources in the environment such as human motion, vibration, and flowing wind. In this type of devices, the microstructure control appears as a critical issue to improve their overall performance [32]. Flexibility further appears as a major requirement to enhance the electromechanical coupling in the widely-used vertically integrated configuration sandwiching ZnO NWs encapsulated in a polymer between two metallic electrodes [33]. To avoid sophisticated technological processes including transfer processes, the use of flexible substrates has largely been targeted for the fabrication of flexible piezotronic and piezoelectric devices. This in turn limits strongly the number of compatible deposition techniques for the self-assembled growth of ZnO NWs. As such, although ZnO NWs can be grown by a vast number of catalyst-free physical and chemical deposition techniques including thermal evaporation [34,35], pulsed-laser deposition [36,37], chemical vapor deposition [38], spray pyrolysis [39], and metal-organic chemical vapor deposition [40], only the low-temperature wet chemistry methods [41,42] appear as efficient, compatible processes for the fabrication of flexible piezotronic and piezoelectric devices.

The chemical bath deposition (CBD) technique first reported by Vayssières et al. has received an overwhelming interest in the last two decades [41]. It is a low-cost, low temperature, and easily implemented process that employs an aqueous solvent [43,44] in line with the development of green chemistry [45] and can be scaled up for industrial purposes. It further allows the implementation of the selective area growth using a wide variety of advanced lithography processes involving a soft mask to form ordered ZnO NW arrays with great structural uniformity [46–48]. This contrasts with other deposition techniques using a chamber under vacuum and at high temperature only favoring the growth over relatively small surface areas [34–40], and where the implementation of the selective area growth is much more complicated *via* the use of rigid mask requiring a larger number of technological processes in a cleanroom environment. As a consequence, CBD has been reported in the vast majority of investigations showing the integration of ZnO NWs in flexible piezoelectric devices [18–21]. In this CBD technique, polarity is an even more critical issue. In contrast to the vapor phase deposition techniques for which spontaneously grown ZnO NWs are until now systematically Zn-polar with the possible nucleation of inversion domain boundaries to force the Zn-polarity [49], the CBD technique offers the possibility to select the O- or Zn-polarity of ZnO NWs [50] *via* a polarity transfer from the nucleation surface [3,5]. On the one hand, this represents a great opportunity to investigate in detail the polarity effects on many processes and properties. On the other hand, the polarity transfer often occurs at the expense of the polarity uniformity in the arrays. This additional tunable parameter for growing O- and Zn-polar ZnO NWs by CBD along with the related polarity non-uniformity in the arrays should have a strong impact in the fields of piezotronic and piezoelectric devices. The present statement has however been underestimated so far to a large extent. And yet, it may partly account for the relatively limited performances of the piezoelectric devices integrating ZnO NWs as compared to their expected higher potential.

Following an introductory section on the basic principles of crystal polarity, this review discusses the most important consequences related to the polarity issue in ZnO NWs grown by CBD and the subsequent effects on piezotronic and piezoelectric devices. A special emphasis is placed on the effects of polarity on the nucleation and growth mechanisms, defect incorporation and doping, contact properties, and device performances.

2. Polarity: basic principles and measurements

2.1. Definition

Under standard temperature and pressure conditions, ZnO crystallizes into the so-called wurtzite structure belonging to the $P6_3mc$ (or C_{6v}) space and *6mm* point groups. The wurtzite structure is formed by the stack of alternate positively- and negatively-charged planes composed of respective zinc and oxygen atoms in the <0001> direction, namely along the *c*-axis. Zinc and oxygen atoms are typically distributed according to two interpenetrated hexagonal compact structures that are shifted with respect to each other by the internal cell parameter *u*. The coordination of zinc and oxygen atoms is tetrahedral. Owing to the non-centrosymmetric character of the wurtzite structure, ZnO is a piezoelectric material with large piezoelectric coefficients in the ranges of 0.89–1.19 C/m^2 for e_{33}, −0.62 to −0.51 C/m^2 for e_{31}, and −0.46 to −0.37 C/m^2 for e_{15} [51–53]. The actual internal cell parameter *u* around 0.3817 [54] significantly deviates from its theoretical value of 0.375, which mainly originates from the significant difference in the electronegativity of zinc and oxygen atoms. The ionocovalent chemical bonding has an ionicity degree of 0.616 on the Philips scale [55]. According to the classification of Tasker [56] as represented in Fig. 1, the *c*-axis is of Type III and polar, exhibiting both a nonzero charge and a nonzero dipole moment in the repeated unit cell. ZnO is thus a pyroelectric material with a spontaneous polarization field along the *c*-axis. In contrast, the $[1\bar{1}00]$ direction (*i.e.*, the *m*-axis) is of Type I and nonpolar, having a zero charge and a zero dipole moment. Consequently, ZnO NWs with a hexagonal base exhibit one polar *c*-plane top face and six nonpolar *m*-plane sidewalls, their spontaneous polarization and piezoelectric fields being oriented along the growth *c*-axis.

In the absence of any strain, the magnitude of the spontaneous polarization field has been estimated from *ab initio* calculations to be about −0.057 C/m^2 and it is dependent upon the value of *u* [51,52]. The [0001] (*i.e.* +c) and $[000\bar{1}]$ (*i.e.* −c) directions are inequivalent and should be distinguished as represented in Fig. 2. By convention, when the vector of the cation-anion bond colinear to the *c*-axis starts from a zinc atom to an oxygen atom, the [0001] direction is defined and called Zn-polar. In contrast, when the same vector starts from an oxygen atom to a zinc atom, the $[000\bar{1}]$ direction is defined and called O-polar. The polarity is a bulk property and should be distinguished from the surface termination: in principle, Zn- and O-polar surfaces can be terminated by zinc or oxygen surface atoms.

2.2. Stabilization processes of polar surfaces

Following the classification of Tasker, the nonzero dipole moment in the repeated unit cell should be responsible for an electrostatic instability and hence the polar surfaces should be unstable with a divergence in the surface energy [56]. In contrast, the formation of stable polar surfaces in ZnO has largely been reported experimentally, and a vast literature on that issue exists [58]. According to a simple electrostatic model representing the stack of *N* capacitors composed of charged planes σ separated by a distance $R_1 = 0.61$ Å, each capacitor being separated by a distance $R_2 = 1.99$ Å, the total dipole moment μ_{tot} is given by: $\mu_{tot} = N\sigma R_1$. In this configuration represented in Fig. 3a, μ_{tot} depends on the thickness and thus the electrostatic potential diverges [4]. Interestingly, μ_{tot} gets independent upon the thickness when a charge density $\Delta\sigma = \sigma R_1/(R_1 + R_2)$ is introduced on the edges of the structure [4], as presented in Fig. 3b. The stabilization condition is defined by the geometric factor $\mathscr{R} = R_1 / (R_1 + R_2) \approx 0.25$ in the case of

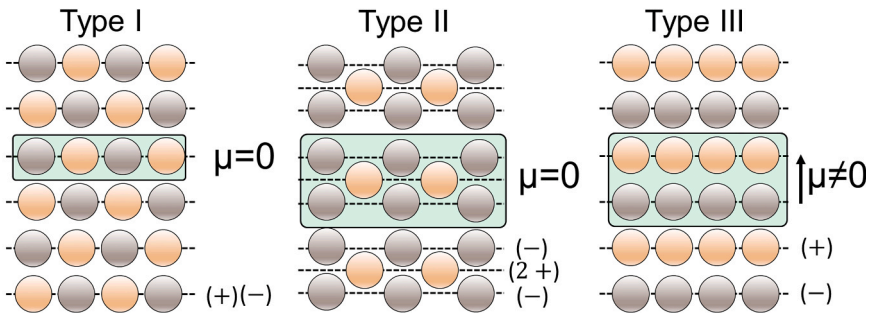

Fig. 1. Type I, II and III surfaces according to the classification of Tasker [56].

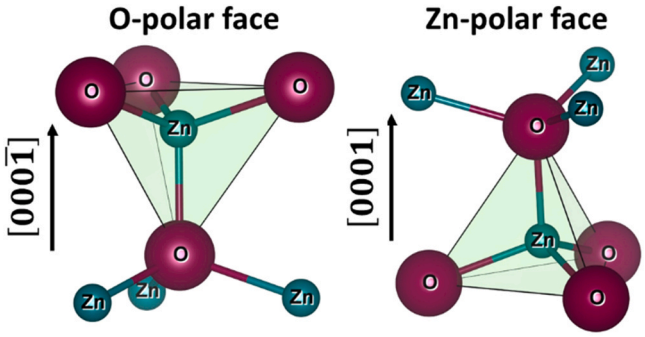

Fig. 2. Side view of the O- and Zn-polar faces with the coordination tetrahedron centered on the Zn atom. Reprinted with permission from Ref. [57]. Copyright 2017 American Chemical Society.

ZnO [1]. The introduction of compensating charges on the polar surfaces of ZnO therefore acts in principle as an efficient stabilization mechanism. It can be achieved by many different processes [59], including charge displacement [60], stoichiometry modifications [61], and chemical species adsorption [62]. All of the surface stabilization processes are dependent upon the bulk polarity and the physical/chemical environmental conditions.

The displacement of compensating charges from the O- to Zn-polar perfect surfaces has been one of the first investigated stabilization process [60,63]. Nevertheless, the resulting metallic surface states have not been revealed experimentally yet, [64,65] and the metallicity character has theoretically been questioned for clean surfaces [66]. The stoichiometry modifications involving the reduction of one quarter of oxygen atoms and of one quarter of zinc atoms on the O- and Zn-polar surfaces, respectively, has experimentally been shown through reconstruction phenomena [61]. Atomic models for the bulk terminated (0001) and (000$\bar{1}$) ZnO surfaces are presented in Fig. 4a, b. In the case of Zn-polar surfaces, triangular indentations composed of zinc atoms with one

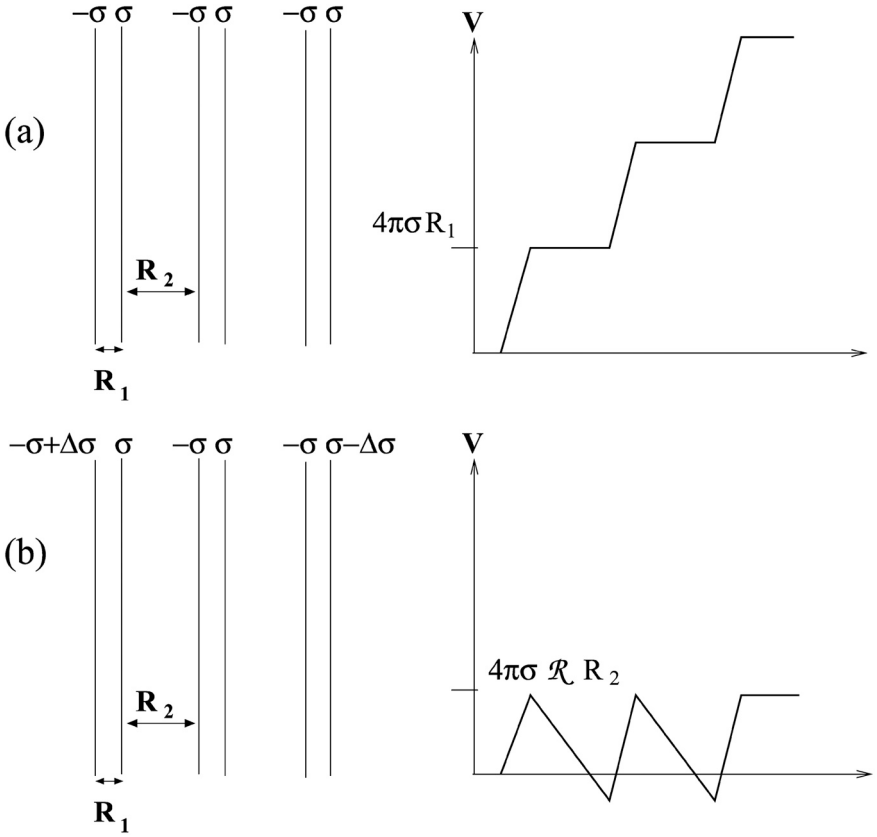

Fig. 3. Capacitor models (a) without and (b) with compensating charges on the outer layers and sketch of the electrostatic potential *V* in a slab cut along a polar direction. Reprinted with permission from Ref. [4]. Copyright 2013 American Chemical Society.

monolayer height having oxygen atoms on the edges coexist with linear reconstructions composed of zinc vacancies (V_{Zn}) [61,62,67,68]. In the case of O-polar surfaces, (5 × 5) reconstructions are composed of hexagonal pits with one monolayer height, in which eleven oxygen atoms and seven zinc atoms are taken out [61,68,69], along with the adsorption of hydrogen atoms on the oxygen atoms [70]. The different reconstructions on both polar surfaces mainly originate from the larger flexibility of zinc atoms to create bonds owing to their *d*-type orbitals [69]. Eventually, the adsorption of chemical species like hydrogen, oxygen, and hydroxyl groups from the environment to form hydroxylated polar surfaces has also appeared as an efficient stabilization process [71], as presented in the phase diagram in Fig. 4c. In the case of Zn-polar surfaces, hydroxyl groups forming one half of a monolayer are formed under hydrogen-rich conditions [59,62]. The hydroxyl groups deplete the electron excess in the conduction band to form a semiconducting surface [72]. The adsorption of one monolayer of hydrogen atoms on zinc and oxygen atoms composing the triangular reconstructions has also been reported [73]. In the case of O-polar surfaces, the formation of hydroxyl groups comes from the adsorption of hydrogen atoms over one third to one half of the oxygen atoms [74–76]. Interestingly, the presence of hydroxyl groups and $Zn(OH)_2$ phases in ZnO nanocrystals and NWs grown by wet chemistry has been shown by X-ray photoelectron spectroscopy and photoluminescence measurements through the yellow emission band and possible exciton quenching, respectively [77–80].

2.3. Free energy of polar surfaces

In the growth of ZnO NWs by CBD, their formation mechanism is governed by thermodynamic considerations minimizing the free energy of the system. As such, the surface energy represents an important quantity. The free energy of the nonpolar *m*-plane is about 1.15 J/m^2, and hence this plane has the lowest surface energy in ZnO [81,82]. In contrast, the determination of the free energy of Zn- and O-polar surfaces has been a long debate. The cleavage perpendicular to the *c*-axis gives rise to two inequivalent surfaces with opposite polarity that cannot be readily decoupled. Accordingly, the sum of both free energies has been deduced from the first theoretical calculations [60,82]. From the most recent *ab initio* calculations, a zinc-blend/wurtzite heterojunction scheme has been established to estimate the free energy of both polar surfaces to the accuracy determined by the uncertainty of the interface energy [83]. The free energy of the O-polar truncated surface of about 1.35 J/m^2 is significantly smaller than the free energy of the Zn-polar truncated surface of about 2.49 J/m^2, rendering them much more stable. Alternative approaches have indicated that the free energy of O- and Zn-polar surfaces lies in the ranges of 1.17–2.04 and 2.11–2.25 J/m^2, respectively [84,85]. Overall, the lower polarizability of the Zn-polar surface as compared to the O-polar surface accounts for its higher surface energy [68].

2.4. Behavior of polar surfaces in water

As the medium to form ZnO NWs by CBD is aqueous, the behavior of O- and Zn-polar surfaces in the presence of water molecules is of great interest [58]. Following a long debate, it has been concluded that water molecules are dissociated by the O- and Zn-polar surfaces, preferentially on surface atoms and defects [86–89]. The adsorption and dissociation of water molecules on the polar surfaces act as an efficient stabilization process over a broad range of temperature and pH. The polar surfaces of ZnO are thus hydroxylated in water, resulting in the formation of hydroxyl groups on their uppermost layer (*i.e.*, Zn – OH). In aqueous solution, the uppermost hydroxyl groups of ZnO can react with H^+ ions at low pH or HO^- ions at high pH as follows [90]:

$$Zn-OH+H^+ \leftrightarrow Zn-OH_2^+ \quad (1)$$

$$Zn-OH+OH^- \leftrightarrow Zn-O^- + H_2O \quad (2)$$

Depending on the magnitude of the pH, the uppermost hydroxyl groups are positively or negatively charged. The surface electrical charge switches from a positive to negative value at a given pH, denoted as the isoelectric point (IEP) [91,92]. The IEP represents the point for which the surface electrical charge is neutral and bares an equal number of positive and negative charges. Correlatively, the point of zero charge (PZC) represents the point for which the surface electrical charge is neutral and does not bare any individual charges. Basically, the values of PZC and IEP in ZnO strongly depend on the coordination of surface oxygen atoms and of their polarization by the zinc atoms, which are related to the nature of crystallographic planes and of polarity. For the O-polar (resp. Zn-polar) surfaces, the surface oxygen atoms are linked to three (resp. one) zinc atoms of the downer layer. As a result, the surface protonation is described as follows for each of the polarity:

$$Zn_3-O^{-\frac{1}{2}}+H^+ \leftrightarrow Zn_3-OH^{+\frac{1}{2}} \quad (3)$$

$$Zn_1-O^{-\frac{3}{2}}+2H^+ \leftrightarrow Zn_1-OH_2^{+\frac{1}{2}} \quad (4)$$

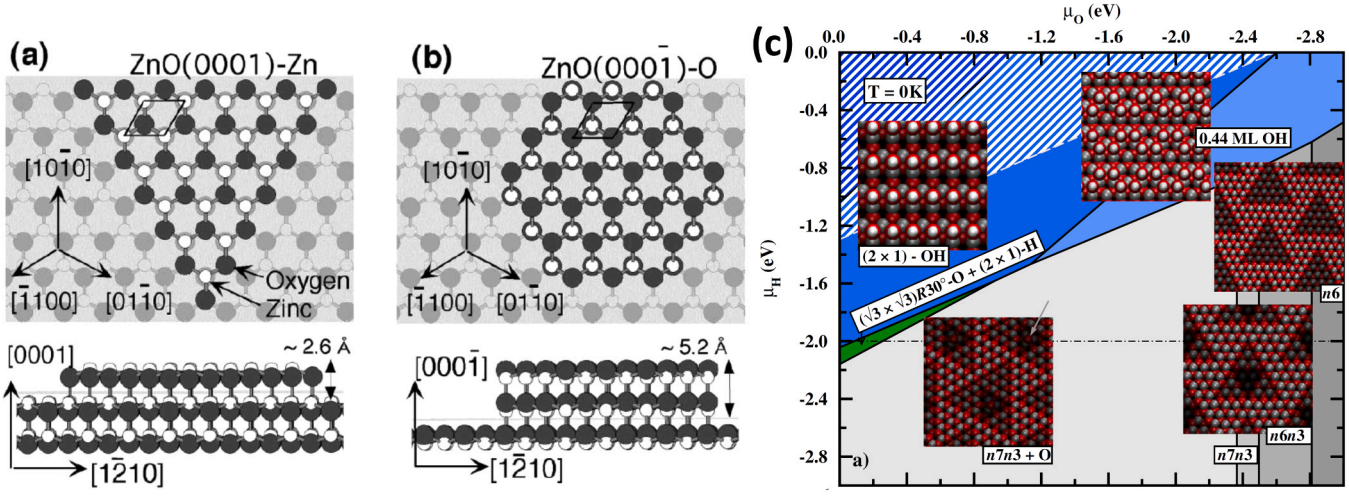

Fig. 4. Top- and side-views of atomic models for the bulk terminated (a) (0001) and (b) (000$\bar{1}$) ZnO surfaces. Adapted from Ref. [61]. Copyright 2002 Elsevier. (c) Phase diagram for the Zn-terminated (0001) ZnO surface in equilibrium with a humid oxygen atmosphere at 0 K. Equilibrium conditions under which water would condensate on the surface are indicated by the hashed area (upper left corner). The geometries of the stable surface structures are shown as insets. The hydrogen chemical potential is marked by a dot-dashed black line. Adapted from Ref. [71]. Copyright 2009 American Physical Society.

Since the concentration of H^+ ions needed for compensating the surface electrical charge is larger for the Zn-polar surface than for the O-polar surface, the values of PZC and IEP are expected to be higher for the O-polar surface than for the Zn-polar surface. Overall, the IEP values in ZnO lie in the range of 8.7–10.3 and no distinction has been made regarding the crystallographic plane involved [91,92]. More interestingly, the PZC of the Zn-polar surface was reported to 8.7 ± 0.2 [93] while the PZC of the *m*-plane is of 10.2 ± 0.2 [94]. It is thus significantly lower for the *c*-plane top face of ZnO NWs than for their *m*-plane sidewalls. In aqueous solution, the surface electrical charge further results in the formation of a double electrical layer composed of an adsorbed counter-ion layer (*i.e.* Stern layer) and of a diffusive layer where ions are distributed according to the balance between electrostatic and thermal forces [95]. The zeta potential defined as the electrical potential located at the limit of the double electrical layer corresponding to the slipping plane of the solvent should also depend on the surface polarity.

2.5. Contact properties on polar surfaces

The chemistry of free polar surfaces has been studied in various environmental conditions to provide a deeper understanding of the surface chemical and electronic properties. Typically, using techniques such as X-ray photoelectron spectroscopy (XPS), the polar real surfaces of ZnO single crystals invariably exhibit downward surface band bending after exposure to atmosphere as a result of donor hydroxyls creating a surface electron accumulation layer (SEAL) [96,97]. Electrically, this presents itself as a metallic surface layer with greater conductivity than the bulk [97–99]. The extent of downward band bending relative to the Fermi level is often greater on the Zn-polar surfaces with typical values > 0.5 eV measured on hydrothermally grown single crystals while a lesser effect is found on O-polar surfaces [100]. Heinhold et al. showed with *in situ* heating, H_2O dosing and atmospheric exposure in a synchrotron XPS that the flat band condition could be achieved on O-polar surfaces when the surface H coverage was approximately 0.9 monolayers [96]. However, the Zn-polar surface hydroxyl layer was much more resilient to heating and vacuum with an OH surface coverage of 0.8 monolayers ML persisting at 750 °C and always remaining in the downward band bending state. This difference is a consequence of the polar terminations with hydroxide forming on the O-polar surface when H bonds to lattice oxygen while on the Zn-polar surface the reactions involve OH groups. The extensive hydroxyl coverage and associated accumulation layer on both polar surfaces after exposure to atmosphere has important implications for the fabrication of high quality Schottky contacts.

In addition to the SEAL, there is a high concentration of sub-surface point defects in ZnO single crystals that results in Ohmic electrical contacts on untreated surfaces, particularly with noble metals [102,103]. The hydroxide layer and defective atomic lattice near the surface are shown in Fig. 5a along with the resultant effect on the electronic nature of the surface depicted by a band diagram [101]. Point defects such as vacancies at the ZnO surface introduce energy levels into the band gap that can influence surface band bending and the Schottky barrier height (SBH) after metal deposition. Surface and sub-surface vacancies are also created by chemical reactions that take place on the surface and at an interface when in contact with a metal. A high concentration of surface/interfacial states can lead to Fermi-level pinning near to the energy level of the dominant defect state [104–107]. Schottky barrier inhomogeneity which may stem from variations in interface structure, defects, or the contact material, creates neighboring regions of differing SBH [108]. Sub-surface defects affect the local carrier concentration and the contact depletion region introducing energy levels into the band gap that can assist defect related transport mechanisms such as hopping/tunneling [109]. Segregation of defects towards the ZnO surface can differ according to polarity with higher vacancy

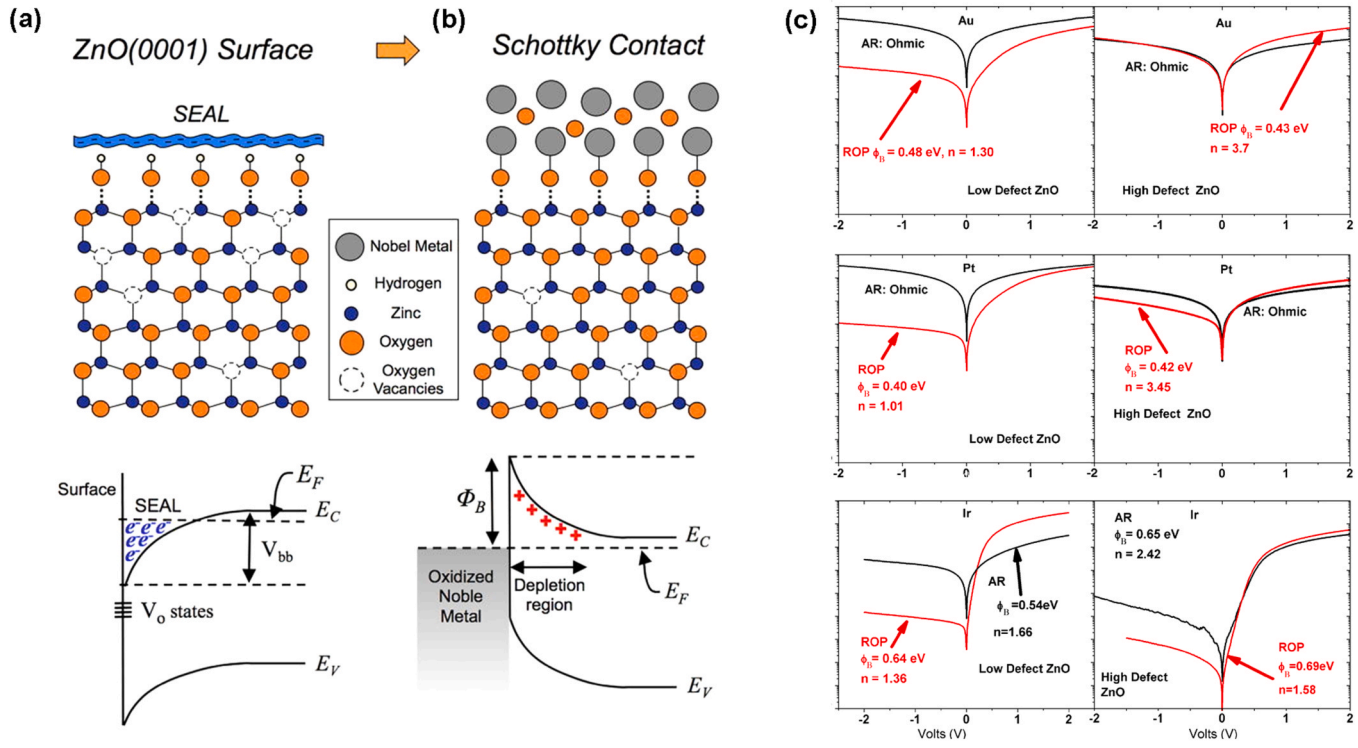

Fig. 5. (a) A lattice model of a free ZnO surface when exposed to atmosphere creating a SEAL with vacancy defects and the resultant band diagram. (b) After an oxidizing metal deposition process, the lattice model shows the SEAL is removed and vacancies are filled resulting in the Schottky barrier shown in the band diagram. Adapted from Ref. [101]. Copyright 2008 American Institute of Physics. (c) Current-voltage measurements of various metals deposited on $(000\bar{1})$ single crystal ZnO, before (black) and after (red) oxygen plasma treatments on crystals with low (low defect) and high (high defect) luminescent defect band emissions. Adapted from Ref. [102]. Copyright 2007 American Institute of Physics.

densities recorded in the surface and sub-surface regions of the O-polar face [109]. All of these effects can cause a large deviation of the measured SBH from that predicted by the Schottky–Mott theory.

The application of oxygen plasma treatments at elevated temperatures to Zn- and O-polar surfaces was shown by Coppa et al. to reduce the hydroxide coverage to 0.4 monolayers ML on both polar surfaces while subsequent cooling in oxygen atmosphere resulted in an oxygen terminated surface and upward band bending [110]. This sequence of treatments dramatically improved the Au Schottky contacts such that barrier heights of 0.71 eV and 0.6 eV were formed on the Zn- and O-polar surfaces, respectively. The oxygen treatments had several effects of inducing a surface depletion layer, improving the stoichiometry and surface structure, and eliminating hydrocarbon contamination. Furthermore, several works have shown that simple oxidizing plasma treatments before metal deposition significantly reduce the luminescent defect band emissions associated with oxygen vacancy (V_O) and V_{Zn} defects that switches the contact properties from Ohmic to rectifying, as illustrated in Fig. 5c [102,111]. This was further developed by Allen and Durbin who showed using various metals that the SBH has a relationship with the free energy of formation of the metal's oxide suggesting chemical reactions at the interface create V_O which have a decisive influence on the contact properties [112]. We can expect that the lower the energy required for metal oxide formation on contact deposition, the greater the likelihood there is of high densities of vacancy defects being present near the interface. They argued that a high concentration of V_O at the metal interface, both intrinsic and as a result of chemical reactions with the metal, pins the ZnO Fermi level near to the V_O energy level ~ 0.7 eV below the conduction band minimum (CBM), restricting the SBH. Although the exact energy level of V_O is still debated, this helps to explain why many metals on ZnO have previously displayed SBH values

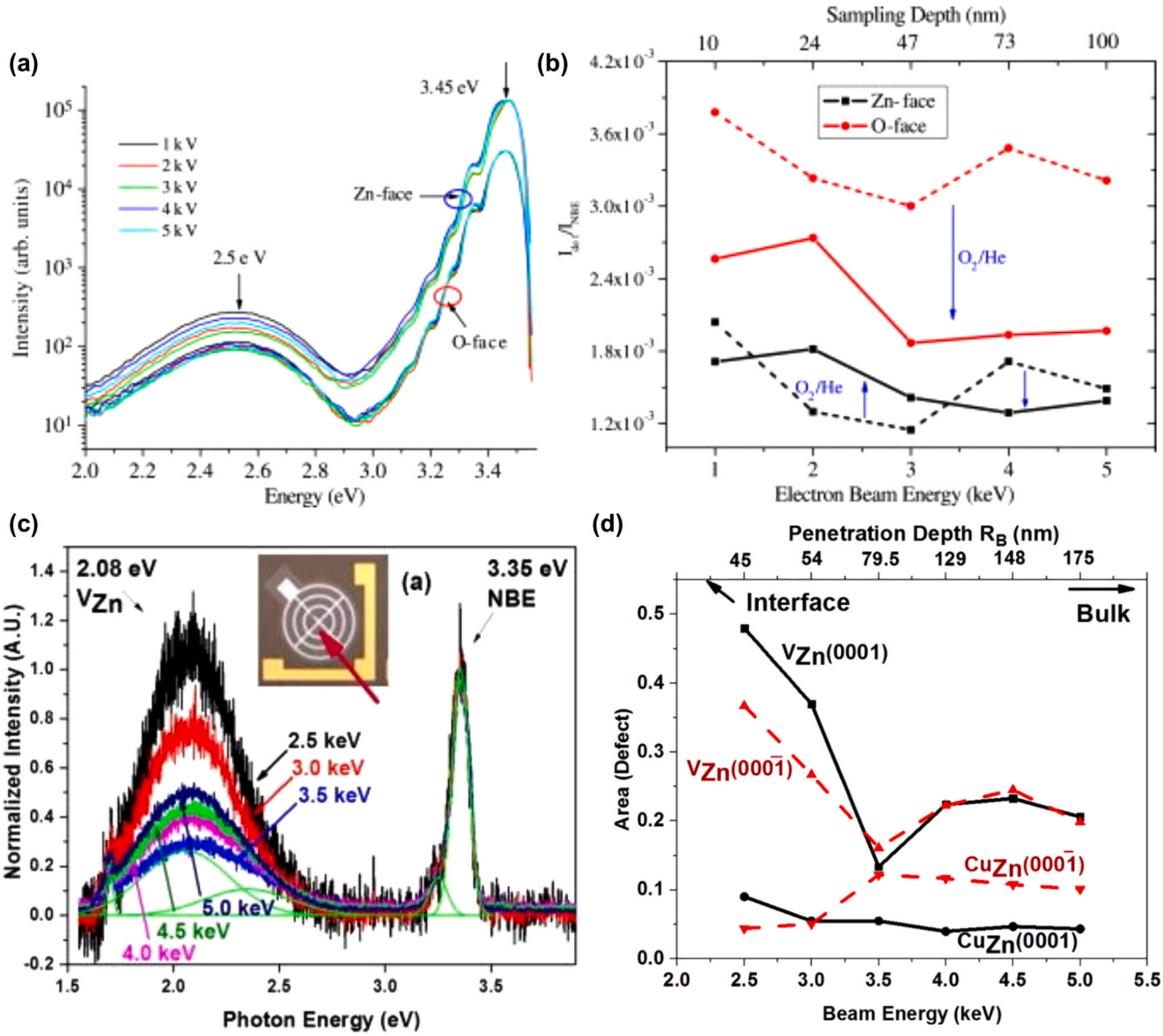

Fig. 6. Depth-resolved cathodoluminescence spectroscopy comparing oxygen plasma treated surfaces and oxidized noble metal Schottky contacts. (a) Depth-resolved cathodoluminescence spectra over a range of beam energies of solvent cleaned O- and Zn-faces of the same crystal and the dominant defect emission at 2.5 eV associated with V_O. (b) The variation of I(2.45 eV)/I(*NBE*) for the same surfaces before and after oxygen plasma treatment showing a large reduction in defects on the O-face. NBE stands for near band edge. Adapted from Ref. [103]. Copyright 2009 Elsevier. (c) Depth-resolved cathodoluminescence spectra through an oxidized Ir Schottky contact on the Zn-face showing a large increase in the defect emission associated with V_{Zn}. (d) Depth variation below the same Schottky interface of V_{Zn} and another acceptor defect Cu_{Zn} on the Zn- and O-faces revealing a much higher density of V_{Zn} on the Zn-face for these contacts. Adapted from Ref. [115]. Copyright 2017 American Institute of Physics.

in the region of 0.6–0.8 eV [113].

The strong influence of V_O on contacts to both polar surfaces has led to the application of oxidized metal contacts that can significantly breach the constraints of the earlier pinned Schottky contacts [101,104,114]. In these examples, noble metals were oxidized during the deposition process that vastly improved the Schottky contacts when compared to non-oxidized contacts such as PtO_x providing a barrier height of up to 1.3 eV [101]. The vast improvement comes from a combination of the removal of the surface hydroxide accumulation layer, the excess oxygen present during metal deposition passivating interfacial V_O removing any pinning effect, and an increase in the work function and electronegativity of the Schottky contacts, as depicted in Fig. 5b [101,104].

The surface modification and contact fabrication methods required for high quality contacts to the polar surfaces are not insignificant, which can make it difficult to determine whether the polarity has an influence on the contact properties. This is displayed by works that report little difference between non-oxidized metal Schottky contacts on the O- and Zn-polar surfaces most likely due to V_O related Fermi-level pinning [116]. However, with more elaborate contact fabrication methods and directly comparing oxidized Schottky contacts on the two polar surfaces of the same crystal, in order to minimize any difference in bulk properties, the Zn-polar surface consistently has larger SBHs and lower ideality factors [101,115]. On low-doped samples with oxidized silver contacts, a significant difference was found between the Zn- and O-polar crystals (Zn-polar barrier height as large as 1.2 eV), but this difference diminishes for crystals with a carrier concentration in excess of 10^{17} cm^{-3}, approaching the level in CBD-grown NWs [114]. Significantly higher defect band emissions associated with V_O are often measured on the O-polar surfaces (Fig. 6a, b) and this helps to explain the difference in Schottky barriers [103,104,109,117,118]. However, the electrical contact interface and associated potential energy field are highly dependent upon the surface and subsurface defect chemistry, which can vary greatly with ZnO growth method, sample preparation, and surface polarity, as seen in Fig. 6b [109,115]. This was revealed more recently on IrO_x contacts to hydrothermally grown ZnO single crystals with a very low defect density that predominantly displayed V_{Zn} near the polar contact surfaces, as shown in Fig. 6c [115]. A significantly higher concentration of V_{Zn} near the Zn-polar interface led the authors to develop a defect-segregation model based on observations with depth-resolved cathodoluminescence spectroscopy of the contacts on both polar surfaces, as revealed in Fig. 6c, d. This could account for the greater 0.89 eV barrier height compared to 0.67 eV of the IrO_x contacts on the Zn- and O-polar surfaces, respectively, since V_{Zn} acts as an acceptor increasing the depletion region width and measured SBH. The preferential segregation of V_{Zn} towards the Zn-polar surface is due to the spontaneously polarized electric field in ZnO and associated band bending. In all of these works, the near-surface defects that govern the properties of high quality Schottky contacts are dependent upon the polarity of the surface and related to the free carrier concentration in this region. Generally, on ZnO single crystals, the O-polar surface region has a higher defect density than the Zn-polar surface region that can lead to lower SBHs and higher ideality factors. As with most aspects of ZnO, definitively detecting and identifying point defects is troublesome as they are very sensitive to the growth method and provide the great variety of bulk and interfacial properties; however, in this way, crystal polarity can influence the electrical contacts [117].

2.6. Polarity measurements

The polarity of ZnO can be measured by a large number of characterization techniques using selective chemical etching [119], transmission electron microscopy (TEM) [120–123], X-ray and electron diffraction [124–126], and atomic force microscopy (AFM) [127,128]. The TEM-based experiments include high angle annular dark field and annular bright field (ABF) imaging [122] (Fig. 7a), convergent beam electron diffraction [50,120] (Fig. 7b), electron energy loss spectroscopy [121] (Fig. 7c), and electron holography [123]. The X-ray and electron diffraction-based experiments involve low-energy electron diffraction [124], resonant X-ray diffraction in synchrotron [125,129] (Fig. 7d), and angle-resolved X-ray photoelectron diffraction [126]. The AFM-based experiments are based on piezoelectric response force microscopy [127] and Kelvin probe microscopy [128]. More exotic techniques include coaxial impact collision ion scattering spectroscopy [130], scanning nonlinear dielectric microscopy [131]. The comprehensive review of Zuniga-Perez et al. provides more details regarding the basic principles of each polarity characterization technique [3].

3. Nucleation and growth: its polarity dependence

3.1. Generalities about chemical bath deposition

The CBD is based on the homogeneous [132] and heterogeneous [41] growths of ZnO NWs. For piezotronic and piezoelectric devices, the heterogeneous formation of ZnO NWs on an appropriate nucleation surface is preferred. The chemical bath typically contains a zinc salt (*e.g.* zinc nitrate, zinc acetate, or zinc sulfate) and a source of HO^- ions (*e.g.* caustic soda, ethanolamine, or hexamethylenetetramine (HMTA)) mixed in an equimolar/non-equimolar ratio in aqueous solution [44]. Ammonia is often added to reduce the homogeneous growth of ZnO microstructures in the bath and to monitor the pH value. The reactor containing the bath is either open [133] or sealed [41] and hence the depletion of chemical reactants occurs to establish dynamic conditions. Alternative reactors working under a continuous flow of chemical reactants are developed as well to establish homeostatic conditions [134,135]. The reactor is typically placed in an oven heated up to a growth temperature ranging from 70 °C to 90 °C. Microwave heating is useful as well to reduce the actual growth temperature and drastically boost the growth rate of ZnO NWs that typically lies around 1 Å/s using thermal heating to 16 Å/s [134]. In contrast to many alternative deposition techniques used to form ZnO NWs, CBD operates under thermodynamic near-equilibrium conditions with a relatively small supersaturation ratio. In the most widely reported conditions using zinc nitrate and HMTA as the two chemical precursors, the CBD of ZnO NWs is driven by the set of the following chemical reactions [43]:

$$(CH_2)_6N_4 + 6H_2O \rightarrow 6HCHO + 4NH_3 \quad (5)$$

$$NH_3 + H_2O \leftrightarrow NH_4^+ + HO^- \quad (6)$$

$$Zn(NO_3)_2 \rightarrow Zn^{2+} + 2NO_3^- \quad (7)$$

$$Zn^{2+} + 4NH_3 \leftrightarrow Zn(NH_3)_4^{2+} \quad (8)$$

$$Zn^{2+} + 2HO^- \leftrightarrow ZnO_{(s)} + H_2O \quad (9)$$

$$Zn^{2+} + 2HO^- \leftrightarrow Zn(OH)_2 \quad (10)$$

$$Zn(OH)_2 \leftrightarrow ZnO_{(s)} + H_2O \quad (11)$$

Basically, HMTA is progressively hydrolyzed with heat, forming formaldehyde and ammonia (Eq. (5)). Then, ammonia reacts with water, producing HO^- ions (Eq. (6)). In addition to be a source of HO^- ions, HMTA acts as a pH buffer limiting the supersaturation ratio in the bath to kinetically control the growth of ZnO NWs [136] and inhibits the development of the nonpolar *m*-plane sidewalls to increase their aspect ratio [137–139]. Zn^{2+} ions are produced through the solubilization of zinc nitrate (Eq. (7)). Zn^{2+} and $Zn(NH_3)_4^{2+}$ ions are predominant Zn(II) species in the low and high pH ranges, respectively, with a transition around 7 depending on the bath temperature [136,140,141]. The crystallization of ZnO NWs follows a direct (Eq. (9)) or indirect process (Eqs. (10) and (11)), depending on the conditions used [136,142]. Under conventional temperature conditions, the crystallization process of ZnO NWs is direct through the dehydration process of $[Zn(H_2O)_6]^{2+}$ ions involving no formation of long-lived intermediates [143]. The shape of

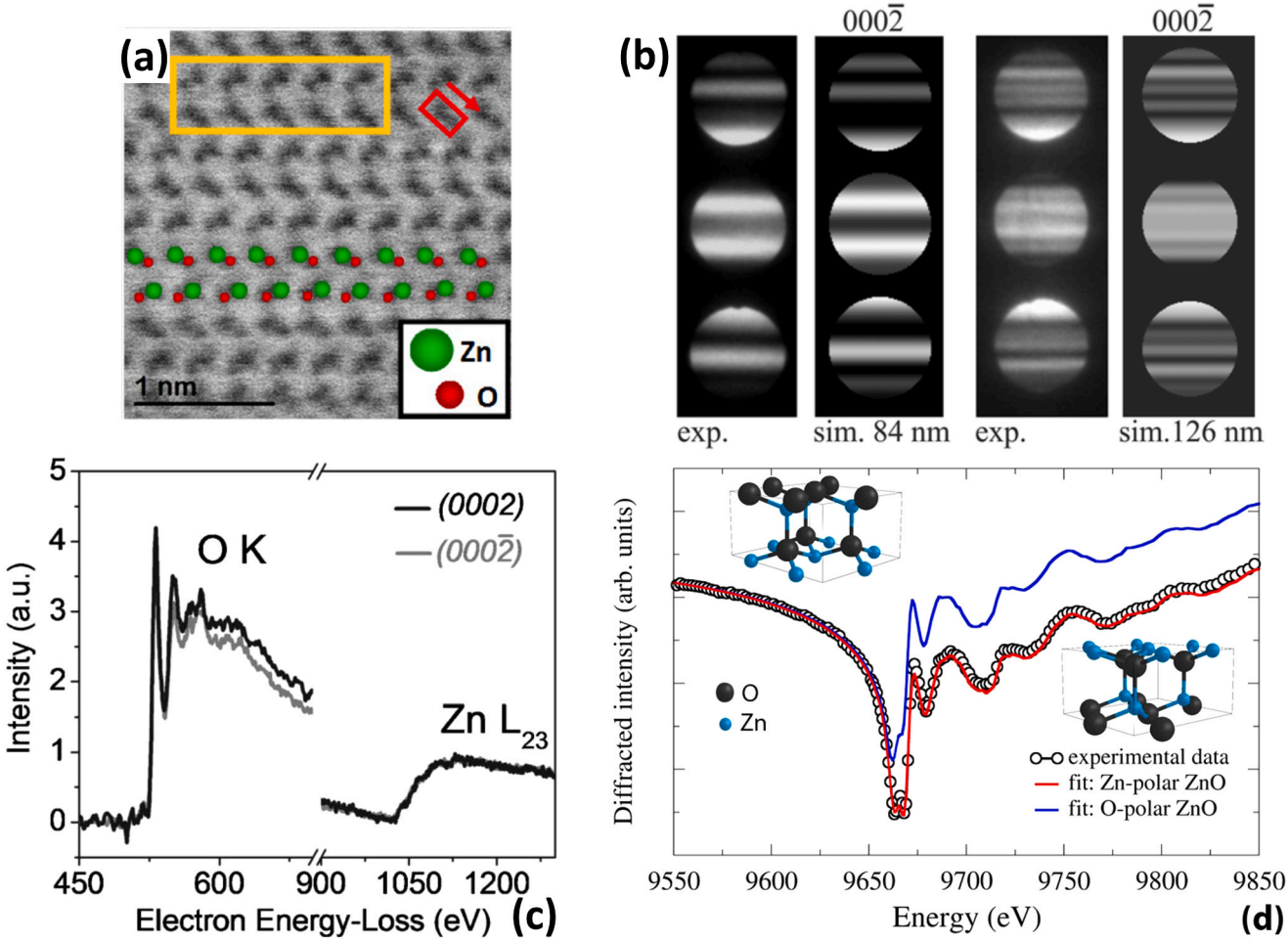

Fig. 7. (a) Atomic resolution aberration corrected ABF-STEM detail obtained on a single Zn-polar ZnO NW. Adapted from Ref. [122]. Copyright 2012 American Chemical Society. (b) Experimental and simulated CBED patterns taken along the <10$\bar{1}$0> zone axis for both thickness of 84 and 126 nm on a single O-polar ZnO NW. The central disc is the transmitted electron beam. Adapted from Ref. [50]. Copyright 2014 American Chemical Society. (c) EELS spectra measured under two-beam Bragg conditions for the (0002) and (000$\bar{2}$) diffracted beams, respectively, on a single Zn-polar ZnO NW. Adapted from Ref. [121]. Copyright 2008 American Institute of Physics Publishing. (d) Evolution of the background-subtracted diffracted intensity *I*(*00l*, *E*) as a function of the energy around the Zn K-edge on ZnO NW arrays. Adapted from Ref. [129]. Copyright 2017 Institute of Physics Publishing.

ZnO NWs as high aspect ratio nanostructures is governed by thermodynamic considerations involving the minimization of the free energy of the system: the development of their nonpolar *m*-plane sidewalls with the lowest surface energy is achieved at the expense of the development of the polar *c*-plane top face with a larger surface energy. In this context, the CBD proceeds through a nucleation phase to form NW nuclei followed by a growth phase to elongate the NW nuclei. The polarity issue plays a significant role on both nucleation and growth phases as discussed in the two following subsections.

3.2. Nucleation mechanisms

The nucleation phase of ZnO NWs operates on an appropriate surface that is typically a polycrystalline ZnO seed layer grown by physical and chemical deposition techniques [133,135,136,140]. Alternative nucleation surfaces include ZnO single crystals [144], GaN thin films and single crystals [145], as well as metallic seed layers using gold [146] to create a Schottky-like contact in the backside electrode for piezoelectric devices. These nucleation surfaces can be integrated onto rigid or flexible substrates. The most widely-used polycrystalline ZnO seed layer is basically composed of grains with a broad range of nonpolar, semipolar, and polar orientations. The identification of the nucleation sites has been a long debate over the last decade. A consensus has emerged on the fact that the nucleation sites are located on the free surfaces of grains when their size are larger than about 10 nm and possibly at grain boundaries when their size is smaller [147]. The nucleation sites can also be amended by adjusting the CBD conditions [148]. When the nucleation occurs on the free surface of grains, polarity has several important effects on the nucleation phase. A first report by Greene et al. showed that the vertical alignment of ZnO NWs is strongly enhanced when the nucleation phase operates on a polycrystalline ZnO seed layer that is highly textured along the polar *c*-axis [149]. Later on, ZnO NWs were found to homoepitaxially nucleate on the *c*-axis oriented grains composing the polycrystalline ZnO seed layer [150]. To circumvent the difficulty of investigating the nucleation mechanisms on an ensemble of grains with different properties, the nucleation phase and its polarity dependence has been investigated on ZnO single crystals with different nonpolar [151], semipolar [152], and polar orientations [50,57,151], as shown in Fig. 8.

The present findings have shown that the grains with nonpolar orientations are chemically active, but form a two-dimensional layer that is much more slowly developed, as presented in Fig. 8a and b by scanning electron microscopy (SEM) images [151]. The growth on these grains is expected not to form when the nucleation phase operates on a ZnO polycrystalline seed layer owing to detrimental competitive effects. Only the grains with polar and semipolar orientations as presented in Fig. 8c

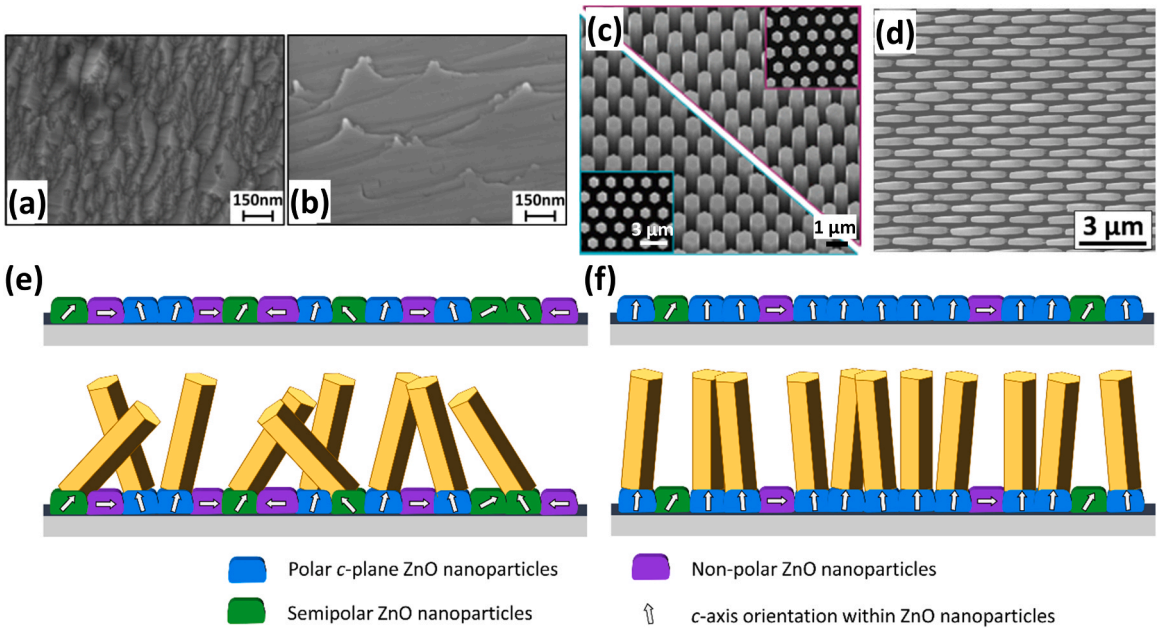

Fig. 8. SEM images of CBD grown ZnO using standard conditions over un-patterned, (a) nonpolar *a*- and (b) *m*-plane oriented ZnO single crystals. Adapted with permission from Ref. [151]. Copyright 2013 American Chemical Society. (c) SEM image of CBD grown ZnO using standard conditions over patterned, Zn- (bottom) and O- (top) polar *c*-plane oriented ZnO single crystals. Adapted with permission from Ref. [57]. Copyright 2017 American Chemical Society. (d) SEM image of CBD grown ZnO using standard conditions over patterned, semipolar ($\bar{2}0-\bar{2}1$) plane oriented ZnO single crystals. Adapted with permission from Ref. [152]. Copyright 2018 Institute of Physics Publishing. Schematic of the ZnO NW growth by CBD on a (e) poorly and (f) highly textured polycrystalline ZnO seed layer composed of grains with nonpolar, semipolar, and polar orientations. Reprinted with permission from Ref. [152]. Copyright 2018 Institute of Physics Publishing.

and d, respectively, result in the nucleation of ZnO NWs [50,57,151, 152]. A complete diagram recapitulating the nucleation phase on a poorly and highly textured ZnO polycrystalline seed layer is shown in Fig. 8e, f [152]. From this diagram, the presence of inclined ZnO NWs in an array is due to both the nucleation on the grains with semipolar orientations and to the nucleation on the grains with polar orientations when the mosaicity defining the angle of the surface *c*-plane with the plane parallel to the surface is large.

Also, chemical additives like polyethyleneimine [153] or even HMTA [139] are supposed to block out the nucleation on these grains with nonpolar orientations. On all the nucleation surfaces, the formation of ZnO NWs follows a homo-epitaxial process [150–152]. Under standard conditions, the nucleation of O- and Zn-polar ZnO NWs is homo-epitaxially achieved on O- and Zn-polar ZnO grains in the polycrystalline seed layer through a polarity transfer process [151]. For instance, Zn-polar ZnO NWs were formed on top of ZnO seed layers grown by pulsed-laser deposition with the Zn-polarity [154] and with an unknown polarity [120], as well as on top of silver seed layers [127]. Cherns et al. further reported the nucleation of Zn-polar ZnO NWs on top of Zn-polar ZnO NWs grown by pulsed-laser deposition [155,156]. This process also operates on ZnO single crystals to get polarity-controlled vertical ZnO NWs with great structural uniformity [50]. Similarly, inclined *c*-axis oriented ZnO NWs are homo-epitaxially nucleated on semipolar ZnO grains, where the inclination angle corresponds to the angle between the semipolar and *c*-planes [152]. This polarity transfer process was further revealed on N- and Ga-polar GaN substrates with the formation of O- and Zn-polar ZnO NWs, respectively [145]. The Zn-polar *c*-plane top face was found to be more reactive than the O-polar *c*-plane top face, leading to the formation ZnO nanotubes by dissolution in water. Both O- and Zn-polar surfaces on the top face of ZnO NWs were found by X-ray absorption fine structure at the oxygen K edge to be hydroxylated through the saturation with OH groups. Overall, the polarity transfer process by homo/heteroepitaxy using CBD is remarkable. It should however be distinguished from the processes at work in the vapor phase deposition techniques including thermal evaporation/physical vapor transport [122,157], pulsed-laser deposition [158], molecular beam epitaxy [159], and MOCVD [49,160] for instance. In these techniques, the nucleation of Zn-polar ZnO NWs has systematically been reported regardless of the nature of the nucleation surface and of its polarity. It is believed that surfactant effects originating from the contamination of the nucleation surfaces with aluminum or other chemical elements force the Zn-polarity through the nucleation of inversion domain boundaries [49]. In most of the reports using the CBD of ZnO NWs, the formation of ZnO NW arrays with a mixed polarity is thus largely expected since the polycrystalline ZnO seed layers do not exhibit a uniform polarity. The use of post-deposition thermal treatments was shown to favor the nucleation of Zn-polar grains and NWs with a high uniformity (*i.e.* more than 92%), but the present process is not compatible with the flexible substrates required to fabricate flexible devices [129]. In addition to the polarity transfer process, the nature of chemical precursors may also contribute to the selection of the polarity of ZnO NWs. It was suggested by Rathore et al. that the use of zinc nitrate and zinc sulfate leads to the formation of O- and Zn-polar NWs, respectively [161]. However, this kind of approach would deserve a more careful analysis for distinguishing the effects of the polarity transfer process from the effects of the chemical precursors.

3.3. Growth mechanisms

3.3.1. Nanowires

The growth phase of ZnO NWs by CBD basically involves an elongation process during which their aspect ratio is tunable by further using chemical additives. In the CBD process using standard conditions, Zn(II) species are the limiting reactant because the oxygen species are provided by i) highly mobile HO^- ions produced by the decomposition of HMTA in aqueous solution and likely by ii) dissociative water molecules from the solvent on the growth front located on the *c*-plane top face of ZnO NWs. In the bath, the growth regime is basically driven by i) the surface reaction rate on the polar *c*-plane top faces of ZnO NWs and ii) the diffusive transport of the chemical reactants [162], both of them

depending strongly on their density and diameter through the so-called *c*-plane surface ratio *S* [163]. By considering the serial processes of the consumption of the limiting Zn^{2+} ions at the crystal growth front and of their diffusive transport from the bulk solution as represented in Fig. 9a, the *c*-plane growth rate $R_{c\text{-}plane}$ in homeostatic conditions is given by the following relation [163]:

$$\frac{1}{R_{c-plane}} = \frac{\rho}{C_\infty k_1} + \frac{\rho\delta}{C_\infty D} S \tag{12}$$

where ρ is the ZnO molar density, C_∞ is the bulk solution concentration of Zn^{2+} ions, k_1 is the surface reaction rate constant for crystallizing ZnO, δ is the stagnant layer thickness (*i.e.* the thickness of fluid adjacent to the substrate surface with only diffusive transport), D is the diffusion coefficient of Zn^{2+} ions in aqueous solution. For small or large S values, the growth regime is limited by the surface reaction or diffusion processes, respectively [164], as illustrated in Fig. 9b. More complex relations have been reported in dynamic conditions where the depletion of the chemical reactants occurs [165]. Interestingly, the elongation process of O- and Zn-polar ZnO NWs do not exhibit the same rate. By using pre-patterned ZnO single crystals with the same domains to leave polarity as the only varying parameter, Cossuet et al. revealed that Zn-polar ZnO NWs have a much larger axial growth rate than O-polar ZnO NWs [57], as shown in Fig. 9c. In the framework of a surface reaction/diffusive transport limited growth regime analysis, this was related to the difference in the surface reaction rate constant that was significantly larger in the case of Zn-polar ZnO NWs. This higher reactivity was attributed to a larger number of surface dangling bonds facilitating the incorporation of the limiting Zn(II) species on the Zn-polar *c*-plane top face: the incoming Zn^{2+} ions interact with the three (*resp.* one) dangling bonds of each OH group on the Zn- (*resp.* O-) polar surface, increasing (*resp.* decreasing) in turn their incorporation rate, as represented in Fig. 9d. The present argument has been invoked in the

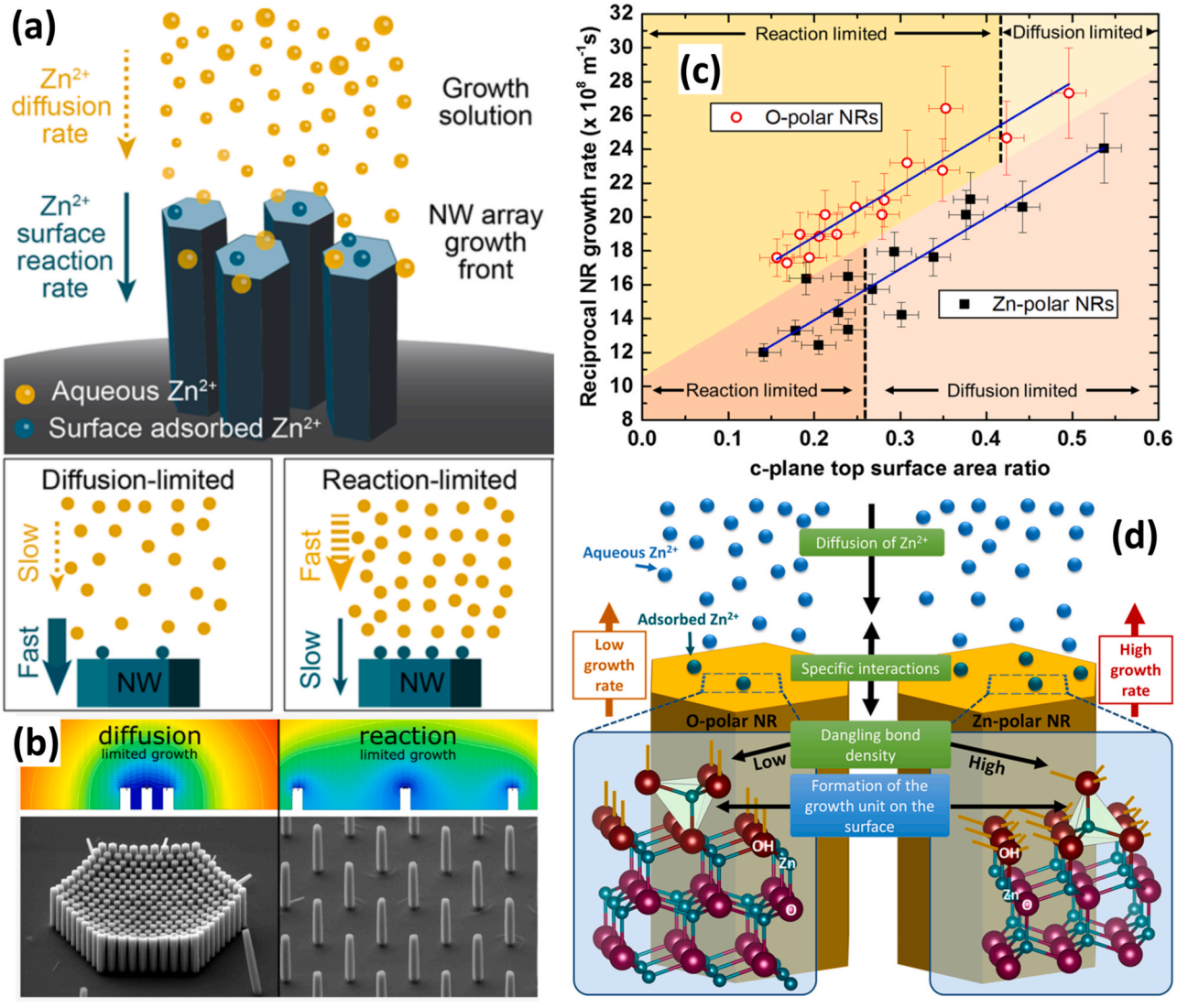

Fig. 9. (a) Schematic representing serial processes of diffusion and reaction in the vicinity of the NW array growth front. Zn^{2+} ion diffusion (dotted arrow), adsorption, and subsequent incorporation (solid arrow) into NW *c*-plane top faces. The local variation in Zn^{2+} ion concentration in the vicinity of the *c*-plane top faces is shown for diffusion- and reaction-limited growth scenarios (left and right inset, respectively). Arrow thickness represents process rate; thinner arrow refers to a slow process. Reprinted with permission from Ref. [163]. Copyright 2016 American Chemical Society. (b) Illustration of the diffusion- and reaction-limited growth regimes in strongly dense (left) and weakly dense (right) NW arrays by CBD using the selective area growth approach. Reprinted with permission from Ref. [164]. Copyright 2020 American Chemical Society. (c) Reciprocal *c*-plane growth rates of O- and Zn-polar ZnO NRs *vs* their *c*-plane top surface area ratio. The blue solid lines correspond to the linear fit to Eq. (10) with $C_\infty = 30$ mM, $\rho = 4.20 \times 10^{28}$ m^{-3}, and $D = 2.91 \times 10^{-9}$ m^2/s. The vertical dark dashed lines delimit the transition between the surface reaction- and diffusive transport-limited elongation regimes for both polarities. (d) Schematic representation of the possible mechanisms accounting for the polarity dependent growth of ZnO NRs. Reprinted with permission from Ref. [57]. Copyright 2017 American Chemical Society.

hydrothermal growth of ZnO crystals at high temperature through the incorporation of $Zn(OH)_4^{2-}$ growth units tailored by the orientation of Zn-O_4^{6-} tetrahedron at the interface [166]. Additional polarity-dependent interactions with the ionic species in solution were suggested as well, specifically a significant difference of the zeta potential for a given pH between the O- and Zn-polar ZnO NWs. Eventually, when the formation of O- and Zn-polar ZnO NWs is mixed in the same array by using a polycrystalline ZnO seed layer with a mixed polarity, both NWs should present a differential length. This should result in a couple of particularities regarding their integration into piezoelectric devices, notably in the Schottky configuration where each NW top is connected with a metallic contact like Au, for which the connection to O-polar ZnO NWs may be lost.

In addition to the different chemical reactivity on the O- and Zn-polar surfaces, polarity affects the physicochemical processes at work in the bath when chemical additives are used to monitor the aspect ratio of ZnO NWs. Chemical additives acting as capping agents are mostly employed to monitor the aspect ratio of ZnO NWs: i) polyethyleneimine [167] and ethylenediamine [168] can adsorb on the nonpolar *m*-plane sidewalls, limiting the radial growth at the benefit of the axial growth, while ii) chlorine [169] and citrate [170] ions, maleic acid and phenolphthalein [171] can adsorb on the polar *c*-plane top faces, limiting the axial growth at the benefit of the radial growth. The mechanisms involved in the adsorption of these chemical additives are not completely understood along with the effects of the polarity on the *c*-plane top face.

3.3.2. *Alternative nanostructures*

Besides ZnO NWs, a wide variety of nanostructures with different shapes can be formed by CBD using two main approaches that involve

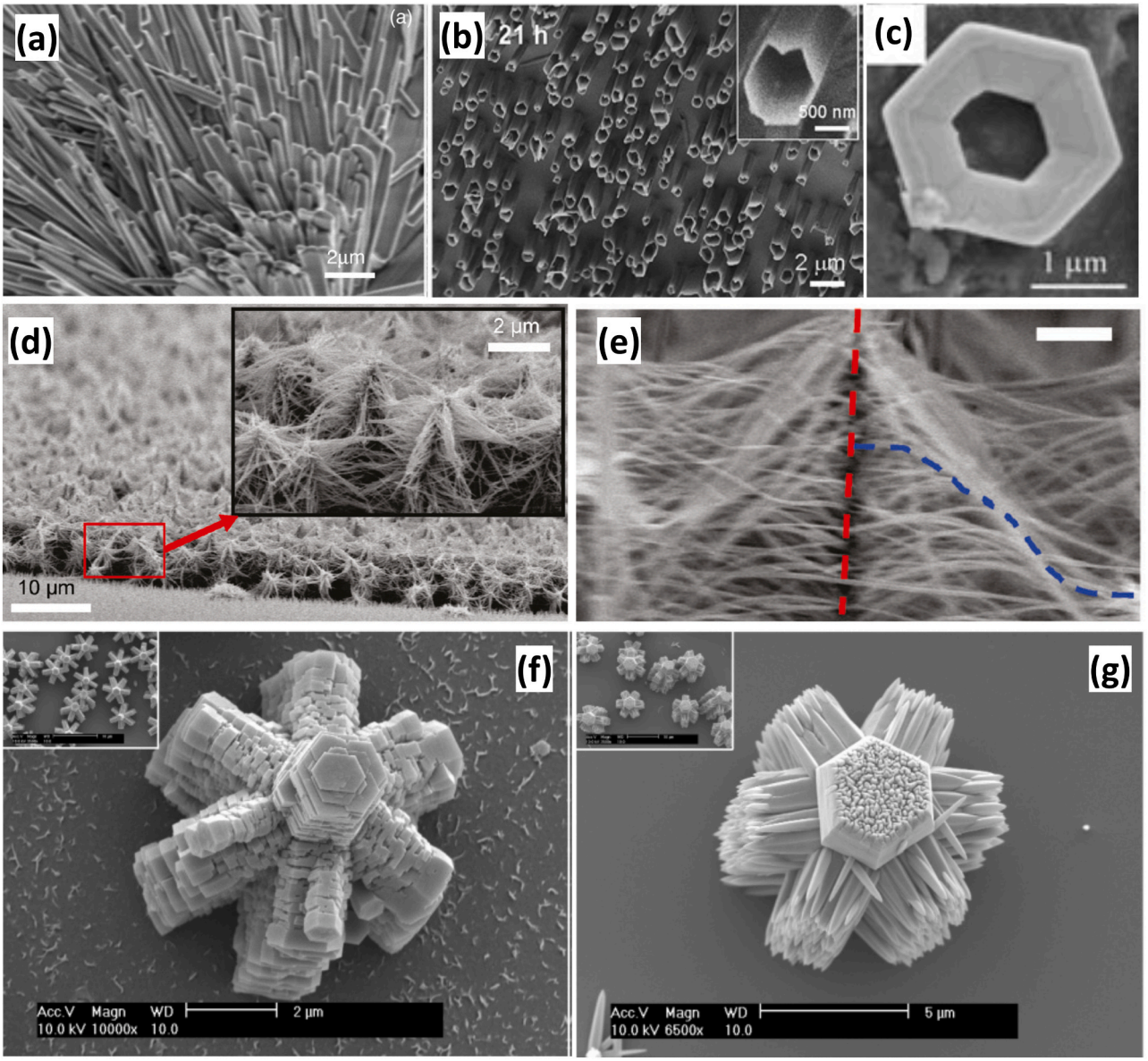

Fig. 10. (a) SEM image of ZnO nanobelts grown by CBD using ethylenediamine. Reprinted with permission from Ref. [174]. Copyright 2007 Elsevier. (b) SEM image of ZnO nanotubes grown by CBD using a lower temperature to selectively activate the dissolution of the polar surface. Reprinted with permission from Ref. [175]. Copyright 2007 The Royal Society of Chemistry. (c) SEM image of a ZnO nanoring grown by CBD using an aqueous/alcohol mixed solvent. Reprinted with permission from Ref. [177]. Copyright 2004 Wiley & Sons. (d) SEM image of a ZnO NW nanoforest grown by CBD with (e) a magnified view of a blackbone. Reprinted with permission from Ref. [180]. Copyright 2011 American Chemical Society. SEM images of ZnO hierarchical nanostructures grown by CBD (f) by first using diaminopropane and then citrate ions or (g) by first using citrate ions and then diaminopropane in a sequential growth process. Reprinted with permission from Ref. [182]. Copyright 2006 American Chemical Society.

physicochemical processes affected by polarity. The first approach to form original nanostructures consists in using chemical additives inhibiting the development of certain planes during the CBD process, which is further combined or not with a selective chemical etching process dissolving certain planes. Nanoplatelets, nanobelts, nanotubes, and nanorings have been fabricated using that approach. Nanoplatelets can be formed by using citrate ions to inhibit the growth along the polar *c*-axis [172] and by using the oriented attachment of nanoparticles [173]. They can further be piled up into nanobelts following an Ostwald ripening process [173]. Nanobelts grown along the polar *c*-axis can also be fabricated by using ethylenediamine as capping agents to inhibit the growth along the $[10\bar{1}0]$ direction as presented in Fig. 10a [174]. Following the formation of NWs by wet chemistry, a selective etching process has been reported to form nanotubes. The preferential dissolution of the polar surface with a higher reactivity stems from the strong reduction of supersaturation at a lower temperature as shown in Fig. 10b [175] or from the formation of H_3O^+ ions using electrodeposition [176]. A modified CBD technique using sodium bis(2-ethylhexyl) sulfosuccinate in a water/1-butanol solvent was developed to form nanorings, as revealed in Fig. 10c [177].

The second approach to form original nanostructures is based on the multi-step CBD process with different chemical additives and/or on the combination of the one-step CBD process with other deposition techniques including ALD for instance. Hierarchical nanostructures with different complex shapes have been fabricated using that approach. Following the CBD of ZnO NWs in the first step, a ZnO seed layer was deposited by ALD as a continuous shell in the second step to induce the nucleation of ZnO NWs along the [0001] horizontal direction in the third step, resulting in the formation of nanotrees [178,179]. By multiplying the number of processes, the formation of nanoforests with a more complex shape was shown, as presented in Fig. 10d, e [180]. The sequential nucleation and growth processes using successive chemical baths with different chemical additives have typically been further developed to form more complex hierarchical nanostructures. Following the growth of ZnO NWs in a standard chemical bath at low temperature, the use of a chemical bath containing citrate ions at a higher temperature has been found to form nanoplatelets on their sidewalls resulting in the fabrication of layered helical nanostructures [172,181]. The shape of complex hierarchical nanostructures is further tunable by adding citrate ions and diaminopropane in two chemical baths, respectively, and by reversing the addition order in the sequential growth process, as presented in Fig. 10f, g [182]. Diaminopropane is well-known to adsorb on the sidewalls of ZnO NWs and to react with water molecules to release hydroxide ions, in turn increasing locally the pH and favoring the formation of seeds inducing the secondary nucleation of NWs to form nanobranches [183].

4. Defect and doping: its polarity dependence

The electrical properties of ZnO NWs grown by CBD has extensively been investigated using terahertz spectroscopy [184], scanning probe microscopy [185], field-effect transistor [186] and four-point probe resistivity [187,188] measurements, as well as scanning capacitance microscopy [189]. ZnO NWs exhibit a high electron density ranging from 5×10^{17} to 3.1×10^{19} cm^{-3} [184–189]. Most of the ZnO NWs in the arrays are thus degenerate and exhibit a metallic conduction. This indicates the formation of a high concentration of defects that are able to be ionized at room temperature. In the fields of piezotronic and piezoelectric devices, this statement has an important consequence as free charge carriers can efficiently screen the piezoelectric potential by creating a potential in the opposite direction, in turn reducing significantly its magnitude. Numerical simulations have shown that the screening effect operates when the electron density is above 10^{17} cm^{-3} [190–193]. The identification and control of the major intrinsic/extrinsic point defects in ZnO NWs grown by CBD along with the development of intentional doping thus represent a critical issue and drastically depends on its polarity.

4.1. Native defect incorporation using chemical bath deposition

Unintentionally-doped ZnO NWs grown by CBD under standard conditions have a high aspect ratio lying in the range of 5–50 and hence exhibit a large surface area, both on the predominant nonpolar *m*-plane sidewalls and minority polar *c*-plane top face. Native point defects represent imperfections in the crystal lattice involving the constituent elements, namely zinc and oxygen. They consist of V_{Zn} and V_O, zinc and oxygen interstitials (Zn_i and O_i), as well as zinc and oxygen anti-sites (Zn_O and O_{Zn}). The energetic of native point defects has extensively been investigated in ZnO over the last two decades, using *ab initio* calculations with different functionals and under distinct approximations. The two comprehensive reviews of Janotti et al. and McCluskey et al. provide for more details regarding the native defect energetics in ZnO using *ab initio* calculations [194,195]. Two typical diagrams reporting the formation energy of native point defects as a function of Fermi level for small and large oxygen chemical potential conditions is reported in Fig. 11a [196]. These defects are likely to be incorporated in the bulk and on the surfaces of ZnO NWs to drive their electronic structure properties and thus their optical and electrical properties. Zn_i acts as a shallow donor with the stable 2+ charge state regardless of Fermi level, but its high formation energy close to the CBM in addition to its high mobility makes its formation very unlikely as isolated species with a large concentration. O_i in octahedral sites acts as a deep acceptor with the stable −2 charge state close to the CBM, but its high formation energy is also against its formation with a significant concentration. A split-interstitial configuration with a neutral charge state is also widely

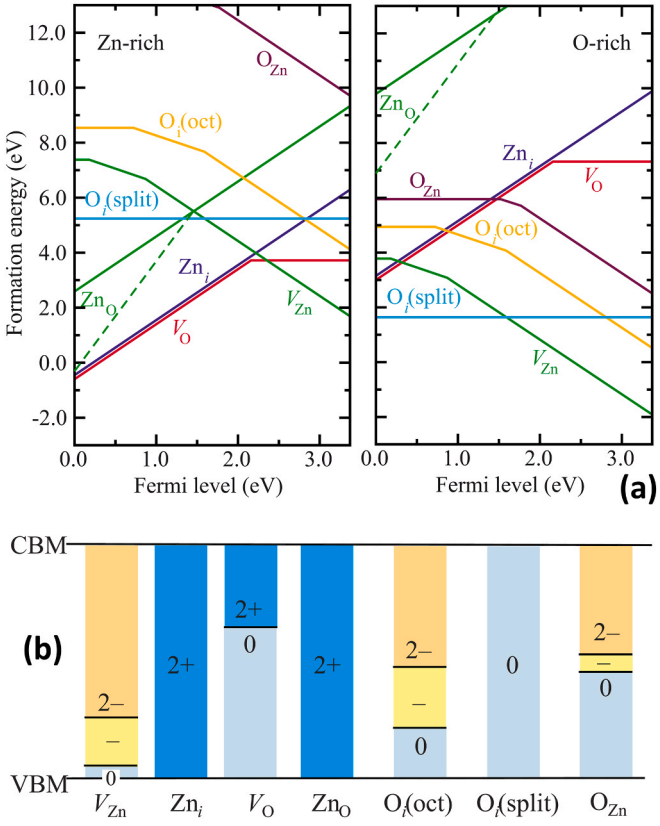

Fig. 11. (a) Formation energy of native point defects in ZnO as a function of Fermi level for small and large oxygen chemical potential conditions. The zero of Fermi level corresponds to the valence band maximum. (b) Thermodynamic transition levels for native point defects in ZnO. Reprinted with permission from Ref. [196]. Copyright 2007 American Physical Society.

reported in the literature. Both antisites are the native defects with the highest formation energy and thus are unlikely to be formed with a large concentration.

Both vacancies are the native defects with the lowest formation energy. V_O is a negative-*U* center with the +1 charge state being never thermodynamically stable; it acts as a deep donor with the stable neutral charge state when the Fermi level is close to the CBM. V_{Zn} exhibits defect states localized on nearest-neighbor oxygen atoms; it acts as a deep acceptor with the stable −2 charge state when the Fermi level is close to the CBM. The range of thermodynamic transition levels for all native point defects in ZnO is indicated in Fig. 11b. The role of V_O and V_{Zn} in the physical properties of ZnO NWs has received a considerable attention over the past decade. A couple of particularities have arisen from the high aspect ratio of ZnO NWs. First, the formation energy of V_O and V_{Zn} was shown to depend on their location in ZnO NWs and possibly on the size of the object [197]. V_O and V_{Zn} have a lower formation energy on the surface of ZnO NWs than in their center owing to more structural relaxation and metal-metal bond formation for V_O and to large structural deformation for V_{Zn}. Besides a lower formation energy at shallow and surface sites as presented in Fig. 12a, b, Deng et al. stated that the migration of V_O is energetically favorable from the bulk to the surface of ZnO NWs and exhibits a low barrier [198]. Both arguments imply a higher concentration of V_O on the surfaces of ZnO NWs. In general, a segregation of vacancies and defects is expected on the surfaces of ZnO NWs. For instance, Watanabe et al. showed the formation of growth sectors resulting from the inhomogeneous incorporation of defects in the center of ZnO NWs [199]. Moreover, Sheetz et al. also found out from *ab initio* calculations that the presence of vacancies in ZnO NWs strongly contribute to the optical absorption in the visible range [200]. Recently, Song et al. interestingly showed by DFT calculations that the concentration of V_O on the surfaces of ZnO NWs strongly depends on its orientation and termination, as shown in Fig. 12c, d [201]. It was found that the formation energy of V_O is much smaller on the non-polar *m*-plane surface than on the Zn-polar *c*-plane with the Zn- or O-terminations, showing that the concentration of V_O is larger on the *m*-plane sidewalls of ZnO NWs than on their top *c*-face. An anisotropy in the work function of these surfaces was also reported, the non-polar *m*-plane surface exhibiting the lowest work function.

Following these theoretical considerations, there has been a lot of efforts to experimentally identify the presence of V_O and V_{Zn} in ZnO NWs by photo-/cathodoluminescence spectra [202,203]. For instance, the green emission band has been attributed to the presence of surface defects in ZnO NWs grown by vapor phase deposition techniques [204–207] and CBD [80]. More recently, the blue emission band was also related to the presence of surface defects in ZnO NWs grown by vapor phase deposition techniques [208]. Nevertheless, the issue is still highly debated and the relationship with the polarity has been controversial. Overall, numerous investigations have assigned the green

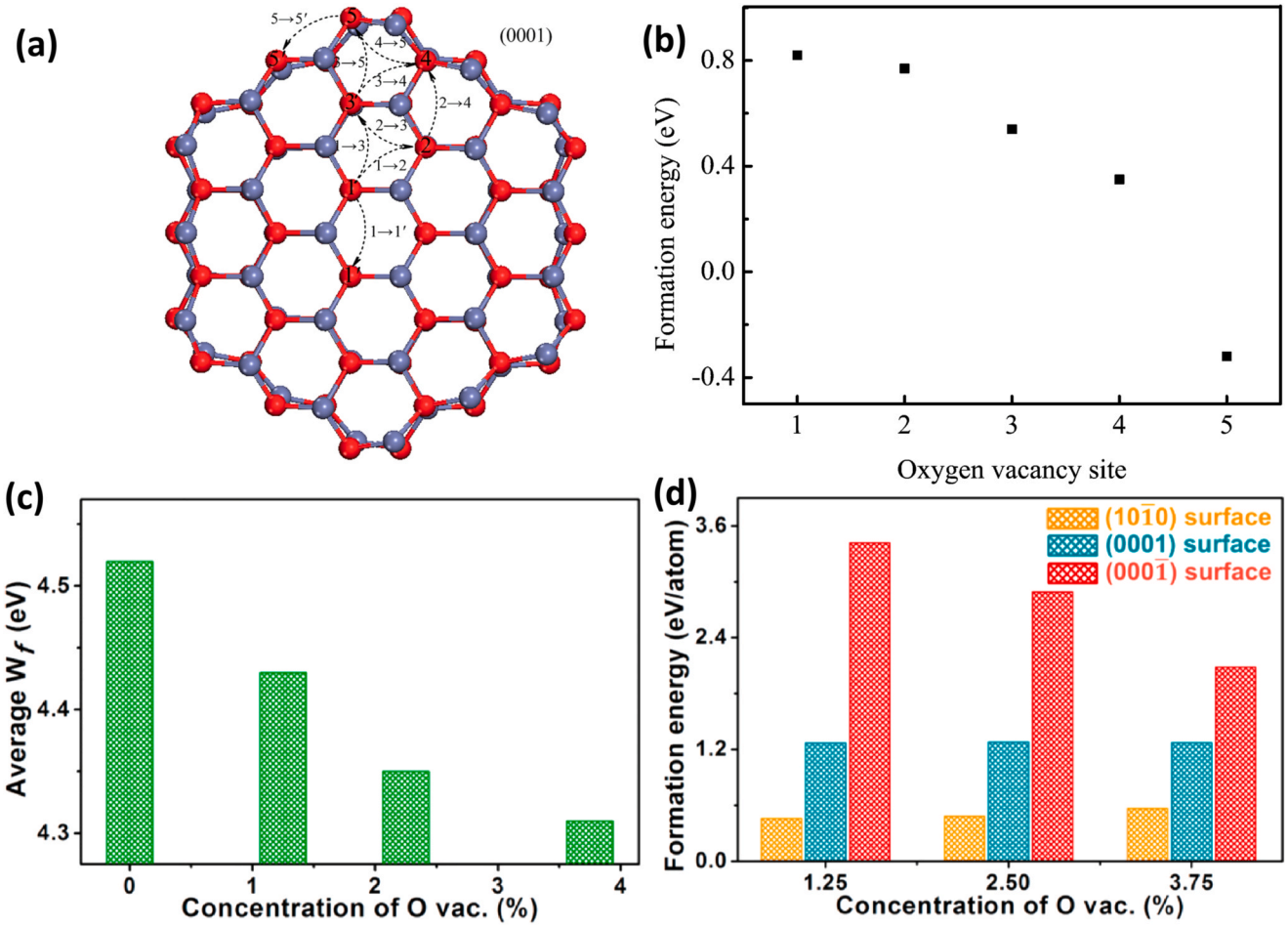

Fig. 12. (a) Axial view of a [0001] ZnO NW. Zinc and oxygen atoms are shown in gray and red, respectively. V_O sites (1–5) define possible migration paths along the basal plane. (b) Formation energy of V_O at different sites of the ZnO NW under zinc-rich conditions deduced from DFT calculations. Reprinted with permission from Ref. [198]. Copyright 2014 The Royal Society of Chemistry. (c) Average work function of the non-polar *m*-plane surface, Zn-terminated Zn-polar *c*-plane surface, and O-terminated Zn-polar *c*-plane surface as a function of the concentration of V_O. (d) Formation energy of V_O (normalized per V_O) as a function of the concentration of V_O for the non-polar *m*-plane surface, Zn-terminated Zn-polar *c*-plane surface, and O-terminated Zn-polar *c*-plane surface. Reprinted with permission from Ref. [201]. Copyright 2021 Elsevier.

emission band to the presence of V_O or V_{Zn} in ZnO NWs grown by CBD, similarly to ZnO single crystals and thin films. Panigrahy et al. attributed the green and yellow emission bands to V_O^+ and V_O^{2+} on the surfaces of ZnO NWs, further leading to magnetization phenomena [209]. Kushwaha et al. ascribed the green emission band to V_O^+ on the surfaces of ZnO NWs, further resulting in poor dark conductance and higher photo-conductance phenomena [210]. Wong et al. showed that V_O occurs on the surfaces of ZnO NWs, but also in the annulus region beneath the surfaces [211]. In contrast, Tam et al. attributed the green emission band to the presence of V_{Zn} on the surfaces of ZnO NWs [79]. Barbagiovanni et al. attributed the blue, green, and orange emission bands at 2.52, 2.23, and 2.03 eV to V_{Zn}^{2-}, V_O^+, and V_O in the bulk of ZnO NWs [212]. Park et al. investigated the presence of vacancies in thin and thick ZnO NWs [213]. An alternative assignment was proposed by Hsu et al. attributing the yellow-orange emission band to the excess oxygen in the bulk of ZnO NWs [214]. Correlatively, Anantachaisilp et al. attributed the red and green emission bands to V_{Zn} and V_O, respectively [215]. Djurisic et al. attributed the red emission band to V_{Zn} defect complexes [80]. Overall, the involvement of V_O in the visible emission bands is still highly controversial. The most recent *ab initio* calculations have shown that V_O does not lead to any emission levels above 1 eV in photo-/-cathodoluminescence spectroscopy [216], which questions its assignment to the green emission band in the experimental data. Instead, recent *ab initio* calculations reporting the emission levels of V_{Zn} with different charge states in ZnO have revisited the assignment of the red and green emission band. It has been found that V_{Zn}^{2-} exhibits an emission level at 1.60 eV close to the red emission band, while the V_{Zn}^-, V_{Zn}^+, and V_{Zn}^{2+} have emission levels at 2.19, 2.48, and 2.53 eV, namely in the yellow-green emission band [188]. As a result, ZnO NWs grown by CBD under standard conditions have a significant density of V_{Zn} in their bulk and on their surfaces. The addition of ammonia during the growth by CBD to tune the pH is also expected to influence the visible emission bands and hence the incorporation of vacancies [217]. Eventually, it is well-established that V_O as a deep donor and V_{Zn} as a deep acceptor

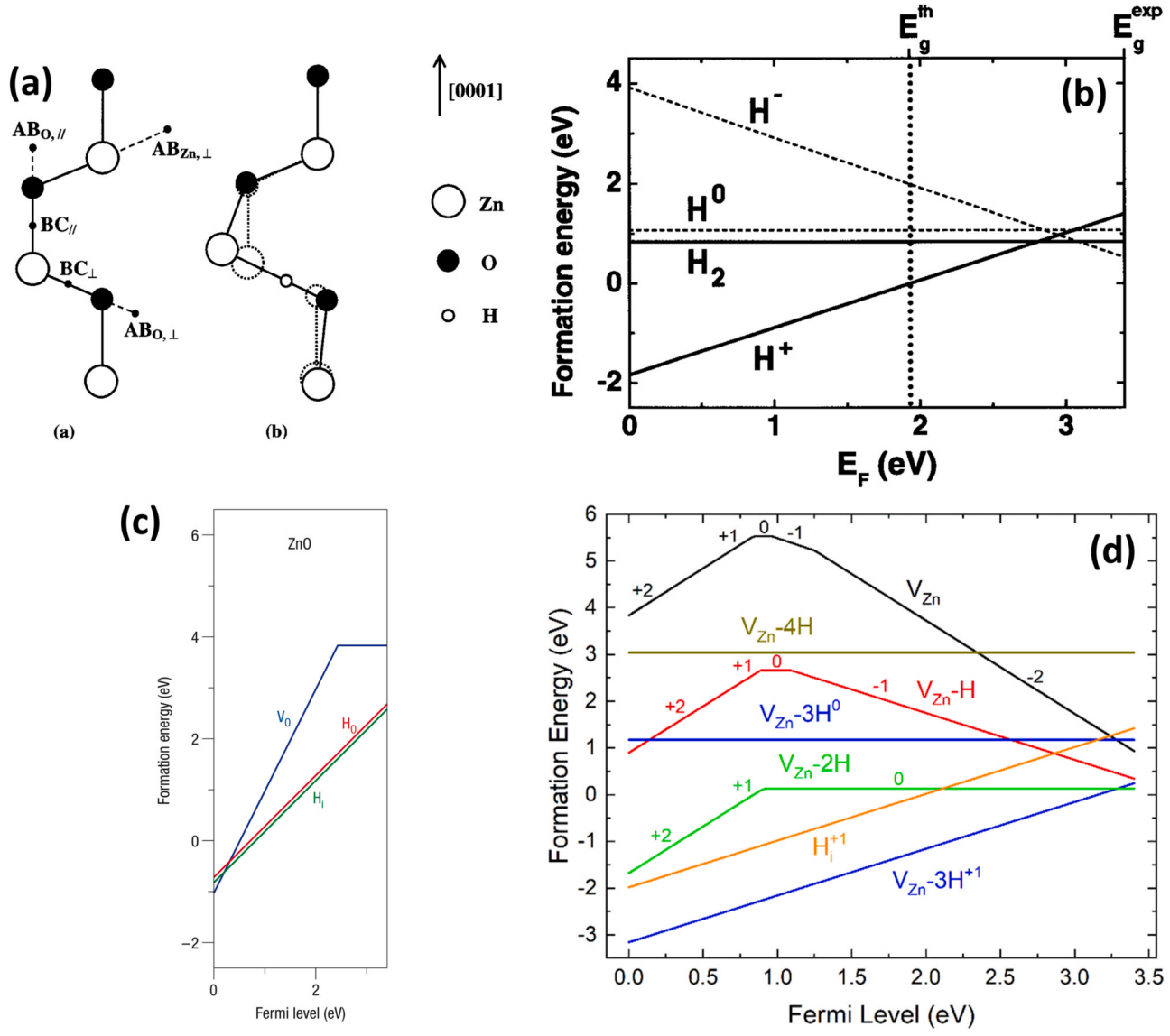

Fig. 13. (a) Schematic representation of the ZnO wurtzite structure, and the sites on which H_i can incorporate. BC indicates the bond-center sites, AB indicates the anti-bonding sites. (b) Relaxed atomic positions of hydrogen and host atoms in the BC⊥ configuration. Ideal lattice position are shown in dotted lines. Reprinted with permission from Ref. [218]. Copyright 2000 American Physical Society. (c) Formation energy of H_O in ZnO as a function of Fermi level for oxygen-poor conditions. Reprinted with permission from Ref. [219]. Copyright 2007 Nature Publishing. (d) Formation energies of hydrogen-related defects in ZnO as a function of Fermi level for intermediate oxygen chemical potential conditions. The zero of Fermi level corresponds to the valence band maximum. Reprinted with permission from Ref. [188]. Copyright 2020 American Chemical Society.

cannot account for the n-type conductivity of ZnO NWs associated with a high electron density and hence are not so critical in the piezotronic and piezoelectric properties of ZnO NWs. Instead, both V_O and V_{Zn} are believed to play a considerable role in the UV sensing and photocatalytic properties of ZnO NWs involving specific processes on the surfaces.

4.2. Hydrogen incorporation using chemical bath deposition

The CBD of ZnO NWs typically occurs in a hydrogen-rich medium that is full of hydroxide ions and water molecules. Moreover, the crystallization process involves the dehydration of $[Zn(H_2O)_6]^{2+}$ ions [143,

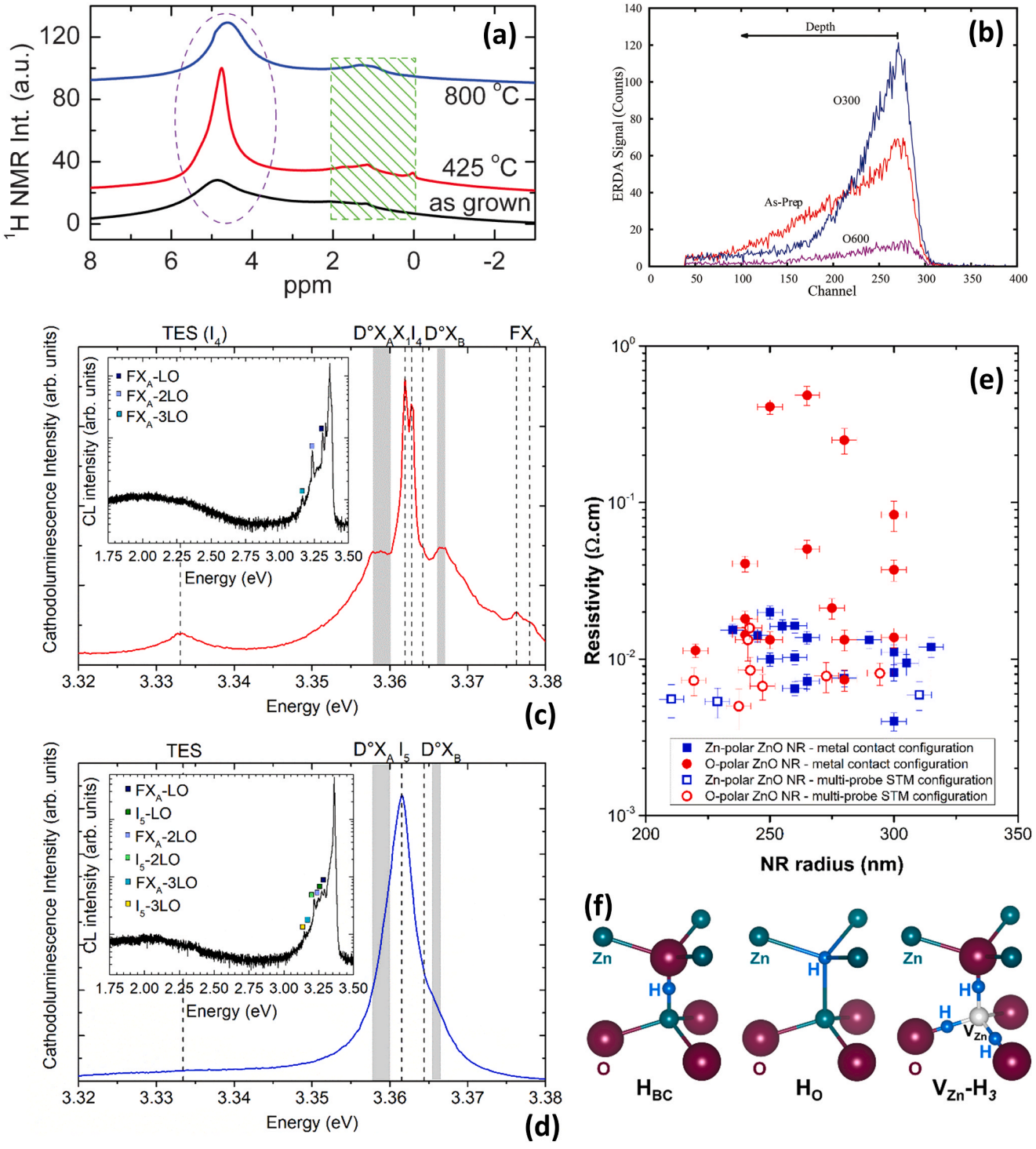

Fig. 14. (a) ^{1}H nuclear magnetic resonance spectra of as-grown ZnO NRs by CBD and annealed ZnO NRs in air. Reprinted with permission from Ref. [230]. Copyright 2011 The Royal Society of Chemistry. (b) Elastic recoil detection analysis spectra of as grown ZnO NWs by CBD and annealed ZnO NWs under oxygen atmosphere. The peak around channel 275 is from surface H, while the lower channel number provides H in the bulk of ZnO NWs. Reprinted with permission from Ref. [212]. Copyright 2016 The Royal Society of Chemistry. 5 K cathodoluminescence spectra of (c) O- and (d) Zn-polar ZnO NRs highlighting the NBE emissions. Both insets show 5 K cathodoluminescence spectra over a broader energy range. (e) Four-point probe resistivity measurements of O- and Zn-polar ZnO NRs as a function of their radius for the patterned metal contact and multi-probe scanning tunneling configurations. (f) Major hydrogen-related defects involved in ZnO NRs grown by CBD. Adapted from Ref. [187]. Copyright 2018 American Chemical Society.

163,165]. As a result, hydrogen-related defects appear as the most likely candidates to drive the electronic structure properties of ZnO NWs by CBD.

Since the 2000's, hydrogen-related defects have been more and more emphasized as the predominant source of n-type conductivity in ZnO [194,195]. Hydrogen interstitial (H_i) exhibits a unique positive charge state over the expected range of Fermi level and acts as a shallow donor with a very low formation energy in both bond-center (H_{BC}) and anti-bonding (H_{AB}) configurations, as presented in Fig. 13a, b [218]. The preferential sites favor the incorporation of hydrogen interstitials strongly binding to an oxygen atom and thus forming an O–H bond with a length of 0.99–1.01 Å. In contrast to many other semiconductors, H_i does not play the role of an amphoteric impurity precluding its role as an effective dopant. Additionally, substitutional hydrogen on an oxygen lattice site (H_O) also exhibits a unique positive charge state over the expected range of Fermi level and acts as a shallow donor with a very low formation energy, as shown in Fig. 13c [219]. H_O typically forms a multicentre bond where hydrogen is equally bonded to the four nearest-neighbor zinc atoms. Furthermore, more recent *ab initio* calculations have revealed the significance of considering zinc vacancy – hydrogen (V_{Zn}-*n*H) defect complexes, where *n* is the number of involved H_i and typically lies in the range of 1–4 [216,220–224], as presented in Fig. 13d [188]. The (V_{Zn}-H) complex acts as a deep acceptor with a −1 charge state and fairly low formation energy when the Fermi level is close to the CBM. The (V_{Zn}-2H) complex is neutral and exhibits a low formation energy over a broad range of Fermi level. Both defect complexes are liable to form in ZnO, but their electrical activity is low at room temperature. In contrast, the (V_{Zn}-3H) complex acts as a shallow donor with a +1 charge state and exhibits a very low formation energy regardless of the Fermi level in the bandgap. This suggests its massive formation in ZnO along with a large electrical activity together with H_{BC} and H_O. The (V_{Zn}-4H) complex with a stable neutral charge state has a fairly high formation energy regardless of the Fermi level in the bandgap and thus does not play a significant role.

The involvement of hydrogen in the electronic structure properties of ZnO NWs grown by CBD has first been suggested through the presence of hydroxyl groups on their surfaces [80,202]. Numerous investigations have shown the effects of post-deposition treatments under hydrogen atmosphere and plasma on the properties of ZnO NWs grown by CBD to passivate V_O and V_{Zn} and likely form (V_{Zn}-*n*H) complexes as well as to increase their conductivity [215,225–229]. This has suggested that a hydrogen incorporation may occur during their growth by CBD. Huang et al. revealed that the presence of hydrogen in ZnO NWs grown by CBD using nuclear magnetic resonance and explored their stability as a function of annealing temperature [230], as shown in Fig. 14a. Urgessa et al. identified the predominance of the I_4 line assigned to H_O in the near-band edge emission region of ZnO NWs grown by CBD and investigated their stability as a function of annealing temperature up to 450 °C [231]. Barbagiovanni et al. measured the presence of hydrogen in ZnO NWs grown by CBD using elastic recoil detection analysis and investigated their stability as a function of annealing temperature under oxygen atmosphere [212], as revealed in Fig. 14b.

More recently, Villafuerte et al. showed the presence of hydrogen in as-grown ZnO NWs using Raman spectroscopy and revisited the assignment of the visible and ultra-violet emission bands in luminescence spectroscopy using density functional theory (DFT) calculations [188]. The red-orange and yellow-green emission bands at 1.86 and 2.25 eV were assigned to the presence of (V_{Zn}-H) and (V_{Zn}-2H) defect complexes in the bulk of ZnO NWs, respectively. In contrast, the green-blue emission band around 2.65 eV was attributed to the presence of V_{Zn}, (V_{Zn}-H), and (V_{Zn}-2H) defect complexes with different charge states on the surfaces of ZnO NWs where holes migrate and are in high concentration under UV illumination. By using pre-patterned ZnO single crystals with the same domains to leave polarity as the only varying parameter, Cossuet et al. investigated in detail the optical properties of O- and Zn-polar ZnO NRs [187]. It was revealed that the NBE emissions of O- and Zn-polar ZnO NRs are dominated by the I_4 and I_5 lines related to H_O and (V_{Zn}-3H) defect complex, respectively, along with the line at 3.360 eV attributed to H_{BC}, as shown in Fig. 14c, d. The X_1 line characteristic of the O-polarity of ZnO was pointed out as well in a high resolution spectrum of O-polar ZnO NRs [50]. The differential incorporation of hydrogen-related defects results in a significant difference of their electrical conductivity: Zn-polar ZnO NRs were found to be much more conductive than O-polar ZnO NRs as presented in Fig. 14e, which is basically contrary to what was previously observed in ZnO thin films epitaxially grown by chemical vapor deposition [232]. This indicates that the incorporation mechanisms of dopants depend on the growth medium. The major hydrogen-related defects in ZnO NWs and NRs grown by CBD are summarized in Fig. 14f. More recently, Lord et al. showed that the cathodoluminescence spectra of O- and Zn-polar ZnO NWs strongly differ following an oxygen plasma treatment [233]. Such a treatment is favorable for producing high energy oxygen ions and thus establishing oxygen-rich conditions. They can fill the vacant oxygen sites and hence reduce the density of H_O in O-polar ZnO NRs, decreasing in turn the intensity of the related I_4 line. Also, the massive incorporation of V_{Zn} typically reduces the coordination of the (V_{Zn}-*n*H) defect complex. This leads to the decrease in the intensity of the related I_5 line assigned to (V_{Zn}-3H) and to the increase in the red-orange and yellow-green emission bands assigned to (V_{Zn}-H) and (V_{Zn}-2H) defect complexes. As a consequence, the oxygen plasma treatment is associated with a decrease in the NBE over visible band intensity ratio while significantly decreasing the electrical conductivity of ZnO NRs, for which the difference coming from the O- and Zn-polarity still holds. This opens many perspective to engineer the hydrogen-related defects in ZnO NRs grown by CBD while taking their polarity into account in such processes.

4.3. Intentional doping with extrinsic elements using chemical bath deposition

The control of the electrical and optical properties of ZnO NWs is strongly required for piezotronic and piezoelectric devices. In addition to the crucial role of hydrogen in the related electronic structure properties of these NWs, the intentional doping appears as a critical issue for the monitoring of these properties. Depending on the devices targeted, the intentional incorporation of shallow donors or shallow acceptors belonging to Group III/VII and I/V elements of the periodic table may help to control the resistivity and mobility of ZnO NWs to name a few. The doping of ZnO has been a long debate over the last three decades [113,194,195] and we concentrate our discussion on the issues related to the CBD process and polarity of ZnO NWs. In the CBD process, the growth medium in aqueous solution is strongly polar and introduces additional forces including electrostatic interactions, which must be considered for ensuring an effective doping of ZnO NWs. In 2011, Joo et al. showed that the introduction of ancillary metal sulfates in the bath forms negatively- or positively-charged ion complexes, which can monitor the aspect ratio of ZnO NWs to a value ranging from 0.1 to 100 [234]. The use of A-type (*e.g.*, Cd, Cu, Mg, and Ca) and B-type (*e.g.*, Al, Ga, In) ion complexes favor attractive electrostatic interactions at a high pH value of 11 with the negatively- and positively charged *c*-plane faces and *m*-plane sidewalls of ZnO NWs, respectively, as shown in Fig. 15a. The key point here is that the value of the IEP, defining the pH at which a surface is neutral through an equal number of negative and positive charges [91,92], is not the same between the polar *c*- and nonpolar *m*-planes [90,93,94]. This offers a pH window where the *c*-plane faces of ZnO NWs and their *m*-plane sidewalls do not exhibit the same charge sign nor the same magnitude defined by the zeta potential. Although the possible doping of ZnO NWs was excluded by Joo et al. owing to the low temperature used in the CBD process [234], this approach has opened many perspectives.

A typical strategy has thus emerged for the effective doping of ZnO NWs. By monitoring the pH in a range where the ion complexes

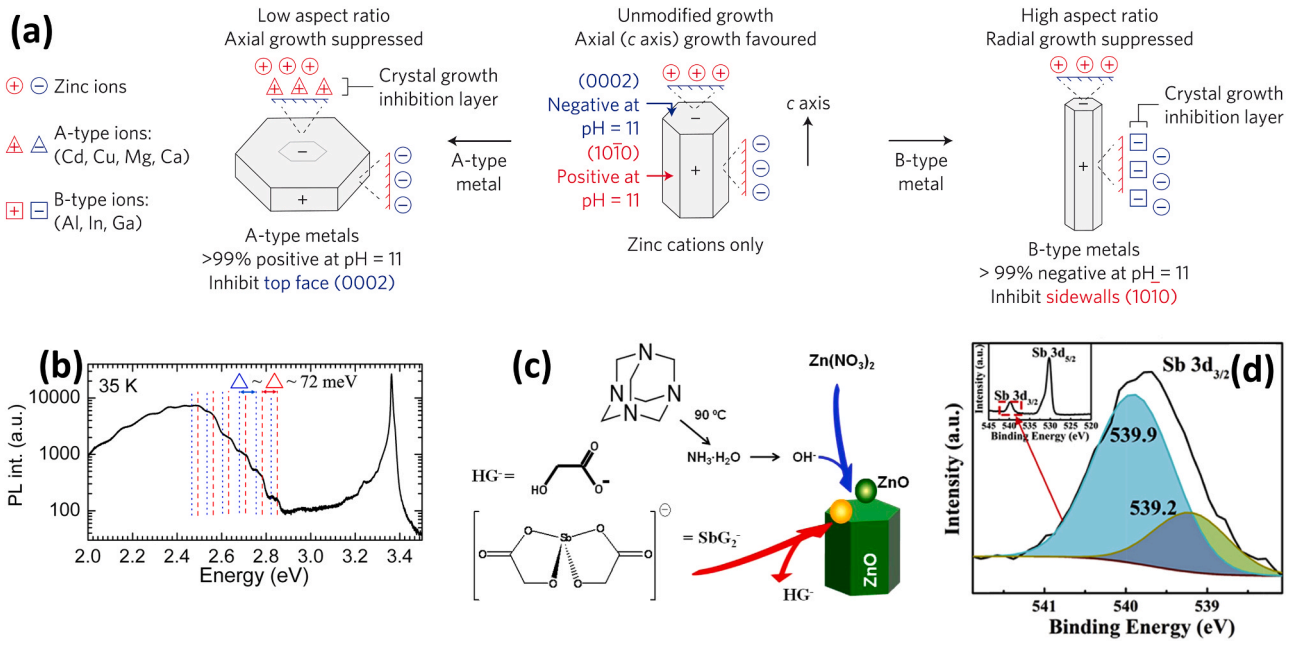

Fig. 15. (a) Mechanism of control by non-zinc metal sulfates in the bath solution. A-type cations suppress axial growth at the negatively-charged *c*-plane top face. B-type anions suppress radial growth at the positively-charged *m*-plane sidewalls. Reprinted with permission from Ref. [234]. Copyright 2011 Nature Publishing. (b) 35 K photoluminescence spectrum of Cu-doped ZnO NWs after annealing in air at 800 °C. Reprinted with permission from Ref. [235]. Copyright 2013 American Institute o Physics. (c) Molecular structure of SbG_2^- and a schematic diagram showing the incorporation of Sb into ZnO NWs. SbG_2^- ions diffuse to the growing *c*-plane faces of the growing ZnO NW and get adsorbed. HG^- ions leave the surface thereafter. Reprinted with permission from Ref. [236]. Copyright 2011 Institute of Physics Publishing. (d) X-ray photoelectron spectroscopy spectrum of Sb-doped ZnO NWs at the Sb 3d peak showing the two Sb valence states. Reprinted with permission from Ref. [237]. Copyright 2019 Elsevier.

containing the dopant and the surface of ZnO NWs exhibit an opposite charge, the adsorption of ion complexes opens a way for the direct incorporation of the dopant with or without any post-deposition thermal annealing. The strategy has basically been tested with Group III elements belonging to B-type ions according to Ref. [234]. It has been reported that the formation of $Al(OH)_4^-$ and $Ga(OH)_4^-$ ion complexes in a high pH region affects the development of the *m*-plane sidewalls of ZnO NWs through their direct adsorption [238,239]. $Al(OH)_4^-$ ion complexes have been found to inhibit the radial growth of ZnO NWs, while Ga $(OH)_4^-$ ion complexes have been shown to enhance their radial growth. More importantly, the direct incorporation of Ga was shown in as-grown ZnO NWs through the formation of Ga_{Zn} [239], while the incorporation of Al required a post-deposition thermal treatment under oxygen atmosphere at 200 °C and thus was thermally activated [240]. The involved mechanisms are very dependent upon the pH value [238,239], such that the only introduction of chemical additives containing the dopant in the bath is not sufficient to ensure its incorporation. The present approach thus leads to the effective doping of ZnO NWs, but the influence of the polarity on these mechanisms is still unknown because the incorporation of the dopant using B-type ions is made through the nonpolar *m*-plane sidewalls. It can further be developed for the incorporation of shallow acceptors or other elements like Mg as A-type ions according to Ref. [234] through the polar *c*-plane faces for decreasing the high density of free electrons in their center that is critical for piezoelectric devices through the detrimental screening effects [190–193]. Hassanpour et al. reported an analysis of the addition of chemical precursors containing metal transitions including Ni, Mn, Co, Cu, Cr on the structural and optical properties of ZnO NWs grown by CBD without modifying the pH [241]. The amount of Mg, Ni and Co in the ZnO NWs was found to be larger than the other dopants. Rakhsha et al. investigated the Cu and Ag doping of ZnO NWs grown by CBD, showing a larger amount of dopants at the low pH value of 6.8 than at the high pH value of 10.8 [242]. The Cu doping of ZnO NWs was further shown to result in the occurrence of a typically structured green luminescence band exhibiting a high coupling with LO phonons, as revealed in Fig. 15b [235]. Interestingly, several investigations have been focused on the Sb doping of ZnO NWs grown by CBD by tailoring the chemical additives to form the $(Sb_{Zn}\text{-}2V_{Zn})$ defect complex as a shallow acceptor [243]. Briscoe et al. prepared the dopant solution by dissolving Sb acetate in ethylene glycol to subsequently achieve the Sb incorporation into ZnO NWs by CBD [244]. Wang et al. initially mixed sodium hydroxide and glycolic acid to form sodium glycolate and then dissolved Sb acetate to prepare the dopant solution [236]. It was proposed that Sb glycolate (SbG_2^- ions) in the chemical bath adsorb on the *c*-plane faces of ZnO NWs, leaving behind individual Sb atoms for their incorporation following the desorption of glycolate ligands (HG^- ions), as presented in Fig. 15c. Pradel et al. recently investigated in details the microstructure of Sb-doped Zn NWs by CBD, revealing the presence of voids surrounding $Zn_7Sb_2O_{12}$ region and their processing using thermal annealing [245]. Using the present approach, the formation of $(Sb_{Zn}\text{-}2V_{Zn})$ defect complexes in ZnO NWs was shown by X-ray absorption near-edge structure along with the Sb^{5+} states by X-ray photoelectron spectroscopy and DFT calculations, as presented in Fig. 15d [237]. Interestingly, Rathore et al. reported the incorporation of a higher content of Mg in Zn-polar ZnO NWs than in O-polar ZnO NWs owing to the differential axial growth rate [246]. The nucleation of inversion domain boundaries induced by Mg was suggested in O-polar ZnO NWs following conductive AFM (CAFM) measurements. Generally, the chemistry of precursors containing the dopant element along with the stability of parasitic phases originating from the dopant element and the nucleation of structural defects requires a precise optimization of the CBD conditions for developing the doping with each targeted element. The effects of the dopant element on the polarity of ZnO NWs are still unknown, despite its primary importance for piezotronic and piezoelectric devices.

5. Contact and device properties: its polarity dependence

5.1. General considerations and context

Many of the devices utilizing CBD NRs require integration into an electrical circuit with some sort of junction, typically, a p-n junction for optical devices or metal-semiconductor contacts to form an Ohmic or Schottky interface and control the flow of electric charge. While detailed studies of the fundamental properties of these junctions in relation to polarity-specific NRs remain rare, Schottky contacts and the *c*-axis NR orientation have proved critical in the function of piezotronic and piezoelectric devices [21]. The potential barrier provided by a Schottky contact in piezoelectric devices prevents the screening of static charge by free carriers from the circuit allowing the maximum piezoelectric potential to be generated before the flow of an electric current. One might expect that the characteristics of the contact interface will be influenced by the crystal polarity of the NR, especially if the contacts are formed on the polar facets such as in vertical arrays [233,247]. The crystal polarity also dictates the sign of the generated piezoelectric potential and should be considered to determine at which end of a NR to place a Schottky contact or p-n junction [248]. This is important to achieve in order to maximize the efficiency of devices that can be hindered by variations in ZnO polarity, which can differ depending on the growth method [151,160]. The relationship of piezoelectric output and polarity orientation was demonstrated by Wen et al. on ZnO thin films with high *c*-axis alignment [249]. When the thin films were compressed and released, the recorded voltage output showed a switch in voltage polarity depending on the *c*-axis orientation with respect to the circuit polarity, as seen in Fig. 16a–c. A ZnO thin film that had random grain orientations or grains with opposing crystal polarity would show a significantly reduced output voltage. The work went on to show with two contacts patterned on the uppermost surface of the thin film that the contact properties could be modulated by strain that created a positive or negative piezoelectric potential at the contact interfaces.

It is fundamental to the field of piezotronics that the potential barrier of an electrical contact can be influenced by the piezoelectric potential that modulates the current-voltage characteristics, depending on the piezoelectric polarization induced by strain [250,251]. In turn, for symmetrical contacts at the ends of a single NR, the current-voltage behavior under strain depends on the crystal polarity of the ZnO that dictates which contact behaves as the greater Schottky barrier [252]. A thorough review by Pan et al. covers the fundamental material properties and electrical contact properties of ZnO NRs that have enabled more recent piezotronic and piezo-phototronic devices [21]. In that review, the authors highlight work showing that piezoelectric charges can modify the potential barrier at a p-n junction and metal-semiconductor interface tuning the electrical behavior of the device.

In many of the vertically integrated piezoelectric nanogenerators (VING) involving NR arrays, the formation of high quality Schottky contacts to the NR tips is difficult, but essential to maximizing the energy density that is recoverable. There are some excellent reviews that cover the history and variety of nanostructured piezoelectric nanogenerators and the underlying electromechanical properties [19,20]. With such a high number of NRs that are required to interface with one common top contact, the range of SBHs from NR-to-NR will be broad and the variable nature of the individual depletion regions will obviously be detrimental to the device efficiency when the range of contact properties cannot be optimized or reduced. Additionally, if the polarity of the NRs is mixed or unknown, a further reduction in recoverable energy is to be expected. In the case of laterally integrated piezoelectric nanogenerators (LING) involving single NRs, the metal or polymer contacts are patterned onto one end of the NRs predominantly contacting the NR side *m*-plane facets with usually some portion interfacing with the polar end facets [248, 253]. In our considerations so far, it is assumed that O-polar and Zn-polar NRs are compositionally and structurally equivalent, but due to differing reaction rates at the O-polar and Zn-polar facets, this cannot be taken for granted. In recent years, the importance of the polarity-controlled growth of NRs has emerged [50] to provide polarity-dependent growth rate [57], morphology, defects [187], and subsequent electronic and electro-mechanical properties [233], as presented in the last sections. In this section, we will briefly highlight areas in which polarity-specific NRs can offer an advantage or improvement in quality of the electrical contacts and devices.

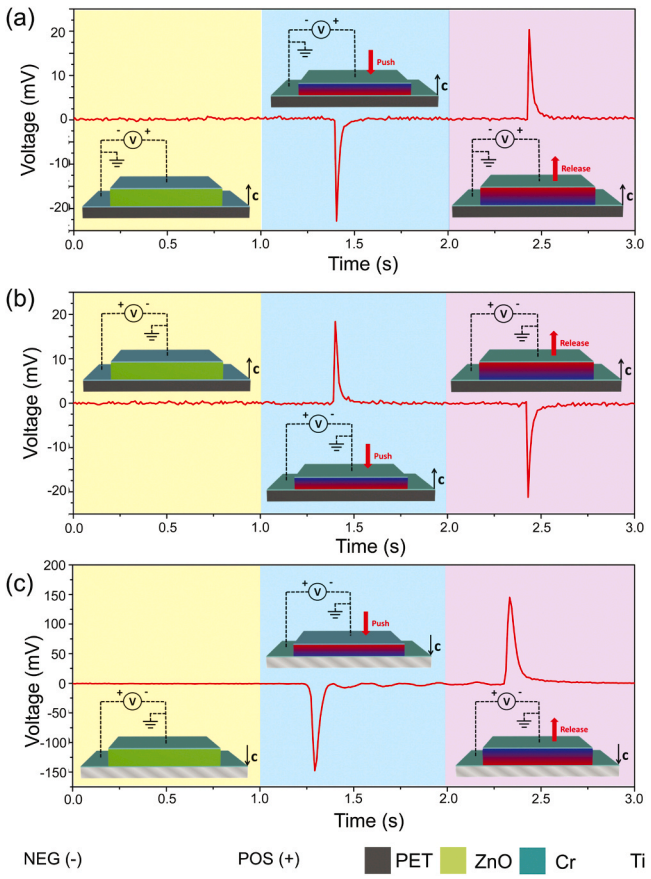

Fig. 16. Experiments on *c*-axis orientated ZnO thin films revealing a switch in piezoelectric voltage output when the circuit polarity is reversed from (a) to (b). (c) A switch in piezoelectric voltage output occurs when the thin film *c*-axis orientation is reversed.
Reprinted with permission from [249]. Copyright 2013 Wiley and Sons.

5.2. Polarity-dependent contact and junction to ZnO nanorods

In general, we can consider four types of contacts, shown in Fig. 17, that, to some extent, include a portion of the polar facets or will be influenced by the NR polarity. In the first three configurations, a large scale contact at the base of a NR array that normally performs as an Ohmic or Schottky contact is used as shown in Fig. 17a, b. The first configuration involves individual contacts to the tips of vertical NRs, such as those that are commonly measured by CAFM, as seen in Fig. 17a. The second and third configurations are based on a large area contact to the tips of the NR array, usually metal Schottky contacts or insulating/capacitive junctions, respectively, as presented in Fig. 17b. In the second configuration, vertical NR arrays are arranged in such a way that each individual NR tip independently interacts mechanically with a metal contact, which can be considered as some portion of the top facet intermittently touching the electrode. In the third configuration, polymer film is coated onto the array as a p-type/capacitive interlayer between the array and metal electrode. The latter configuration consists of single NRs with one Ohmic contact at one end and another p-n/Schottky junction formed to the other NR end or two equivalent metal contacts at

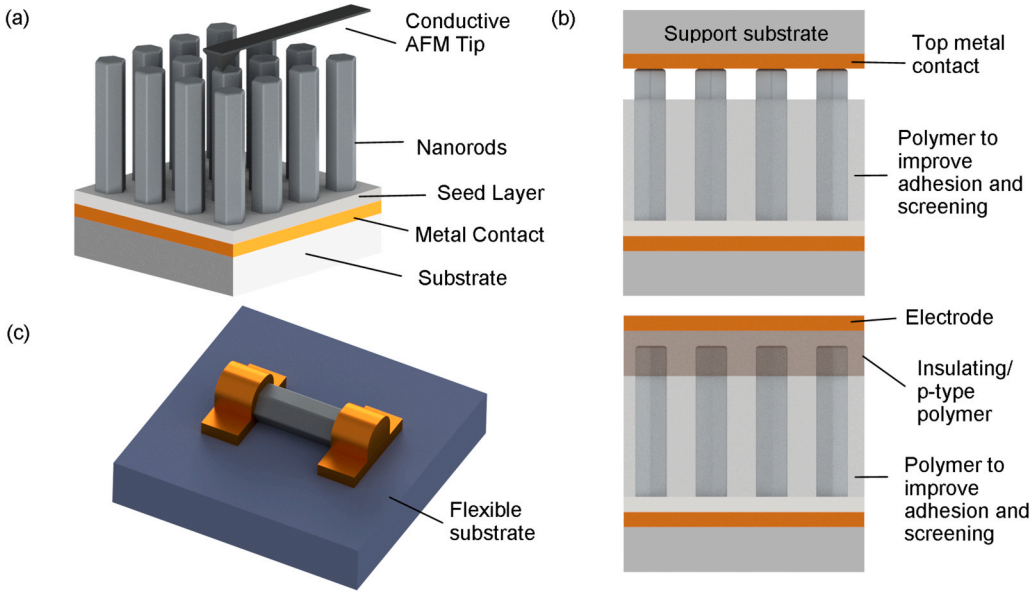

Fig. 17. Schematic diagrams depicting the predominant configurations that electrical contacts and junctions are formed with CBD grown NRs. (a) Metal contacts formed between CAFM tips and the tips of NRs in the as-grown array configuration with a large area Ohmic contact at the array base; (b) in array device applications, a metal film typically interacts with the NR tips to form Schottky contacts or a junction is formed with a p-type/insulating polymer; (c) single NRs are transferred to flexible substrates and metal contacts/ p-type junctions are patterned at the ends of the NR.

either end of flat-lying single NRs, as represented in Fig. 17c, where Schottky barriers are modulated by piezoelectric charge. In the first three array configurations, the lower contact is frequently a transparent conductive oxide substrate/ZnO seed layer that forms a highly conductive Ohmic contact or a metal thin film that forms either an Ohmic or Schottky contact. These contacts are readily fabricated and interfaced with the entire base of the array, as such they are not considered further here.

5.2.1. Contacts to the tips of individual vertical nanorods

There are many studies characterizing metal contacts to vertical ZnO NRs and NWs, however, these works only considered the polarity of the NWs when the piezoelectric properties became of interest particularly with the introduction of piezoelectric energy harvesters. AFM was used extensively in the early experiments measuring the piezoelectric output produced by single vertical NWs in the array configuration. The first experiments were performed on vapor phase deposition grown NWs with Au catalyst tips that formed intimate ready-made Schottky contacts to each individual structure [26]. Later experiments used metal-coated AFM tips to form a metal-semiconductor junction on NRs grown without metal catalyst in the CBD fashion [254]. It is not clear in these early experiments whether there was a suggestion of mixed NR polarity in the arrays that would be indicated by some proportion of the NRs contributing an open circuit potential that opposed the reported output polarity or that may not have produced an output potential at all. Later works showed that it is possible to investigate the predominance of a particular generated potential polarity from individual NRs to provide insight into the mix in NR growth polarity [129]. The contact area is very small when using a CAFM tip sharp enough to interact with individual NRs in an array and as such the current is usually quite low, a few nano-amperes and the measurements can be unstable or erratic. Subsequent analysis is heavily dependent upon the local contact area making it difficult to compare to fabricated contacts that are necessary for devices. However, significant insight has been gained when elastic deformation of vertical NRs with the AFM tip has been coupled with current-voltage experiments to investigate piezoelectric SBH modulation.

CAFM can be used to simultaneously place a conductive tip on the uppermost surface of vertical NRs and measure the current-voltage properties while exerting a compressive force and a variety of external stimuli [256,257]. Lin et al. have used Pt/Ir AFM tips to form a Schottky contact to the tips of patterned vertical ZnO NRs (Fig. 18a), revealing that the NRs exhibited Zn-polar specific piezoelectric polarization under compression that increases the measured SBH (Fig. 18b) [255]. The experiments were compared to the response of an O-polar ZnO film showing opposite piezoelectric polarity and Schottky barrier modulation (Fig. 18c). It was also shown that the SBH modulation by the piezoelectric potential also occurred when the carrier concentration was modulated with UV illumination. Similarly, Han et al. showed the piezoelectric potential modulation of the Schottky barrier is also apparent in vapor phase deposition grown NWs with Au catalyst tips when compressed vertically with an AFM tip [251]. The NWs were considered to have grown in the Zn-polar direction and thus a negative piezoelectric potential was generated at the interface under compression (Fig. 18) increasing the SBH (Fig. 18e, f) and increasing current-voltage rectification under a force of 6 μN. Annealing the Au-NW-Ag structure improved the Ohmic nature of the ZnO-Ag interface and considerably enhanced the overall rectification and force response. This reveals a useful test for measuring the NW polarity because the theory of piezotronics shows a compression of an O-polar NW would not have produced rectification as the piezoelectric potential distribution (Fig. 18d) would have been inverted and acted to reduce the SBH [252]. To overcome any substrate effects, individual free-standing CBD-grown NRs have been contacted at the base with metal pads to record the variation in current output with CAFM when the pillars were deflected by a gas flow [258]. Sahoo et al. investigated the Schottky barriers on the tips of sol-gel seeded CBD-grown NRs with conductive diamond tips measuring the top polar *c*-plane and side nonpolar *m*-plane facets showing the SBH is 0.63 eV and 0.55 eV, respectively [259]. Scrymgeour and Hsu used CAFM with probe tips coated with Ti-Pt and conductive diamond to perform current-voltage measurements on bare ZnO NRs [260]. Both coatings gave non-linear current-voltage characteristics *i.e.* non-Ohmic contact. To form Ohmic characteristics and appreciable currents (μA), the NRs were annealed in H_2/N_2 gas, coated with photoresist (PR), and then the top NR facets were exposed by etching before they were coated with 3 nm Ti and 50 nm Au to provide an Ohmic contact which increased the current by several orders of magnitude. The annealing of the NRs created a highly doped subsurface which provided the low resistance Ohmic contacts. A strong piezoelectric response was correlated to the more resistive NRs by incrementally increasing the positive potential applied to the AFM tip which caused a piezoelectric elongation of the NRs. The authors state the NRs are Zn-polar orientated and there is no data suggesting NRs retracted under a positive tip bias that would indicate O-polar orientation. Measurements by CAFM on as-grown

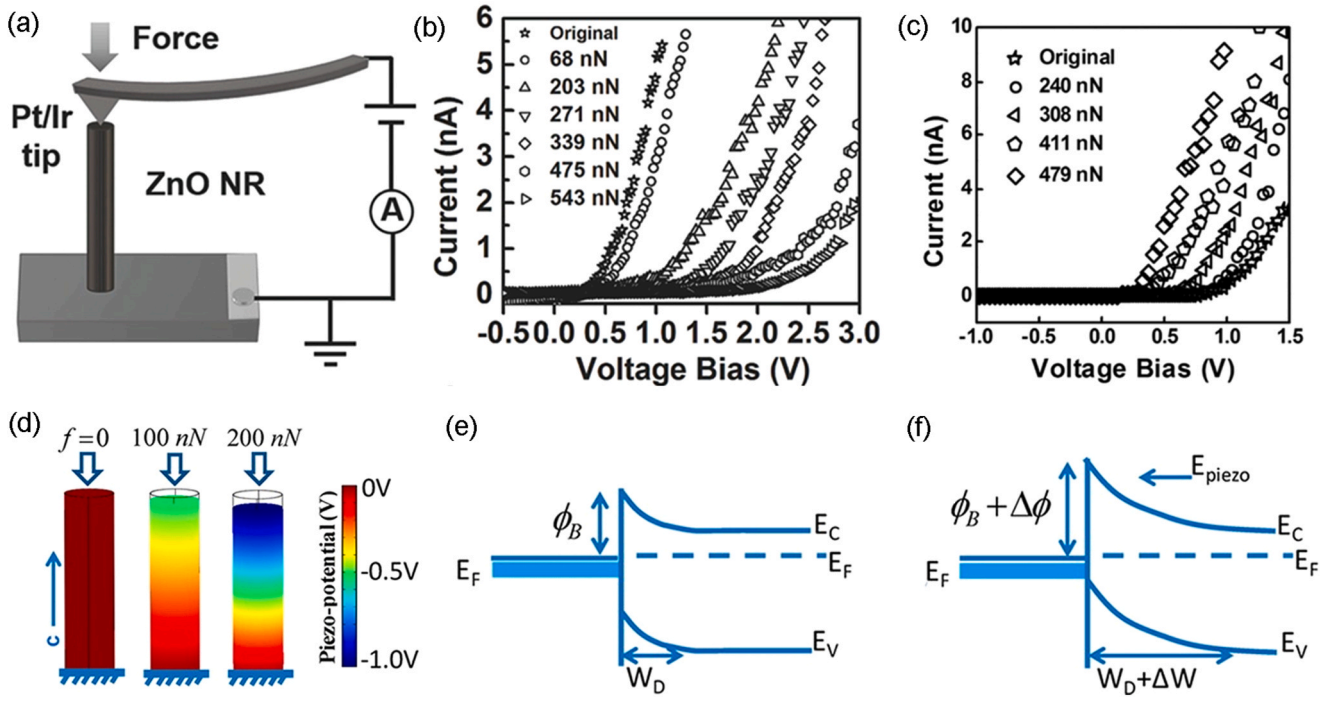

Fig. 18. (a) CAFM experimental schematic combining compressive strain of vertical Zn-polar NRs with current-voltage measurements; (b) increasing compressive strain modulates the Schottky barrier at the NR-tip interface such that the forward-bias current reduces with increasing force indicating a larger barrier height; (c) when compared to an O-polar ZnO wafer, the same experiments show the reverse electrical response such that increasing compressive force increases the forward-bias current. Reprinted with permission from Ref. [255]. Copyright 2017 Wiley & Sons. (d) Finite element method calculation of the potential distribution in a Zn-polar NW under increasing compressive force. (e) and (f) Band diagrams of the NW-tip interface before and under compression, respectively. Reprinted with permission from Ref. [251]. Copyright 2012 Wiley & Sons.

arrays of ZnO NRs typically have small nano-ampere currents at bias up to 10 V most likely due to the small contact area and measurements are usually performed in air. This current magnitude is several orders of magnitude lower than current measured with UHV scanning tunneling microscopy (STM) instruments [261].

Rathore et al. produced one of the few reports to specifically investigate the transport properties of a metallic AFM probe placed onto the tips of polarity-controlled NRs [161]. The electrical measurements reveal a larger SBH is formed on the tips of the Zn-polar NRs, which may show some agreement with the work carried out on ZnO single crystals covered in Section 2.5. However, due to the quite different morphology of the O-polar and Zn-polar NRs, there is an inherent variability in the AFM tip-NR contact area and interface structure and as such it is difficult to assign the recorded variations in transport properties to either polarity-dependent properties or tip-NR interactions. More recently, Lord et al. measured the transport properties of Au contacts deposited onto the tips of polarity-controlled CBD-grown NRs with a multi-probe STM technique [233]. The NRs were grown in patterned arrays with controlled spacing, length and cross-sectional area with comparably flat upper polar surfaces. They found it necessary to use oxygen plasma treatement to improve the Schottky contacts from the as-grown state achieving an effective SBH of 0.43 eV and 0.37 eV on the O-polar and Zn-polar NRs, respectively. It was shown with cathodoluminescence spectroscopy that the oxygen plasma had a different effect on the growth defects that are unique to the O-polar and Zn-polar NRs. The plasma treatment was more effective at quenching the visible-range defects in the O-polar NRs creating a greater improvement in the Au Schottky contacts and reducing the NR electrical conductivity. These measurements showed a vast improvement on similar measurements of vapor phase deposition grown ZnO NWs with or without an Au catalyst that typically show current-voltage rectification between 1 and 10 [262,263].

5.2.2. *Large area contacts to the tips of nanorod arrays*

Vertical array devices, particularly piezoelectric nanogenerators, originally had a top contact fabricated from a metal film such as Au or Ag coated on to a solid substrate to form a Schottky contact with each individual NR [27]. The potential barriers were originally thought to prevent charge leakage, but the models of the mechanisms at play were refined to show the junctions acted to control charge flow and reduce screening of the piezoelectric charge build-up that reduces the piezoelectric potential [193]. Subsequently, the NR arrays have been embedded in insulating or p-type polymer to improve adhesion to the substrate and passivate surface states to further reduce screening improving the maximum voltage output [28,193,254]. In these early experiments, the longer NRs protruded from the polymer matrix, while shorter NRs remained embedded excluding them from the experiments. This is potentially an important aspect especially for array piezoelectric nanogenerators since we know that Zn-polar NRs have a faster growth rate than O-polar NRs [57], which may have excluded O-polar NRs from the majority of measurements including AFM and array device experiments. However, in attempts to increase the output insulating/ semiconductor layers in the form of insulating/p-type polymers between the NRs and electrode were developed which allowed flexibility and for the majority of the NRs to contact the electrode in unison [264]. In further developments, entirely flexible array devices were produced from CBD NRs grown from seed layers on flexible substrates and contacted at the tips by a metal coated flexible film that was pressed on to the array to produce wearable energy harvesters [193,265]. An example of a fully flexible and transparent piezoelectric nanogenerator is shown in Fig. 19a and the NRs that were identified as not contributing to the device output are identified in Fig. 19b, c. In most cases of the top contact, polymers have acted to create a flexible common p-n/blocking junction, while metals were used to form a Schottky contact.

VING devices typically rely on the use of seed layers to ensure the heterogeneous nucleation of ZnO NRs. It was discussed in the previous

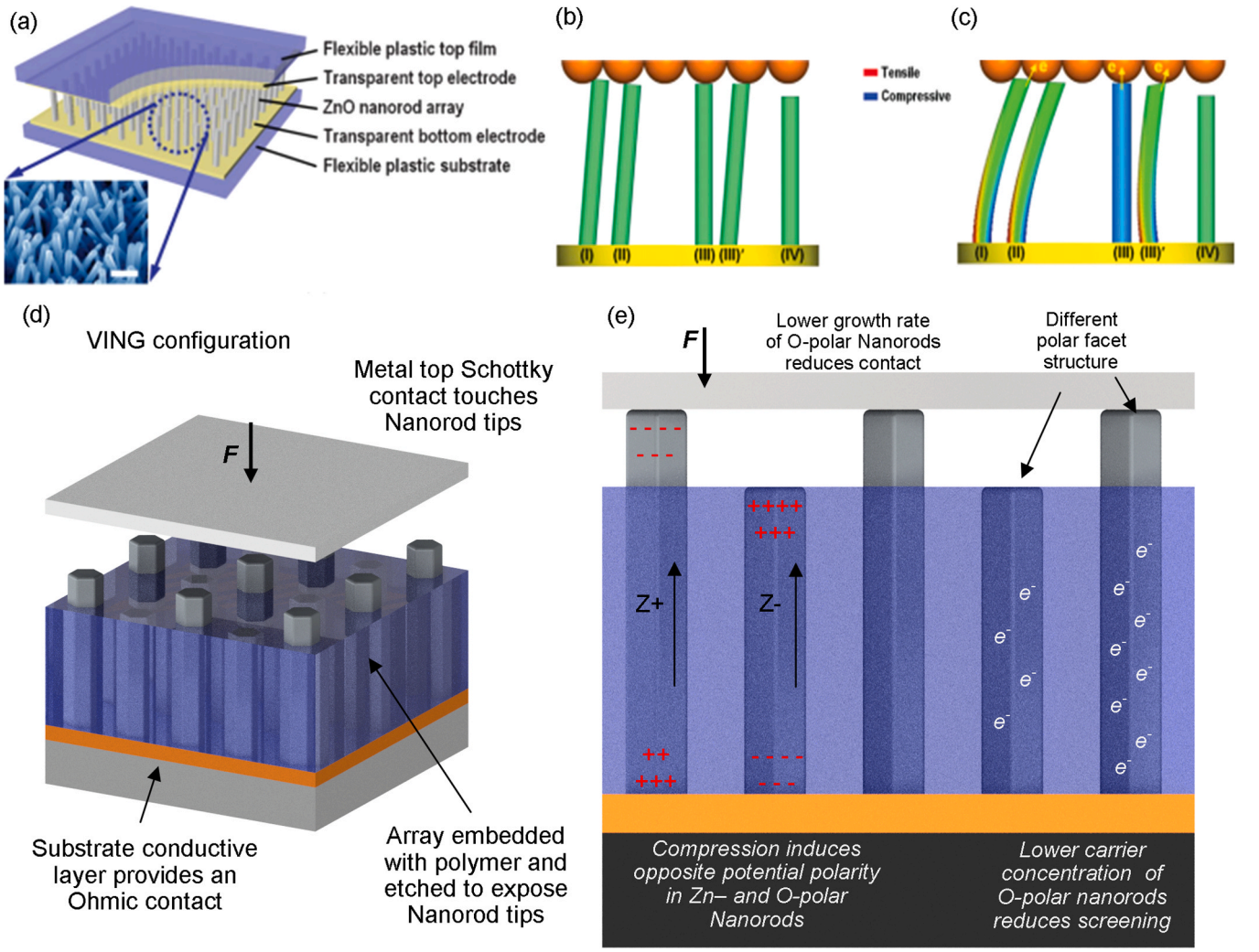

Fig. 19. (a) A schematic diagram showing the components of a transparent and flexible VING. (b) and (c) Schematic diagrams showing four different types of NRs before and after compression and identifying that NRs (II) and (IV) do not contribute to the output. Adapted from Ref. [265]. Copyright 2009 John Wiley & Sons. (d) A schematic diagram showing the common elements of a VING device; (e) the major effects of mixed-polarity NR growth on a VING device including opposite piezoelectric potential polarity, different growth rates reducing the number of NRs touching the top contact, varying polar facet structure affecting Schottky barrier properties, and the lower carrier concentration of O-polar NRs reduces piezoelectric screening.

sections that seed layers can be optimized with high temperature annealing, such that individual seed crystals are predominantly Zn-polar orientated with respect to the substrate, but with a significant fraction that are O-polar orientated [129]. This can be considered as the best case scenario on non-lattice matched substrates and in reality growth may lead to a mixture of both Zn-polar and O-polar NRs when high temperature processes are not appropriate. Furthermore, Guillemin et al. showed that, because of the opposing domains of the seed layer, the polarity of the piezoelectric voltage output will counteract neighboring grains depending on the crystal polarity [151]. Many array devices are grown from seed layers, from which we might expect a mixture of O-polar and Zn-polar NRs and for the O-polar NR voltage output to counteract the Zn-polar NR one. This problem is exacerbated by the fact that O-polar NRs tend to have lower growth rate [57], fewer defects [187], and lower carrier concentration that results in less screening of piezoelectric charges and may produce better Schottky contacts at the NR tip [193,233]. Therefore, the O-polar NRs will likely produce an opposing voltage when a piezoelectric array device is mechanically deformed and may even outperform the Zn-polar NRs in voltage magnitude. This is rarely considered in research works or reviews. These aspects of NR polarity that may affect these devices can be easily understood by considering popular array configurations used for the piezoelectric nanogenerators such as the VING which are summarized in Fig. 19d, e [28].

5.2.3. *Contacts to flat lying single nanorods*

Similar contacting and interlayer materials used on NR arrays have been applied to single lateral NR devices (Fig. 17c) with the metal or polymer/semiconductor acting as a Schottky diode or p-n junction, respectively [248,253]. Schottky contacts have been shown to dramatically improve the response of sensors such as the UV photoresponse increasing the On-Off response ratio and greatly reducing the recovery time. This was achieved by depositing a Pt Schottky contact on an insulating substrate and transferring a ZnO NR to the contact before depositing an Ohmic contact at the other end [266]. In this way, the defect states at the Pt-ZnO interface were sensitive to molecular surface reactions changing the potential barrier. A similar configuration was used to show reverse-biased single NR gas sensors display a large improvement in sensitivity and an increase in Schottky contact rectifying behavior after the adsorption of negatively charged oxygen ions that deplete the NW surface but more crucially alter the SBH [267]. In these examples, the Schottky contact properties are highly sensitive to the exposed NR surface at the edge of the small area contact. The NR surface has a large effect on the transport mechanisms of the Schottky

contact which are not apparent on the same device when only Ohmic contacts are employed. Theoretical models suggest the surface adsorbed species accumulate or deplete charge from the surface that tunes the SBH and depletion width [21].

However, in the case of single NR piezotronic applications, the contacts are patterned to both ends of the NR side facets in a wrap-around configuration to ensure a strong attachment to the substrate. In this case, the majority of the contact interface is not adjacent to the free NR surface (Fig. 17c). Two similar contacts are formed using the same material (*e.g.* Au, Ag) creating two Schottky contacts that in the equilibrium state do not form overly large potential barriers that can also be modulated by additional charge at the interface induced by mechanical strain as shown in Fig. 20a–c [250]. The exponential relationships that govern electrical transport across a Schottky barrier means that a small differential in the two SBHs induced by piezoelectric polarization results in a large current-voltage rectification. The crystal

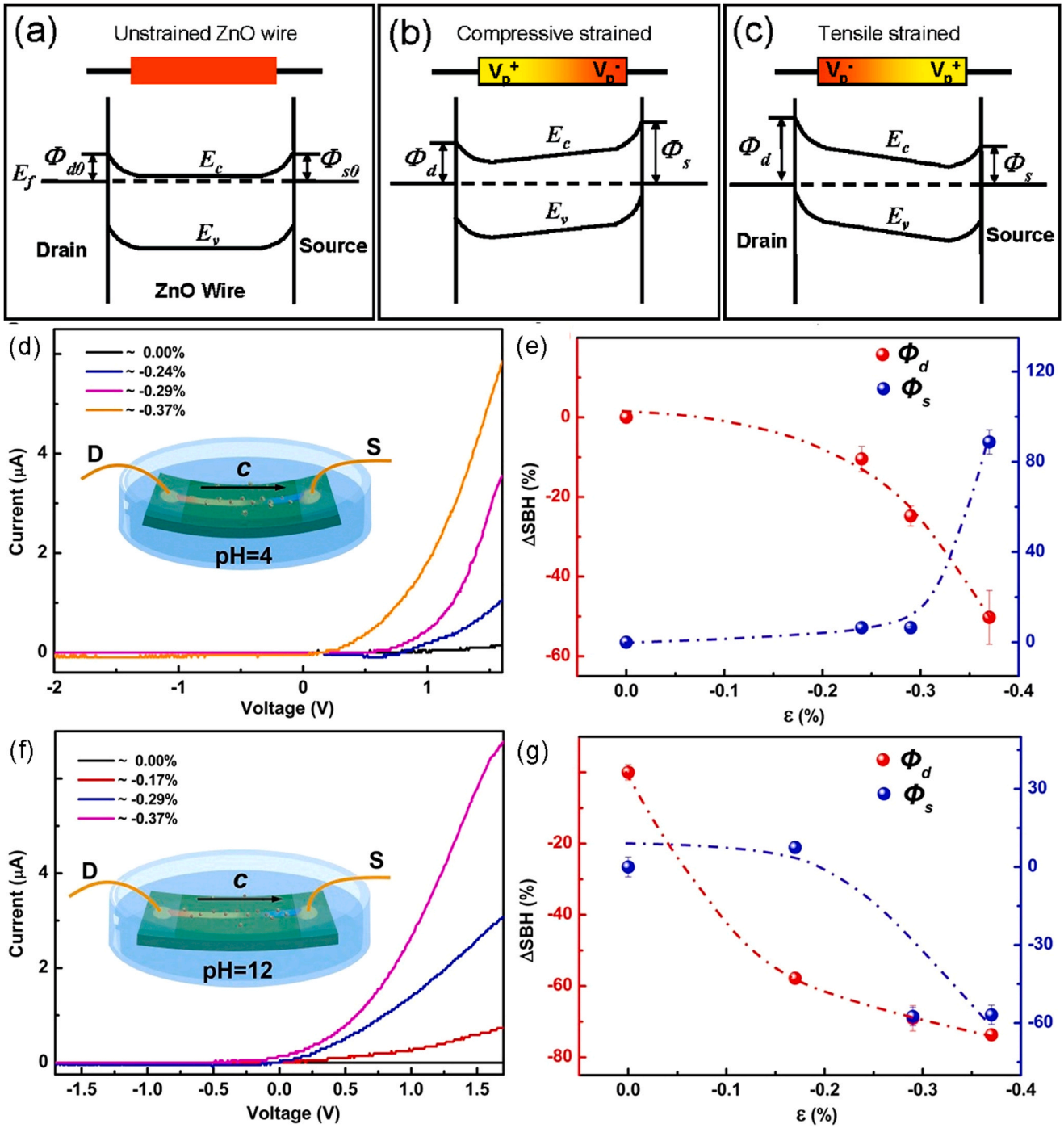

Fig. 20. Band diagrams depicting a single ZnO NR with two Schottky contacts at each end: (a) in the unstrained condition; (b) under compressive strain, a negative piezoelectric potential raises the barrier and positive potential lowers the barrier; (c) tensile strain switches the effect on the barriers. Reprinted with permission from Ref. [250]. Copyright 2008 American Chemical Society. Current-voltage measurements in (d) and (f) from a piezotronic enhanced pH sensor showing the change in output in low and high pH conditions, respectively. The corresponding model of the system revealed in (e) the barrier at the source increases with strain (blue) and decreases at the drain (red) in low pH conditions. (d) In high pH conditions (g) the barrier at the source and drain decreases with strain. Reprinted with permission from Ref. [268]. Copyright 2013 American Chemical Society.

polarity of the NR determines at which contact that a positive or negative piezoelectric charge is generated when under tensile or compressive strain thus the transport properties of the device can be reversed with mechanical deformation. P-n junctions have also been utilized in conjunction with the piezoelectric effect to modulate carrier generation, transportation and recombination. The induced piezoelectric potential alters the band structure at the junction, such that a positive piezoelectric potential decreases the n-type depletion region while increasing it on the p-type side and *vice versa* for a negative piezoelectric potential [269]. This modulates the interaction of charge carriers and photons at the interface and can increase the emission intensity and injection current of NW LEDs [270]. In these devices, the ZnO NR is usually contacted at one end with an Ohmic contact and at the other with a non-piezoelectric p-type material so that the NR polarity should be considered for certain applications that may limit strain to compression or tension.

In further advances, the Schottky contacted piezotronic devices have been applied to enhance single NR sensors by coupling the modulating effect of the piezoelectric potential on the Schottky barriers with surface reactions, as presented in Fig. 20d–g [268]. In traditional NR sensors, the response is determined by the extent of surface depletion or accumulation induced by the surrounding medium or targeted analyte that decreases or increases the signal current. The piezotronic devices build on this by concentrating charged analyte molecules at the oppositely charged contact due to the polarization, which amplifies the effect of strain on the Schottky barrier allowing detection below the usual surface depletion/accumulation limit.

When unequal contacts are formed to either end of a ZnO NR, it is important to know which direction the NR is orientated in order to achieve a piezoelectric enhancement at the correct contact. Qiu et al. showed that contacts fabricated to single cleaved microwires can produce improved Schottky contacts with much greater rectification when a larger contact area and annealing are applied to the freshly cleaved microwire ends [271]. Interpreting the reported results that show current-voltage curves for the contacts applied to both cleaved NR ends, they show an effect of fabricating the Schottky contacts to the O- or Zn-polar surfaces of the same microwire. However, the polarity is not categorically determined and the contacts are fabricated to the entire microwire end and contacting both the polar surface and the side *m*-planes. The results show that the contacts on the cleaved surfaces are not identical, which may indicate some influence of the polar surfaces. In comparison to works on single crystal ZnO (see Section 2.5), they deduce that the greater SBH occurs on the Zn-polar facet. Therefore, we have shown here that when optimizing single NR devices that employ unequal electrical contacts or junctions that consideration of the NR polarity and the polar facets is an important step to achieving reproducible results and maximum performance. Additionally, the variations that are found in polarity-controlled NR properties such as polarity-specific defects and carrier concentration are useful aspects to further optimize devices.

5.3. Further opportunities involving crystal polarity in electrical contacts

Piezoelectric nanogenerators and piezotronic devices typically have four configurations of contacts/junctions as summarized in Fig. 17. In all cases, the function of the p-n junction or Schottky contact is related to the piezoelectric generation, which is dependent upon the NR polarity. Therefore, it is necessary to briefly review the mechanisms at play that control the junctions or contacts, as presented in Fig. 19.

The Schottky contact or p-n junction acts to prevent screening of the piezoelectric potential upon NR deflection by restricting charge leakage when the interface is reverse-biased. A p-n junction also allows efficient electron-hole recombination that can be tuned by the piezoelectric potential. In the case of metal-semiconductor contacts, the (positive or negative) piezoelectric potential generated in the NR changes the electric field at the contact and places the contacts at either end in a state that resembles a lower or higher SBH. This effect switches upon strain reversal and eventually determines the magnitude of current under external bias. In the case of n-type ZnO and depending on the NR polarity, a negative piezoelectric potential from compression or tension is considered to exist in a region near the end NR facet, increasing the negative charge at the interface that increases the electric field at the interface. This, in turn, increases the SBH and depletion region width in addition to uncompensated ionized donor in the NR. A positive piezoelectric potential reduces the SBH and depletion region width. Under an external electric field with a positive bias on the electrode (negative on the semiconductor), the metal Fermi level is lowered relative to the semiconductor and the contact is in forward-bias forming an Ohmic-like junction. The Ohmic nature is increased if the NR is strained such that the piezoelectric potential is positive at the contact. When the free carriers are taken into consideration upon mechanical deformation, a negative piezoelectric potential at one end of the NR induces a migration of charge carriers, increasing the depletion region width [272]. It is apparent that the SBH is affected by the polarity of the interfacial facet and the near-interface defects that differ with polarity-specific growth. Further to this, the depletion region width and the extent of screening are also affected by the carrier concentration that is again related to polarity-specific defects.

Single NR piezotronic devices frequently rely on low quality Schottky contacts that are compatible with flexible substrates and low-cost efficient fabrication that satisfy the need for two equal Schottky barriers with an intermediate height. However, it seems likely, because of the fabrication methods, that interfacial layers have a part to play in the SBH and the piezoelectric-gating effect that can modulate the barrier height. Oxide interfacial layers have been used to act as thin current blocking layers and increase the SBH in piezoelectric nanogenerators minimizing the parasitic screening and charge leakage that reduces the voltage output [274]. Furthermore, thin shell layers have been used in array devices as well-defined and controlled interfacial layers at the NR tips to improve the piezoelectric potential modulation of Schottky barriers and reduce recombination providing an improvement in the photoresponse of strained arrays, as seen in Fig. 21 [273]. Optimized Schottky contacts and interfacial layers can be of substantial benefit to piezoelectric nanogenerators and piezotronic devices [233,275–277]. It is also apparent from the discussion above that, the piezoelectric polarity of the NR determines which NR end determines which contact acts as a Schottky contact and the other as an Ohmic contact on compression or tension. The piezoelectric potential is also screened by the carriers in the NR and it is therefore desirable to reduce donor defects that may originate in the bulk or on the surface but not to a concentration that prevents current flow [193,252,264,278]. For this reason, surface treatments or passivating surface polymers have been shown in piezoelectric nanogenerators to significantly increase open circuit voltage and power density [193,253,279,280]. Therefore, a lower carrier concentration creates a lower screening effect and provides a wider contact depletion region suppressing charge leakage. This dual effect can help maximize the generated potential and, at this stage, it would appear O-polar NRs may satisfy these requirements. Particularly in the case of piezoelectric array devices, well-defined polarity-controlled growth is certainly an opportunity to improve the top contact function, ensure all of the NRs are contributing to the device and to tailor the NR/array properties to maximize the piezoelectric output.

5.4. Applications of piezotronic and piezoelectric devices

Piezoelectric materials have been widely used in the automotive, medical instrument, information and telecommunication industry as sensors, actuators, frequency controlling devices, and high voltage and power sources [281]. The piezoelectric devices based on ZnO NW arrays are currently divided into two main categories using the direct piezoelectric effect: i) the piezoelectric nanogenerators aim at harvesting the energy from the environments to power multifunctional wireless,

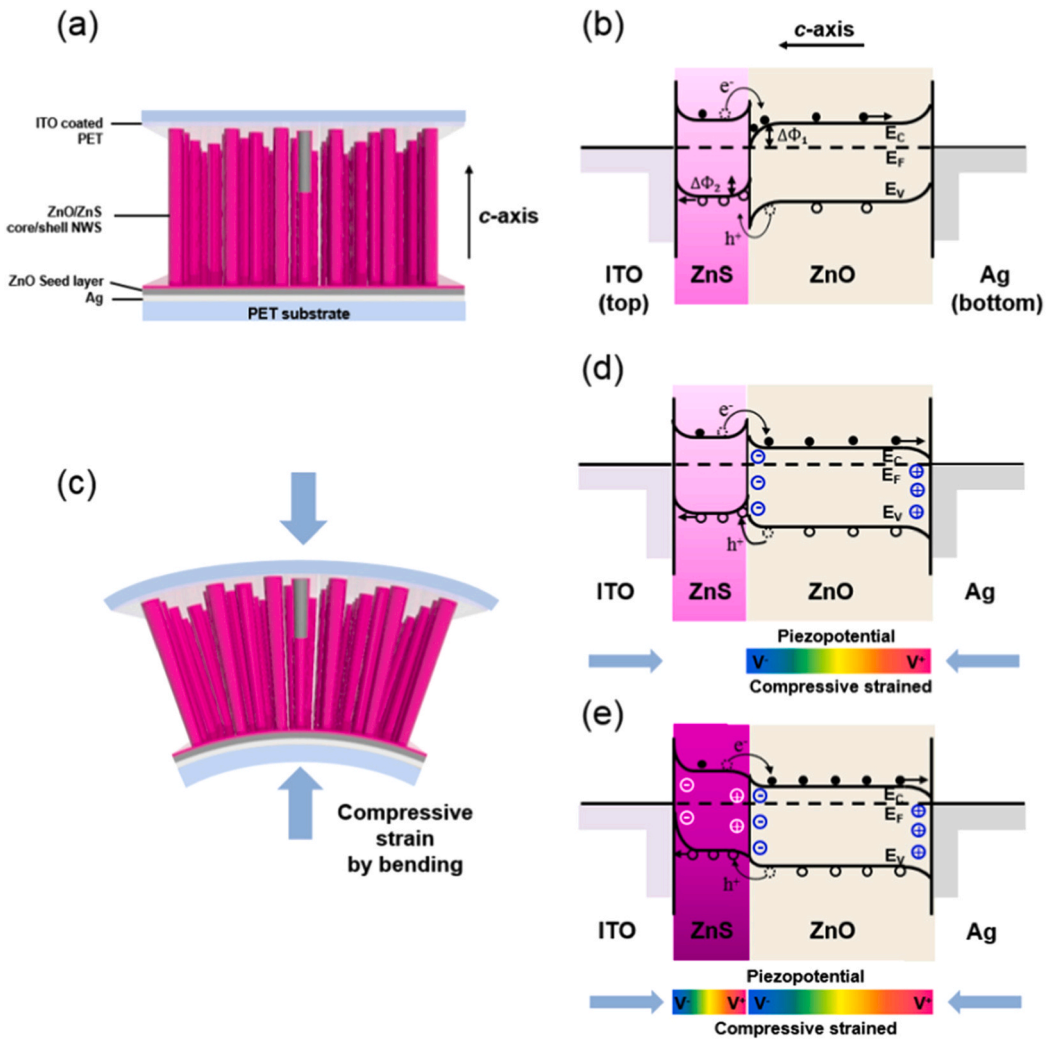

Fig. 21. (a) Schematic diagram of a flexible ZnO NW piezoelectric nanogenerator device with a deposited ZnS shell. (b) Band diagram showing the ITO top contact, ZnS interfacial layer, ZnO NWs and Ag bottom contact. (c) Schematic diagram depicting the compression of the array with associated band diagrams when the ZnS has a zinc blende structure in (d) and piezoelectric wurtzite structure in (e). Reprinted with permission from Ref. [273]. Copyright 2018 American Chemical Society.

wearable nanodevices without any battery and thus act as micro-source of energy to fabricate self-powered nano-systems, while ii) the piezoelectric stress/strain sensors aim at detecting/measuring a signal in different environments [18,282,283]. The use of ZnO NW arrays within the VING configuration has been applied in many piezoelectric devices to convert biomechanical energy (*e.g.* muscle movement [284], bending and stretching action of the skin [285], normal breath and heartbeat [286]), mechanical energy (*e.g.* vehicle tire as in Fig. 22a [287,288]), vibrational energy (*e.g.* sound as in Fig. 22b [289]), and hydraulic energy (gentle wind [30], vortex motion in the atmosphere [29]) into electrical energy for power supply. In the field of automotive, a ZnO NW-based piezoelectric nanogenerator was integrated into a vehicle tire whose deformation was simulated by periodical tightening, harvesting the mechanical energy to an output power density of 70 $\mu W/cm^3$ that was able to light a LCD screen [287]. A flexible, transparent ZnO NW-based piezoelectric nanogenerator using polydimethylsiloxane (PDMS) as a substrate was then integrated into a road surface and produced a stable output power density of 5.3 mW/cm^3 under the rolling vehicle tire, as presented in Fig. 22a [288]. The vibrational energy related to the ambient sound coming from the speech, music, and noise (*e.g.* passing vehicles close to highways) has also been identified as a potential source of energy. A ZnO NW-based piezoelectric nanogenerator using sapphire as a substrate was found to generate an output voltage of about 50 mV when exposed to an input sound with an intensity of 100 dB (*i.e.* 10^{-2} W/m^2 at 100 Hz), as shown in Fig. 22b [289]. The phase shift between the input and output signals was attributed to the impedance of the intrinsic capacitance and reactance inside the circuit. In another field, the electric output of a ZnO NW-based piezoelectric nanogenerator with a record voltage of 58 V and a power density 0.78 W/cm^3 was connected to the sciatic nerve of a frog to induce innervation [290]. The integration of ZnO NW-based piezoelectric nanogenerators connected in parallel and serial into biological fluid environment was achieved using flexible waterproof packaging, leading to the generation of a significant power under high frequency ultrasonic waves, as presented in Fig. 22c [291]. This has opened the way for their implementation into human blood and tissues or into any biological fluid. The integration of a ZnO NW-based piezoelectric nanogenerator into Kevlar 129 textile fibers as shown in Fig. 22d has also been reported to harvest the light-wind energy and body-movement energy at low frequency (*i.e.* < 10 Hz) [292]. Such an integration benefited from the versatile characteristic of the CBD process and has opened the door for the development of smart textiles involving ZnO NWs. The environmental effects on the working of piezoelectric nanogenerators and future strategies to improve their performances have been reviewed in Refs. [293,294]. Compact hybrid cells with synergetic effects simultaneously harvesting the mechanical and solar energy *via* the combination of ZnO NW-based dye-sensitized solar cells sensitive to sunlight with piezoelectric nanogenerators sensitive to ultrasonic waves have further been

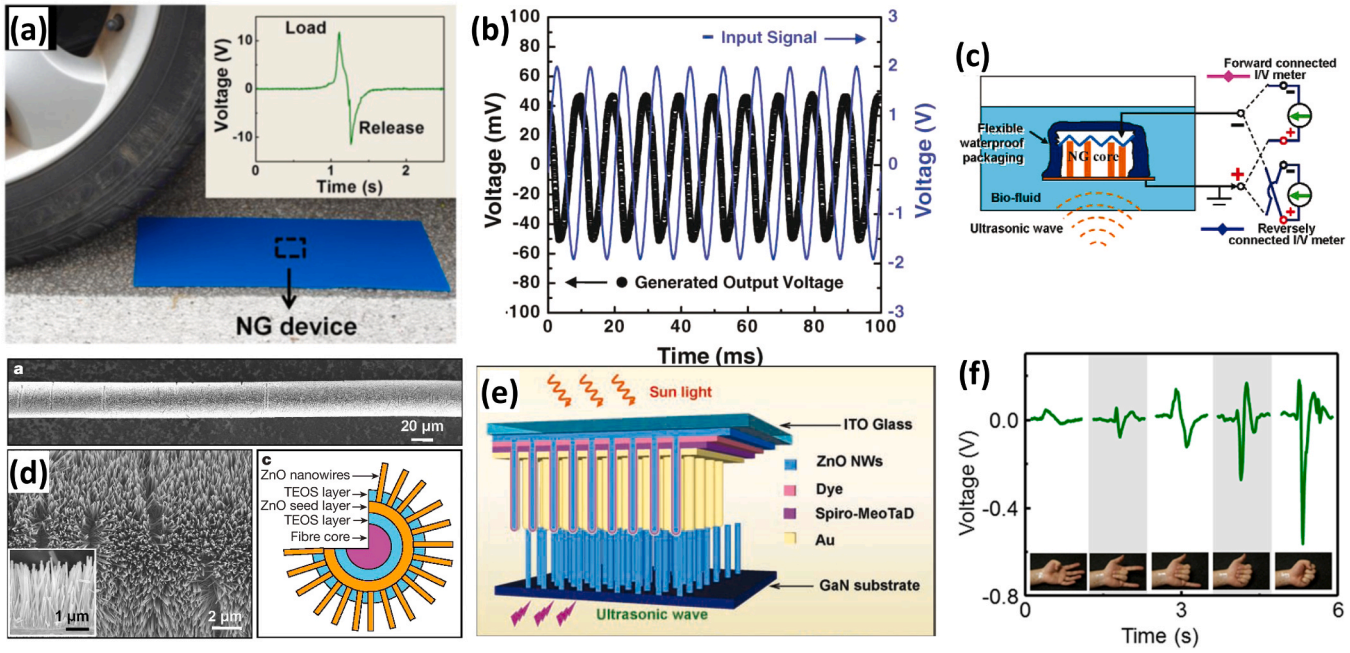

Fig. 22. (a) The photograph showing the experimental setup for harvesting energy under the rolling of the vehicle tire. The ZnO NW-based piezoelectric nanogenerator device was fixed on the road by inserting it between two polystyrene plates. The inset shows a typical output voltage peak induced by the loading and unloading of the vehicle tire. Reprinted with permission from Ref. [288]. Copyright 2013 Elsevier. (b) The input signal for the generation of a sound wave and the output voltage from the ZnO NW-based piezoelectric nanogenerator due to the sound wave. Reprinted with permission from Ref. [289]. Copyright 2010 Wiley & Sons. (c) Schematic of a ZnO NW-based piezoelectric nanogenerator that operates in a biological fluid with the two types of connections used to characterize its performance. The pink and blue solid lines represent signals from forward connected current/voltage meter and reversely connected current/voltage meter, respectively. Reprinted with permission from Ref. [291]. Copyright 2007 American Chemical Society. (d) SEM image of a Kevlar fiber covered with ZnO NW arrays along the radial direction. Higher magnification SEM image and a cross-section image (inset) of the fiber, showing the distribution of ZnO NWs. Diagram showing the cross-sectional structure of the TEOS-enhanced fiber, designed for improved mechanical performance. Reprinted with permission from Ref. [292]. Copyright 2008 Nature Publishing. (e) Schematic illustration of a compact hybrid cell, which is illuminated by sunlight from the top and excited by ultrasonic waves from the bottom. The ITO layer on the dye-sensitized solar cell part and GaN substrate on the piezoelectric nanogenerator part are defined as the cathode and anode of the compact hybrid cell, respectively. Reprinted with permission from Ref. [296]. Copyright 2011 Wiley & Sons. (f) ZnO NW-based piezoelectric sensor grown on silicone rubber for gesture recognition by measurement of flexor movement. The output voltage of the device was measured as a function of the difference in flexion of the fingers. Reprinted with permission from Ref. [304]. Copyright 2014 American Chemical Society.

fabricated to supply more power, as represented in Fig. 22e [295,296]. The output power density was shown to be increased by operating the dye-sensitized solar cell under ultrasonic waves. The development of hybrid cells in one single device was also demonstrated following the architecture of organic solar cells involving ZnO NWs [297]. A dedicated review has been reported in Ref. [298]. ZnO NW arrays have further been integrated into a wide variety of sensors, including ambient wind-velocity detection [29], vibration detection [299], weight detection and measurement system [31], vehicle speed detection [288], humidity sensing [300], tactile sensing for biomimetic robots [301,302], fingerprint sensing [258,303], human face wrinkling detection [30], and gesture recognition (Fig. 22f) [304] to name a few. Some of these sensors are included in the broader scope of electronic skin [305]. For instance, a flexible, wearable-on-skin ZnO NW-based piezoelectric sensor made of a p-n homojunction using Sb p-type doping [236] on polyethylene terephthalate (PET) as a substrate was conformably settled on a human wrist, where each movement of the flexor tendons was distinguished from the different recorded electrical signals, as shown in Fig. 22f [304]. The present gesture recognition has opened the way for the development of human-machine interfacing made of ZnO NWs.

The development of piezotronic effect-based devices, in which the free charge carrier transport is modulated by the piezoelectric potential acting as a gate in strained ZnO NW-based transistors has received an overwhelming interest in the past thirteen years [18,306]. The fabrication of a broad range of piezotronic effect-based devices have been performed, such as strain sensors (Fig. 23a) [307], force and tactile sensors using vertically-integrated strain-gated transistors (Fig. 23b) [308,309], data storage devices (Fig. 23c) [310,311], pH sensors [268], oxygen sensors [312], glucose and protein sensors [313,314], and temperature sensors (Fig. 23d) [315] to name a few. A flexible strain sensor involving a single ZnO NW lying on the outer surface of a polystyrene substrate and contacted at its two ends *via* a two terminal metal-semiconductor-metal structure resulted in the strain-dependent current/voltage characteristics reported in Fig. 23a [307]. The change of current/voltage characteristics in the planar strain-gated piezotronic transistor was related to the modulation of SBH linearly scaling with the strain magnitude. In that sense, the piezotronic effect coming from the piezoelectric polarization of nonmobile ions is due to an asymmetric interface effect at the device terminals, which strongly contrasts the piezoresistive effect in the dedicated transistor. The suppression of the wrap gate in the vertically-integrated strain-gated piezotronic transistor as compared to the field-effect transistor represented in Fig. 23b is consequently a strong asset to simplify the technological integration of vertical ZnO NWs [309]. The present approach was demonstrated by fabricating a taxel-addressable matrix made of strain-gated piezotronic transistors based on vertical ZnO NWs for force and tactile sensors. In the planar strain-gated piezotronic transistor configuration made of ZnO NWs lying on an outer surface and contacted at the two ends, a resistive switching device was fabricated where the hysteretic current/voltage characteristic depends on the strain state and magnitude as shown in Fig. 23c [311]. Notably, the threshold switching voltages were found to be drastically affected by the strain state and magnitude. In an alternative vertically-integrated piezotronic transistor configuration where both contacts are placed at the top (and not at the bottom and top), a

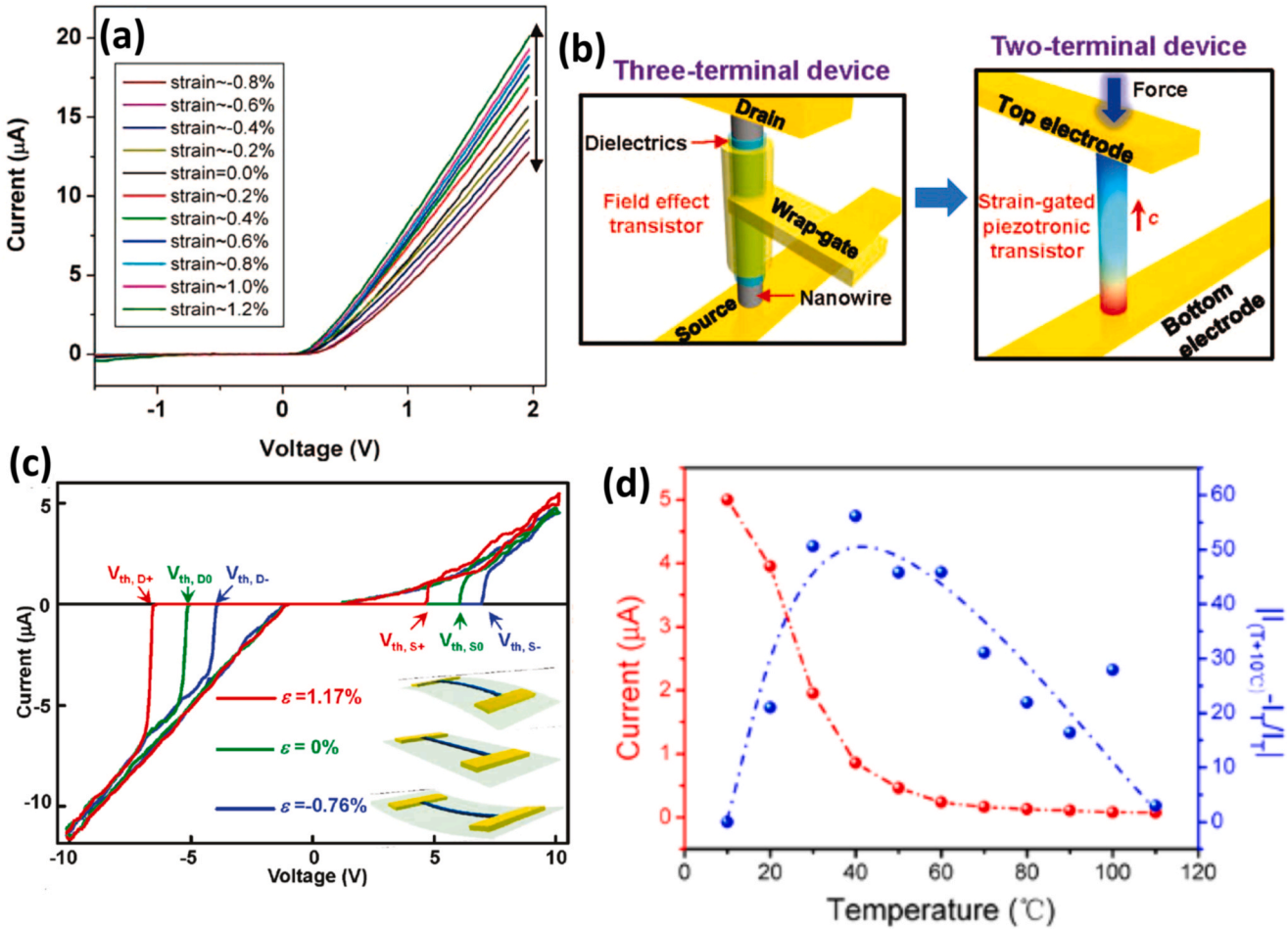

Fig. 23. (a) Typical current/voltage characteristics of the ZnO NW-based strain sensor at different strains. Reprinted with permission from Ref. [307]. Copyright 2008 American Chemical Society. (b) Comparison between three-terminal voltage-gated ZnO NW field effect transistor (left) and two-terminal strain gated ZnO NW vertical piezotronic transistor, in which the color gradient represents the strain-induced piezoelectric potential field where red and blue color indicates positive and negative values, respectively. Reprinted with permission from Ref. [309]. Copyright 2013 The American Association for the Advancement of Science. (c) Current/voltage characteristics of ZnO NW-based piezoelectrically modulated resistive memory cell under tensile, zero, and compressive strains, respectively. Reprinted with permission from Ref. [311]. Copyright 2011 American Chemical Society. (d) Response and relative current change of the ZnO NW-based sensor to the temperature varying from 10 °C to 110 °C. Reprinted with permission from Ref. [315]. Copyright 2014 American Chemical Society.

temperature sensor was fabricated by transferring vertical ZnO NWs embedded in epoxy on a deformable bimetallic strip. The response of the temperature sensor was measured at the fixed bias of 6 V as presented in Fig. 23d, where the current strongly decreases as the temperature is raised to 110 °C [315]. The relative current change follows a parabola trend and reaches a value of about 50% in the temperature range of 30–70 °C. The combination of piezoelectric/piezotronic effect with the light has, in the past decade, open further new perspectives in the emerging field of piezophototronic effect-based devices [272,316].

6. Conclusions

The wurtzite structure of ZnO with its polar and piezoelectric characteristic offers numerous advantages for piezotronic and piezoelectric applications, especially when it is grown with the shape of NWs. Besides its compatibility with the fabrication of flexible devices, the CBD technique also provides the ability to select the O- or Zn-polarity of the resultant NWs, as an additional tunable parameter that should be carefully taken into account. After introducing the basic principles involving crystal polarity in ZnO, we have reviewed the important consequences of the effects of polarity on the nucleation and growth mechanisms of NWs using CBD, defect incorporation and doping, electrical contacts and device properties. Overall, we have revealed that polarity has a strong influence on many processes and properties, which still need further clarification owing to their complex, intricate nature. A couple of guidelines have additionally been emphasized regarding the way to benefit from polarity in ZnO NWs in any optimization study. Eventually, a great improvement of the performance of the related piezotronic and piezoelectric devices should be achieved by more precisely controlling and using the polarity in ZnO NWs.

Declaration of Competing Interest

The authors declare that they have no known competing financial interests or personal relationships that could have appeared to influence the work reported in this paper.

Acknowledgments

V.C. gratefully thanks the financial support from the French National Research Agency through the projects ROLLER (ANR-17-CE09-0033) and DOSETTE (ANR-17-CE24-0003). Funding by the Institut Carnot Energies Du Futur and by the LabEx MINOS under the contract ANR-10-LABX-55-01 are also acknowledged. This work has further been partially supported by the French National Research Agency in the framework of the "Investissements d'avenir" program (ANR-15-IDEX-02) through the project CDP NEED. A.L.

would like to thank the support of the Sêr Cymru II fellowship scheme part-funded by the European Regional Development Fund through the Welsh Government. This work was supported by the Centre for Nanohealth, Swansea University, UK. Support was provided by the Engineering and Physical Sciences Research Council-funded Impact Acceleration Account (grant number EP/R511614/1).

References

[1] C. Noguera, Polar oxide surfaces, J. Phys. Condens. Matter 12 (31) (2000) R367–R410, https://doi.org/10.1088/0953-8984/12/31/201.
[2] J. Goniakowski, F. Finocchi, C. Noguera, Polarity of oxide surfaces and nanostructures, Rep. Prog. Phys. 71 (1) (2007), 016501, https://doi.org/10.1088/0034-4885/71/1/016501.
[3] J. Zuniga-Perez, V. Consonni, L. Lymperakis, X. Kong, A. Trampert, S. Fernandez-Garrido, O. Brandt, H. Renevier, S. Keller, K. Hestroffer, M.R. Wagner, J. S. Reparaz, F. Akyol, S. Rajan, S. Rennesson, T. Palacios, G. Feuillet, Polarity in GaN and ZnO: theory, measurement, growth, and devices, Appl. Phys. Rev. 3 (4) (2016), 041303, https://doi.org/10.1063/1.4963919.
[4] C. Noguera, J. Goniakowski, Polarity in oxide nano-objects, Chem. Rev. 113 (6) (2013) 4073–4105, https://doi.org/10.1021/cr3003032.
[5] M. de la Mata, R.R. Zamani, S. Marti-Sanchez, M. Eickhoff, Q.H. Xiong, A.F. I. Morral, P. Caroff, J. Arbiol, The role of polarity in nonplanar semiconductor nanostructures, Nano Lett. 19 (6) (2019) 3396–3408, https://doi.org/10.1021/acs.nanolett.9b00459.
[6] X.Y. Kong, Z.L. Wang, Spontaneous polarization-induced nanohelixes, nanosprings, and nanorings of piezoelectric nanobelts, Nano Lett. 3 (12) (2003) 1625–1631, https://doi.org/10.1021/nl034463p.
[7] Z.L. Wang, Nanostructures of zinc oxide, Mater. Today 7 (6) (2004) 26–33, https://doi.org/10.1016/S1369-7021(04)00286-X.
[8] Z.L. Wang, X.Y. Kong, J.M. Zuo, Induced growth of asymmetric nanocantilever arrays on polar surfaces, Phys. Rev. Lett. 91 (18) (2003), 185502, https://doi.org/10.1103/PhysRevLett.91.185502.
[9] Z.L. Wang, Zinc oxide nanostructures: growth, properties and applications, J. Phys. Condens. Matter 16 (25) (2004) R829–R858, https://doi.org/10.1088/0953-8984/16/25/r01.
[10] L. Schmidt-Mende, J.L. MacManus-Driscoll, ZnO – nanostructures, defects, and devices, Mater. Today 10 (5) (2007) 40–48, https://doi.org/10.1016/s1369-7021(07)70078-0.
[11] F. Glas, Critical dimensions for the plastic relaxation of strained axial heterostructures in free-standing nanowires, Phys. Rev. B 74 (12) (2006), 121302, https://doi.org/10.1103/PhysRevB.74.121302.
[12] M. Diarra, Y.M. Niquet, C. Delerue, G. Allan, Ionization energy of donor and acceptor impurities in semiconductor nanowires: importance of dielectric confinement, Phys. Rev. B 75 (4) (2007), 045301, https://doi.org/10.1103/PhysRevB.75.045301.
[13] W. Fan, H. Xu, A.L. Rosa, T. Frauenheim, R.Q. Zhang, First-principles calculations of reconstructed [0001] ZnO nanowires, Phys. Rev. B 76 (7) (2007), 073302, https://doi.org/10.1103/PhysRevB.76.073302.
[14] M. Willander, O. Nur, Q.X. Zhao, L.L. Yang, M. Lorenz, B.Q. Cao, J.Z. Perez, C. Czekalla, G. Zimmermann, M. Grundmann, A. Bakin, A. Behrends, M. Al-Suleiman, A. El-Shaer, A.C. Mofor, B. Postels, A. Waag, N. Boukos, A. Travlos, H. S. Kwack, J. Guinard, D.L. Dang, Zinc oxide nanorod based photonic devices: recent progress in growth, light emitting diodes and lasers, Nanotechnology 20 (33) (2009), 332001, https://doi.org/10.1088/0957-4484/20/33/332001.
[15] W. Tian, H. Lu, L. Li, Nanoscale ultraviolet photodetectors based on onedimensional metal oxide nanostructures, Nano Res. 8 (2) (2015) 382–405, https://doi.org/10.1007/s12274-014-0661-2.
[16] V. Consonni, J. Briscoe, E. Karber, X. Li, T. Cossuet, ZnO nanowires for solar cells: a comprehensive review, Nanotechnology 30 (36) (2019), 362001, https://doi.org/10.1088/1361-6528/ab1f2e.
[17] L. Zhu, W. Zeng, Room-temperature gas sensing of ZnO-based gas sensor: a review, Sens. Actuators A Phys. 267 (2017) 242–261, https://doi.org/10.1016/j.sna.2017.10.021.
[18] Z.L. Wang, Towards self-powered nanosystems: from nanogenerators to nanopiezotronics, Adv. Funct. Mater. 18 (22) (2008) 3553–3567, https://doi.org/10.1002/adfm.200800541.
[19] H.D. Espinosa, R.A. Bernal, M. Minary-Jolandan, A review of mechanical and electromechanical properties of piezoelectric nanowires, Adv. Mater. 24 (34) (2012) 4656–4675, https://doi.org/10.1002/adma.201104810.
[20] J. Briscoe, S. Dunn, Piezoelectric nanogenerators – a review of nanostructured piezoelectric energy harvesters, Nano Energy 14 (2015) 15–29, https://doi.org/10.1016/j.nanoen.2014.11.059.
[21] C.F. Pan, J.Y. Zhai, Z.L. Wang, Piezotronics and piezo-phototronics of third generation semiconductor nanowires, Chem. Rev. 119 (15) (2019) 9303–9359, https://doi.org/10.1021/acs.chemrev.8b00599.
[22] H.J. Xiang, J.L. Yang, J.G. Hou, Q.S. Zhu, Piezoelectricity in ZnO nanowires: a first-principles study, Appl. Phys. Lett. 89 (22) (2006), 223111, https://doi.org/10.1063/1.2397013.
[23] R. Agrawal, H.D. Espinosa, Giant piezoelectric size effects in zinc oxide and gallium nitride nanowires. A first principles investigation, Nano Lett. 11 (2) (2011) 786–790, https://doi.org/10.1021/nl104004d.
[24] R. Tao, M. Mouis, G. Ardila, Unveiling the influence of surface fermi level pinning on the piezoelectric response of semiconducting nanowires, Adv. Electron. Mater. 4 (1) (2018), 1700299, https://doi.org/10.1002/aelm.201700299.
[25] C. Falconi, Piezoelectric nanotransducers, Nano Energy 59 (2019) 730–744, https://doi.org/10.1016/j.nanoen.2019.03.027.
[26] Z.L. Wang, J.H. Song, Piezoelectric nanogenerators based on zinc oxide nanowire arrays, Science 312 (5771) (2006) 242–246, https://doi.org/10.1126/science.1124005.
[27] X.D. Wang, J.H. Song, J. Liu, Z.L. Wang, Direct-current nanogenerator driven by ultrasonic waves, Science 316 (5821) (2007) 102–105, https://doi.org/10.1126/science.1139366.
[28] S. Xu, Y. Qin, C. Xu, Y.G. Wei, R.S. Yang, Z.L. Wang, Self-powered nanowire devices, Nat. Nanotechnol. 5 (5) (2010) 366–373, https://doi.org/10.1038/nnano.2010.46.
[29] R. Zhang, L. Lin, Q.S. Jing, W.Z. Wu, Y. Zhang, Z.X. Jiao, L. Yan, R.P.S. Han, Z. L. Wang, Nanogenerator as an active sensor for vortex capture and ambient wind-velocity detection, Energy Environ. Sci. 5 (9) (2012) 8528–8533, https://doi.org/10.1039/c2ee22354f.
[30] S. Lee, S.H. Bae, L. Lin, Y. Yang, C. Park, S.W. Kim, S.N. Cha, H. Kim, Y.J. Park, Z. L. Wang, Super-flexible nanogenerator for energy harvesting from gentle wind and as an active deformation sensor, Adv. Funct. Mater. 23 (19) (2013) 2445–2449, https://doi.org/10.1002/adfm.201202867.
[31] L. Lin, Q.S. Jing, Y. Zhang, Y.F. Hu, S.H. Wang, Y. Bando, R.P.S. Han, Z.L. Wang, An elastic-spring-substrated nanogenerator as an active sensor for self-powered balance, Energy Environ. Sci. 6 (4) (2013) 1164–1169, https://doi.org/10.1039/c3ee00107e.
[32] K. Gupta, S. Brahma, J. Dutta, B. Rao, C.P. Liu, Recent progress in microstructure development of inorganic one-dimensional nanostructures for enhancing performance of piezotronics and piezoelectric nanogenerators, Nano Energy 55 (2019) 1–21, https://doi.org/10.1016/j.nanoen.2018.10.056.
[33] F.R. Fan, W. Tang, Z.L. Wang, Flexible nanogenerators for energy harvesting and self-powered electronics, Adv. Mater. 28 (22) (2016) 4283–4305, https://doi.org/10.1002/adma.201504299.
[34] B.D. Yao, Y.F. Chan, N. Wang, Formation of ZnO nanostructures by a simple way of thermal evaporation, Appl. Phys. Lett. 81 (4) (2002) 757–759, https://doi.org/10.1063/1.1495878.
[35] S.C. Lyu, Y. Zhang, C.J. Lee, H. Ruh, H.J. Lee, Low-temperature growth of ZnO nanowire array by a simple physical vapor-deposition method, Chem. Mater. 15 (17) (2003) 3294–3299, https://doi.org/10.1021/cm020465j.
[36] Y. Sun, G.M. Fuge, M.N.R. Ashfold, Growth of aligned ZnO nanorod arrays by catalyst-free pulsed laser deposition methods, Chem. Phys. Lett. 396 (2004) 21–26, https://doi.org/10.1016/j.cplett.2004.07.110.
[37] T. Nobis, E.M. Kaidashev, A. Rahm, M. Lorenz, J. Lenzner, M. Grundmann, Spatially inhomogeneous impurity distribution in ZnO micropillars, Nano Lett. 4 (5) (2004) 797–800, https://doi.org/10.1021/nl049889y.
[38] J.J. Wu, S.C. Liu, Low-temperature growth of well-aligned ZnO nanorods by chemical vapor deposition, Adv. Mater. 14 (3) (2002) 215–218, https://doi.org/10.1002/1521-4095(20020205)14:3<215::aid-adma215>3.0.co;2-j.
[39] M. Krunks, T. Dedova, I. Oja Açik, Spray pyrolysis deposition of zinc oxide nanostructured layers, Thin Solid Films 515 (3) (2006) 1157–1160, https://doi.org/10.1016/j.tsf.2006.07.134.
[40] W.I. Park, G.C. Yi, M.Y. Kim, S.J. Pennycook, ZnO nanoneedles grown vertically on Si substrates by non-catalytic vapor-phase epitaxy, Adv. Mater. 14 (24) (2002) 1841–1843, https://doi.org/10.1002/adma.200290015.
[41] L. Vayssieres, K. Keis, S.E. Lindquist, A. Hagfeldt, Purpose-built anisotropic metal oxide material: 3D highly oriented microrod array of ZnO, J. Phys. Chem. B 105 (17) (2001) 3350–3352, https://doi.org/10.1021/jp010026s.
[42] S. Peulon, D. Lincot, Cathodic electrodeposition from aqueous solution of dense or open-structured zinc oxide films, Adv. Mater. 8 (2) (1996) 166–170, https://doi.org/10.1002/adma.19960080216.
[43] D. Lincot, Solution growth of functional zinc oxide films and nanostructures, MRS Bull. 35 (10) (2010) 778–789, https://doi.org/10.1557/mrs2010.507.
[44] S. Xu, Z.L. Wang, One-dimensional ZnO nanostructures: solution growth and functional properties, Nano Res. 4 (11) (2011) 1013–1098, https://doi.org/10.1007/s12274-011-0160-7.
[45] P. Anastas, N. Eghbali, Green chemistry: principles and practice, Chem. Soc. Rev. 39 (1) (2010) 301–312, https://doi.org/10.1039/B918763B.
[46] S. Xu, Y. Wei, M. Kirkham, J. Liu, W. Mai, D. Davidovic, R.L. Snyder, Z.L. Wang, Patterned growth of vertically aligned ZnO nanowire arrays on inorganic substrates at low temperature without catalyst, J. Am. Chem. Soc. 130 (45) (2008) 14958–14959, https://doi.org/10.1021/ja806952j.
[47] R. Erdelyi, T. Nagata, D.J. Rogers, F.H. Teherani, Z.E. Horvath, Z. Labadi, Z. Baji, Y. Wakayama, J. Volk, Investigations into the impact of the template layer on ZnO nanowire arrays made using low temperature wet chemical growth, Cryst. Growth Des. 11 (6) (2011) 2515–2519, https://doi.org/10.1021/cg2002755.
[48] Y.G. Wei, W.Z. Wu, R. Guo, D.J. Yuan, S.M. Das, Z.L. Wang, Wafer-scale high-throughput ordered growth of vertically aligned ZnO nanowire arrays, Nano Lett. 10 (9) (2010) 3414–3419, https://doi.org/10.1021/nl1014298.
[49] G. Perillat-Merceroz, R. Thierry, P.H. Jouneau, P. Ferret, G. Feuillet, Compared growth mechanisms of Zn-polar ZnO nanowires on O-polar ZnO and on sapphire, Nanotechnology 23 (12) (2012), 125702, https://doi.org/10.1088/0957-4484/23/12/125702.
[50] V. Consonni, E. Sarigiannidou, E. Appert, A. Bocheux, S. Guillemin, F. Donatini, I. C. Robin, J. Kioseoglou, F. Robaut, Selective area growth of well-ordered ZnO nanowire arrays with controllable polarity, ACS Nano 8 (5) (2014) 4761–4770, https://doi.org/10.1021/nn500620t.

[51] A. Dalcorso, M. Posternak, R. Resta, A. Baldereschi, Ab-initio study of piezoelectricity and spontaneous polarization in ZnO, Phys. Rev. B 50 (15) (1994) 10715–10721, https://doi.org/10.1103/PhysRevB.50.10715.

[52] F. Bernardini, V. Fiorentini, D. Vanderbilt, Spontaneous polarization and piezoelectric constants of III-V nitrides, Phys. Rev. B 56 (16) (1997) 10024–10027, https://doi.org/10.1103/PhysRevB.56.R10024.

[53] M. Catti, Y. Noel, R. Dovesi, Full piezoelectric tensors of wurtzite and zinc blende ZnO and ZnS by first-principles calculations, J. Phys. Chem. Solids 64 (11) (2003) 2183–2190, https://doi.org/10.1016/s0022-3697(03)00219-1.

[54] E.H. Kisi, M.M. Elcombe, u parameters for the wurtzite structure of ZnS and ZnO using powder neutron diffraction, Acta Crystallogr. C 45 (12) (1989) 1867–1870, https://doi.org/10.1107/S0108270189004269.

[55] C.R.A. Catlow, A.M. Stoneham, Ionicity in solids, J. Phys. C Solid State 16 (22) (1983) 4321–4338, https://doi.org/10.1088/0022-3719/16/22/010.

[56] P.W. Tasker, The stability of ionic crystal surfaces, J. Phys. C Solid State 12 (22) (1979) 4977–4984, https://doi.org/10.1088/0022-3719/12/22/036.

[57] T. Cossuet, E. Appert, J.L. Thomassin, V. Consonni, Polarity-dependent growth rates of selective area grown ZnO nanorods by chemical bath deposition, Langmuir 33 (25) (2017) 6269–6279, https://doi.org/10.1021/acs.langmuir.7b00935.

[58] C. Wöll, The chemistry and physics of zinc oxide surfaces, Prog. Surf. Sci. 82 (2) (2007) 55–120, https://doi.org/10.1016/j.progsurf.2006.12.002.

[59] G. Kresse, O. Dulub, U. Diebold, Competing stabilization mechanism for the polar ZnO(0001)-Zn surface, Phys. Rev. B 68 (24) (2003), 245409, https://doi.org/10.1103/PhysRevB.68.245409.

[60] A. Wander, F. Schedin, P. Steadman, A. Norris, R. McGrath, T.S. Turner, G. Thornton, N.M. Harrison, Stability of polar oxide surfaces, Phys. Rev. Lett. 86 (17) (2001) 3811–3814, https://doi.org/10.1103/PhysRevLett.86.3811.

[61] O. Dulub, L.A. Boatner, U. Diebold, STM study of the geometric and electronic structure of ZnO(0001)-Zn, (000-1)-O, (10-10), and (11-20) surfaces, Surf. Sci. 519 (3) (2002) 201–217, https://doi.org/10.1016/s0039-6028(02)02211-2.

[62] O. Dulub, U. Diebold, G. Kresse, Novel stabilization mechanism on polar surfaces: ZnO(0001)-Zn, Phys. Rev. Lett. 90 (1) (2003), 016102, https://doi.org/10.1103/PhysRevLett.90.016102.

[63] J.M. Carlsson, Electronic structure of the polar ZnO{0001}-surfaces, Comput. Mater. Sci. 22 (1–2) (2001) 24–31, https://doi.org/10.1016/s0927-0256(01)00159-8.

[64] W. Gopel, J. Pollmann, I. Ivanov, B. Reihl, Angle-resolved photoemission from polar and non-polar zinc oxide surfaces, Phys. Rev. B 26 (6) (1982) 3144–3150, https://doi.org/10.1103/physrevb.26.3144.

[65] R.T. Girard, O. Tjernberg, G. Chiaia, S. Soderholm, U.O. Karlsson, C. Wigren, H. Nylen, I. Lindau, Electronic structure of ZnO(0001) studied by angle-resolved photoelectron spectroscopy, Surf. Sci. 373 (2–3) (1997) 409–417, https://doi.org/10.1016/s0039-6028(96)01181-8.

[66] A. Calzolari, M. Bazzani, A. Catellani, Dipolar and charge transfer effects on the atomic stabilization of ZnO polar surfaces, Surf. Sci. 607 (2013) 181–186, https://doi.org/10.1016/j.susc.2012.09.004.

[67] S. Torbrugge, F. Ostendorf, M. Reichling, Stabilization of zinc-terminated ZnO (0001) by a modified surface stoichiometry, J. Phys. Chem. C 113 (12) (2009) 4909–4914, https://doi.org/10.1021/jp804026v.

[68] D. Mora-Fonz, T. Lazauskas, M.R. Farrow, C.R.A. Catlow, S.M. Woodley, A. A. Sokol, Why are polar surfaces of ZnO stable? Chem. Mater. 29 (12) (2017) 5306–5320, https://doi.org/10.1021/acs.chemmater.7b01487.

[69] R. Wahl, J.V. Lauritsen, F. Besenbacher, G. Kresse, Stabilization mechanism for the polar ZnO(0001¯)-O surface, Phys. Rev. B 87 (8) (2013), 085313, https://doi.org/10.1103/PhysRevB.87.085313.

[70] J.V. Lauritsen, S. Porsgaard, M.K. Rasmussen, M.C.R. Jensen, R. Bechstein, K. Meinander, B.S. Clausen, S. Helveg, R. Wahl, G. Kresse, F. Besenbacher, Stabilization principles for polar surfaces of ZnO, ACS Nano 5 (7) (2011) 5987–5994, https://doi.org/10.1021/nn2017606.

[71] M. Valtiner, M. Todorova, G. Grundmeier, J. Neugebauer, Temperature stabilized surface reconstructions at polar ZnO(0001), Phys. Rev. Lett. 103 (6) (2009), 065502, https://doi.org/10.1103/PhysRevLett.103.065502.

[72] M. Valtiner, S. Borodin, G. Grundmeier, Preparation and characterisation of hydroxide stabilised ZnO(0001)–Zn–OH surfaces, Phys. Chem. Chem. Phys. 9 (19) (2007) 2406–2412, https://doi.org/10.1039/B617600C.

[73] T. Becker, S. Hövel, M. Kunat, C. Boas, U. Burghaus, C. Wöll, Interaction of hydrogen with metal oxides: the case of the polar ZnO(0001) surface, Surf. Sci. 486 (3) (2001) L502–L506, https://doi.org/10.1016/S0039-6028(01)01120-7.

[74] B. Meyer, First-principles study of the polar O-terminated ZnO surface in thermodynamic equilibrium with oxygen and hydrogen, Phys. Rev. B 69 (4) (2004), 045416, https://doi.org/10.1103/PhysRevB.69.045416.

[75] K. Ozawa, K. Mase, Comparison of the surface electronic structures of H-adsorbed ZnO surfaces: an angle-resolved photoelectron spectroscopy study, Phys. Rev. B 83 (12) (2011), 125406, https://doi.org/10.1103/PhysRevB.83.125406.

[76] V. Staemmler, K. Fink, B. Meyer, D. Marx, M. Kunat, S.G. Girol, U. Burghaus, C. Woll, Stabilization of polar ZnO surfaces: validating microscopic models by using CO as a probe molecule, Phys. Rev. Lett. 90 (10) (2003), 106102, https://doi.org/10.1103/PhysRevLett.90.106102.

[77] H. Zhou, H. Alves, D.M. Hofmann, W. Kriegseis, B.K. Meyer, G. Kaczmarczyk, A. Hoffmann, Behind the weak excitonic emission of ZnO quantum dots: ZnO/Zn$(OH)_2$ core-shell structure, Appl. Phys. Lett. 80 (2) (2002) 210–212, https://doi.org/10.1063/1.1432763.

[78] N.S. Norberg, D.R. Gamelin, Influence of surface modification on the luminescence of colloidal ZnO nanocrystals, J. Phys. Chem. B 109 (44) (2005) 20810–20816, https://doi.org/10.1021/jp0535285.

[79] K.H. Tam, C.K. Cheung, Y.H. Leung, A.B. Djurisic, C.C. Ling, C.D. Beling, S. Fung, W.M. Kwok, W.K. Chan, D.L. Phillips, L. Ding, W.K. Ge, Defects in ZnO nanorods prepared by a hydrothermal method, J. Phys. Chem. B 110 (42) (2006) 20865–20871, https://doi.org/10.1021/jp063239w.

[80] A.B. Djurisic, Y.H. Leung, K.H. Tam, Y.F. Hsu, L. Ding, W.K. Ge, Y.C. Zhong, K. S. Wong, W.K. Chan, H.L. Tam, K.W. Cheah, W.M. Kwok, D.L. Phillips, Defect emissions in ZnO nanostructures, Nanotechnology 18 (9) (2007), 095702, https://doi.org/10.1088/0957-4484/18/9/095702.

[81] A. Wander, N.M. Harrison, An ab initio study of ZnO(10-10), Surf. Sci. 457 (1–2) (2000) L342–L346, https://doi.org/10.1016/s0039-6028(00)00418-0.

[82] B. Meyer, D. Marx, Density-functional study of the structure and stability of ZnO surfaces, Phys. Rev. B 67 (3) (2003), 035403, https://doi.org/10.1103/PhysRevB.67.035403.

[83] C.G. Tang, M.J.S. Spencer, A.S. Barnard, Activity of ZnO polar surfaces: an insight from surface energies, Phys. Chem. Chem. Phys. 16 (40) (2014) 22139–22144, https://doi.org/10.1039/c4cp03221g.

[84] S.H. Na, C.H. Park, First-principles study of the surface energy and the atom cohesion of wurtzite ZnO and ZnS – implications for nanostructure formation, J. Korean Phys. Soc. 56 (1) (2010) 498–502, https://doi.org/10.3938/jkps.56.498.

[85] K. Sun, H.Y. Su, W.X. Li, Stability of polar ZnO surfaces studied by pair potential method and local energy density method, Theor. Chem. Acc. 133 (1) (2013) 1427, https://doi.org/10.1007/s00214-013-1427-8.

[86] M. Kunat, S.G. Girol, U. Burghaus, C. Woll, The interaction of water with the oxygen-terminated, polar surface of ZnO, J. Phys. Chem. B 107 (51) (2003) 14350–14356, https://doi.org/10.1021/jp030675z.

[87] M. Schiek, K. Al-Shamery, M. Kunat, F. Traeger, C. Woll, Water adsorption on the hydroxylated H-(1x1) O-ZnO(0001) surface, Phys. Chem. Chem. Phys. 8 (13) (2006) 1505–1512, https://doi.org/10.1039/b515418a.

[88] A. Onsten, D. Stoltz, P. Palmgren, S. Yu, M. Gothelid, U.O. Karlsson, Water adsorption on ZnO(0001): transition from triangular surface structures to a disordered hydroxyl terminated phase, J. Phys. Chem. C 114 (25) (2010) 11157–11161, https://doi.org/10.1021/jp1004677.

[89] M. Iachella, J. Cure, M.D. Rouhani, Y. Chabal, C. Rossi, A. Esteve, Water dissociation and further hydroxylation of perfect and defective polar ZnO model surfaces, J. Phys. Chem. C 122 (38) (2018) 21861–21873, https://doi.org/10.1021/acs.jpcc.8b04967.

[90] A. Degen, M. Kosec, Effect of pH and impurities on the surface charge of zinc oxide in aqueous solution, J. Eur. Ceram. Soc. 20 (6) (2000) 667–673, https://doi.org/10.1016/s0955-2219(99)00203-4.

[91] G.A. Parks, The isoelectric points of solid oxides, solid hydroxides, and aqueous hydroxo complex systems, Chem. Rev. 65 (2) (1965) 177–198, https://doi.org/10.1021/cr60234a002.

[92] M. Kosmulski, The pH dependent surface charging and points of zero charge. VIII. Update, Adv. Colloid Interface Sci. 275 (2020), 102064, https://doi.org/10.1016/j.cis.2019.102064.

[93] M. Valtiner, S. Borodin, G. Grundmeier, Stabilization and acidic dissolution mechanism of single-crystalline ZnO(0001) surfaces in electrolytes studied by in-situ AFM imaging and ex-situ LEED, Langmuir 24 (10) (2008) 5350–5358, https://doi.org/10.1021/la7037697.

[94] C. Kunze, M. Valtiner, R. Michels, K. Huber, G. Grundmeier, Self-localization of polyacrylic acid molecules on polar ZnO(0001)-Zn surfaces, Phys. Chem. Chem. Phys. 13 (28) (2011) 12959–12967, https://doi.org/10.1039/c1cp20913b.

[95] D.C. Grahame, The electrical double layer and the theory of electrocapillarity, Chem. Rev. 41 (3) (1947) 441–501, https://doi.org/10.1021/cr60130a002.

[96] R. Heinhold, G.T. Williams, S.P. Cooil, D.A. Evans, M.W. Allen, Influence of polarity and hydroxyl termination on the band bending at ZnO surfaces, Phys. Rev. B 88 (23) (2013), 235315, https://doi.org/10.1103/PhysRevB.88.235315.

[97] M.W. Allen, C.H. Swartz, T.H. Myers, T.D. Veal, C.F. McConville, S.M. Durbin, Bulk transport measurements in ZnO: the effect of surface electron layers, Phys. Rev. B 81 (7) (2010), 075211, https://doi.org/10.1103/PhysRevB.81.075211.

[98] A.M. Lord, J.E. Evans, C.J. Barnett, M.W. Allen, A.R. Barron, S.P. Wilks, Surface sensitivity of four-probe STM resistivity measurements of bulk ZnO correlated to XPS, J. Phys. Condens. Matter 29 (38) (2017), 384001, https://doi.org/10.1088/1361-648X/aa7dc8.

[99] O. Schmidt, A. Geis, P. Kiesel, C.G. Van de Walle, N.M. Johnson, A. Bakin, A. Waag, G.H. Dohler, Analysis of a conducting channel at the native zinc oxide surface, Superlattices Microstruct. 39 (1–4) (2006) 8–16, https://doi.org/10.1016/j.spmi.2005.08.056.

[100] A.R. McNeill, A.R. Hyndman, R.J. Reeves, A.J. Downard, M.W. Allen, Tuning the band bending and controlling the surface reactivity at polar and nonpolar surfaces of ZnO through phosphonic acid binding, ACS Appl. Mater. Interfaces 8 (45) (2016) 31392–31402, https://doi.org/10.1021/acsami.6b10309.

[101] A.M. Hyland, R.A. Makin, S.M. Durbin, M.W. Allen, Giant improvement in the rectifying performance of oxidized Schottky contacts to ZnO, J. Appl. Phys. 121 (2) (2017), 024501, https://doi.org/10.1063/1.4973487.

[102] L.J. Brillson, H.L. Mosbacker, M.J. Hetzer, Y. Strzhemechny, G.H. Jessen, D. C. Look, G. Cantwell, J. Zhang, J.J. Song, Dominant effect of near-interface native point defects on ZnO Schottky barriers, Appl. Phys. Lett. 90 (10) (2007), 102116, https://doi.org/10.1063/1.2711536.

[103] L.J. Brillson, H.L. Mosbacker, D.L. Doutt, Y. Dong, Z.Q. Fang, D.C. Look, G. Cantwell, J. Zhang, J.J. Song, Nanoscale depth-resolved cathodoluminescence spectroscopy of ZnO surfaces and metal interfaces, Superlattices Microstruct. 45 (4) (2009) 206–213, https://doi.org/10.1016/j.spmi.2008.11.008.

[104] M.W. Allen, R.J. Mendelsberg, R.J. Reeves, S.M. Durbin, Oxidized noble metal Schottky contacts to n-type ZnO, Appl. Phys. Lett. 94 (10) (2009), 103508, https://doi.org/10.1063/1.3089871.
[105] D.B. Suyatin, V. Jain, V.A. Nebol'sin, J. Trägårdh, M.E. Messing, J.B. Wagner, O. Persson, R. Timm, A. Mikkelsen, I. Maximov, L. Samuelson, H. Pettersson, Strong Schottky barrier reduction at Au-catalyst/GaAs-nanowire interfaces by electric dipole formation and Fermi-level unpinning, Nat. Commun. 5 (1) (2014) 3221, https://doi.org/10.1038/ncomms4221.
[106] D. Colleoni, G. Miceli, A. Pasquarello, Fermi-level pinning through defects at GaAs/oxide interfaces: a density functional study, Phys. Rev. B 92 (12) (2015), 125304, https://doi.org/10.1103/PhysRevB.92.125304.
[107] S. Erker, P. Rinke, N. Moll, O.T. Hofmann, Doping dependence of the surface phase stability of polar O-terminated (0001¯) ZnO, New J. Phys. 19 (8) (2017), 083012, https://doi.org/10.1088/1367-2630/aa79e7.
[108] A. Lajn, Hv Wenckstern, M. Grundmann, G. Wagner, P. Barquinha, E. Fortunato, R. Martins, Comparative study of transparent rectifying contacts on semiconducting oxide single crystals and amorphous thin films, J. Appl. Phys. 113 (4) (2013), 044511, https://doi.org/10.1063/1.4789000.
[109] L.J. Brillson, Y. Dong, D. Doutt, D.C. Look, Z.Q. Fang, Massive point defect redistribution near semiconductor surfaces and interfaces and its impact on Schottky barrier formation, Physica B 404 (23) (2009) 4768–4773, https://doi.org/10.1016/j.physb.2009.08.151.
[110] B.J. Coppa, C.C. Fulton, S.M. Kiesel, R.F. Davis, C. Pandarinath, J.E. Burnette, R. J. Nemanich, D.J. Smith, Structural, microstructural, and electrical properties of gold films and Schottky contacts on remote plasma-cleaned, n-type ZnO{0001} surfaces, J. Appl. Phys. 97 (10) (2005), 103517, https://doi.org/10.1063/1.1898436.
[111] H.L. Mosbacker, Y.M. Strzhemechny, B.D. White, P.E. Smith, D.C. Look, D. C. Reynolds, C.W. Litton, L.J. Brillson, Role of near-surface states in ohmic-Schottky conversion of Au contacts to ZnO, Appl. Phys. Lett. 87 (1) (2005), 012102, https://doi.org/10.1063/1.1984089.
[112] M.W. Allen, S.M. Durbin, Influence of oxygen vacancies on Schottky contacts to ZnO, Appl. Phys. Lett. 92 (12) (2008), 122110, https://doi.org/10.1063/1.2894568.
[113] U. Ozgur, Y.I. Alivov, C. Liu, A. Teke, M.A. Reshchikov, S. Dogan, V. Avrutin, S. J. Cho, H. Morkoc, A comprehensive review of ZnO materials and devices, J. Appl. Phys. 98 (4) (2005), 041301, https://doi.org/10.1063/1.1992666.
[114] M.W. Allen, S.M. Durbin, J.B. Metson, Silver oxide Schottky contacts on n-type ZnO, Appl. Phys. Lett. 91 (5) (2007), 053512, https://doi.org/10.1063/1.2768028.
[115] G.M. Foster, H.T. Gao, G. Mackessy, A.M. Hyland, M.W. Allen, B.G. Wang, D. C. Look, L.J. Brillson, Impact of defect distribution on IrOx/ZnO interface doping and Schottky barriers, Appl. Phys. Lett. 111 (10) (2017), 101604, https://doi.org/10.1063/1.4989539.
[116] M.W. Allen, M.M. Alkaisi, S.M. Durbin, Metal Schottky diodes on Zn-polar and O-polar bulk ZnO, Appl. Phys. Lett. 89 (10) (2006), 103520, https://doi.org/10.1063/1.2346137.
[117] Y.F. Dong, Z.Q. Fang, D.C. Look, G. Cantwell, J. Zhang, J.J. Song, L.J. Brillson, Zn- and O-face polarity effects at ZnO surfaces and metal interfaces, Appl. Phys. Lett. 93 (7) (2008), 072111, https://doi.org/10.1063/1.2974983.
[118] Y.F. Dong, Z.Q. Fang, D.C. Look, D.R. Doutt, G. Cantwell, J. Zhang, J.J. Song, L. J. Brillson, Defects at oxygen plasma cleaned ZnO polar surfaces, J. Appl. Phys. 108 (10) (2010), 103718, https://doi.org/10.1063/1.3514102.
[119] H. Tampo, P. Fons, A. Yamada, K.-K. Kim, H. Shibata, K. Matsubara, S. Niki, H. Yoshikawa, H. Kanie, Determination of crystallographic polarity of ZnO layers, Appl. Phys. Lett. 87 (14) (2005), 141904, https://doi.org/10.1063/1.2067689.
[120] D.P. Nicholls, R. Vincent, D. Cherns, Y. Sun, M.N.R. Ashfold, Polarity determination of zinc oxide nanorods by defocused convergent-beam electron diffraction, Philos. Mag. Lett. 87 (6) (2007) 417–421, https://doi.org/10.1080/09500830701203164.
[121] J. Jasinski, D. Zhang, J. Parra, V. Katkanant, V.J. Leppert, Application of channeling-enhanced electron energy-loss spectroscopy for polarity determination in ZnO nanopillars, Appl. Phys. Lett. 92 (9) (2008), 093104, https://doi.org/10.1063/1.2889496.
[122] M. de la Mata, C. Magen, J. Gazquez, M.I.B. Utama, M. Heiss, S. Lopatin, F. Furtmayr, C.J. Fernández-Rojas, B. Peng, J.R. Morante, R. Rurali, M. Eickhoff, A. Fontcuberta i Morral, Q. Xiong, J. Arbiol, Polarity assignment in ZnTe, GaAs, ZnO, and GaN-AlN nanowires from direct dumbbell analysis, Nano Lett. 12 (5) (2012) 2579–2586, https://doi.org/10.1021/nl300840q.
[123] Q.Y. Xu, Y. Wang, Y.G. Wang, X.L. Du, Q.K. Xue, Z. Zhang, Polarity determination of ZnO thin films by electron holography, Appl. Phys. Lett. 84 (12) (2004) 2067–2069, https://doi.org/10.1063/1.1669060.
[124] O. Romanyuk, S. Fernández-Garrido, P. Jiříček, I. Bartoš, L. Geelhaar, O. Brandt, T. Paskova, Non-destructive assessment of the polarity of GaN nanowire ensembles using low-energy electron diffraction and X-ray photoelectron diffraction, Appl. Phys. Lett. 106 (2) (2015), 021602, https://doi.org/10.1063/1.4905651.
[125] A.N. Mariano, R.E. Hanneman, Crystallographic polarity of ZnO crystals, J. Appl. Phys. 34 (2) (1963) 384–388, https://doi.org/10.1063/1.1702617.
[126] J.R. Williams, M. Kobata, I. Pis, E. Ikenaga, T. Sugiyama, K. Kobayashi, N. Ohashi, Polarity determination of wurtzite-type crystals using hard X-ray photoelectron diffraction, Surf. Sci. 605 (13) (2011) 1336–1340, https://doi.org/10.1016/j.susc.2011.04.036.
[127] D.A. Scrymgeour, T.L. Sounart, N.C. Simmons, J.W.P. Hsu, Polarity and piezoelectric response of solution grown zinc oxide nanocrystals on silver, J. Appl. Phys. 101 (1) (2007), 014316, https://doi.org/10.1063/1.2405014.
[128] J. Zuniga-Perez, V. Munoz-Sanjose, E. Palacios-Lidon, J. Colchero, Polarity effects on ZnO films grown along the nonpolar [112¯0] direction, Phys. Rev. Lett. 95 (22) (2005), 226105, https://doi.org/10.1103/PhysRevLett.95.226105.
[129] S. Guillemin, R. Parize, J. Carabetta, V. Cantelli, D. Albertini, B. Gautier, G. Bremond, D.D. Fong, H. Renevier, V. Consonni, Quantitative and simultaneous analysis of the polarity of polycrystalline ZnO seed layers and related nanowires grown by wet chemical deposition, Nanotechnology 28 (9) (2017), 095704, https://doi.org/10.1088/1361-6528/aa5657.
[130] X. Wang, Y. Tomita, O.-H. Roh, M. Ohsugi, S.-B. Che, Y. Ishitani, A. Yoshikawa, Polarity control of ZnO films grown on nitrided c-sapphire by molecular-beam epitaxy, Appl. Phys. Lett. 86 (1) (2005), 011921, https://doi.org/10.1063/1.1846951.
[131] S. Kazuta, Y. Cho, H. Odagawa, M. Kadota, Determination of the polarities of ZnO thin films on polar and nonpolar substrates using scanning nonlinear dielectric microscopy, Jpn. J. Appl. Phys. 39 (2000) 3121–3124, https://doi.org/10.1143/jjap.39.3121.
[132] M.A. Verges, A. Mifsud, C.J. Serna, Formation of rod-like zinc-oxide microcyrstals in homogeneous solutions, J. Chem. Soc. Faraday Trans. 86 (6) (1990) 959–963, https://doi.org/10.1039/ft9908600959.
[133] L.E. Greene, M. Law, J. Goldberger, F. Kim, J.C. Johnson, Y.F. Zhang, R. J. Saykally, P.D. Yang, Low-temperature wafer-scale production of ZnO nanowire arrays, Angew. Chem. Int. Ed. 42 (26) (2003) 3031–3034, https://doi.org/10.1002/anie.200351461.
[134] H.E. Unalan, P. Hiralal, N. Rupesinghe, S. Dalal, W.I. Milne, G.A.J. Amaratunga, Rapid synthesis of aligned zinc oxide nanowires, Nanotechnology 19 (25) (2008), 255608, https://doi.org/10.1088/0957-4484/19/25/255608.
[135] J.J. Richardson, F.F. Lange, Controlling low temperature aqueous synthesis of ZnO. 2. A novel continuous circulation reactor, Cryst. Growth Des. 9 (6) (2009) 2576–2581, https://doi.org/10.1021/cg900083s.
[136] M.N.R. Ashfold, R.P. Doherty, N.G. Ndifor-Angwafor, D.J. Riley, Y. Sun, The kinetics of the hydrothermal growth of ZnO nanostructures, Thin Solid Films 515 (24) (2007) 8679–8683, https://doi.org/10.1016/j.tsf.2007.03.122.
[137] A. Sugunan, H.C. Warad, M. Boman, J. Dutta, Zinc oxide nanowires in chemical bath on seeded substrates: role of hexamine, J. Sol-Gel Sci. Technol. 39 (1) (2006) 49–56, https://doi.org/10.1007/s10971-006-6969-y.
[138] V. Strano, R.G. Urso, M. Scuderi, K.O. Iwu, F. Simone, E. Ciliberto, C. Spinella, S. Mirabella, Double role of HMTA in ZnO nanorods grown by chemical bath deposition, J. Phys. Chem. C 118 (48) (2014) 28189–28195, https://doi.org/10.1021/jp507496a.
[139] R. Parize, J. Garnier, O. Chaix-Pluchery, C. Verrier, E. Appert, V. Consonni, Effects of hexamethylenetetramine on the nucleation and radial growth of ZnO nanowires by chemical bath deposition, J. Phys. Chem. C 120 (9) (2016) 5242–5250, https://doi.org/10.1021/acs.jpcc.6b00479.
[140] K. Govender, D.S. Boyle, P.B. Kenway, P. O'Brien, Understanding the factors that govern the deposition and morphology of thin films of ZnO from aqueous solution, J. Mater. Chem. 14 (16) (2004) 2575–2591, https://doi.org/10.1039/b404784b.
[141] J.J. Richardson, F.F. Lange, Controlling low temperature aqueous synthesis of ZnO. 1. Thermodynamic analysis, Cryst. Growth Des. 9 (6) (2009) 2570–2575, https://doi.org/10.1021/cg900082u.
[142] M.K. Liang, M.J. Limo, A. Sola-Rabada, M.J. Roe, C.C. Perry, New insights into the mechanism of ZnO formation from aqueous solutions of zinc acetate and zinc nitrate, Chem. Mater. 26 (14) (2014) 4119–4129, https://doi.org/10.1021/cm501096p.
[143] K.M. McPeak, M.A. Becker, N.G. Britton, H. Majidi, B.A. Bunker, J.B. Baxter, In situ X-ray absorption near-edge structure spectroscopy of ZnO nanowire growth during chemical bath deposition, Chem. Mater. 22 (22) (2010) 6162–6170, https://doi.org/10.1021/cm102155m.
[144] J. Volk, T. Nagata, R. Erdelyi, I. Barsony, A.L. Toth, I.E. Lukacs, Z. Czigany, H. Tomimoto, Y. Shingaya, T. Chikyow, Highly uniform epitaxial ZnO nanorod arrays for nanopiezotronics, Nanoscale Res. Lett. 4 (7) (2009) 699–704, https://doi.org/10.1007/s11671-009-9302-1.
[145] Y.J. Wu, C.H. Liao, C.Y. Hsieh, P.M. Lee, Y.S. Wei, Y.S. Liu, C.H. Chen, C.Y. Liu, Local electronic structures and polarity of ZnO nanorods grown on GaN substrates, J. Phys. Chem. C 119 (9) (2015) 5122–5128, https://doi.org/10.1021/jp5116542.
[146] S. Xu, C. Lao, B. Weintraub, Z.L. Wang, Density-controlled growth of aligned ZnO nanowire arrays by seedless chemical approach on smooth surfaces, J. Mater. Res. 23 (8) (2008) 2072–2077, https://doi.org/10.1557/jmr.2008.0274.
[147] S.W. Chen, J.M. Wu, Nucleation mechanisms and their influences on characteristics of ZnO nanorod arrays prepared by a hydrothermal method, Acta Mater. 59 (2) (2011) 841–847, https://doi.org/10.1016/j.actamat.2010.09.070.
[148] T. Demes, C. Ternon, F. Morisot, D. Riassetto, M. Legallais, H. Roussel, M. Langlet, Mechanisms involved in the hydrothermal growth of ultra-thin and high aspect ratio ZnO nanowires, Appl. Surf. Sci. 410 (2017) 423–431, https://doi.org/10.1016/j.apsusc.2017.03.086.
[149] L.E. Greene, M. Law, D.H. Tan, M. Montano, J. Goldberger, G. Somorjai, P. D. Yang, General route to vertical ZnO nanowire arrays using textured ZnO seeds, Nano Lett. 5 (7) (2005) 1231–1236, https://doi.org/10.1021/nl050788p.
[150] S. Guillemin, V. Consonni, E. Appert, E. Puyoo, L. Rapenne, H. Roussel, Critical nucleation effects on the structural relationship between ZnO seed layer and nanowires, J. Phys. Chem. C 116 (47) (2012) 25106–25111, https://doi.org/10.1021/jp308643w.
[151] S. Guillemin, L. Rapenne, H. Roussel, E. Sarigiannidou, G. Bremond, V. Consonni, Formation mechanisms of ZnO nanowires: the crucial role of crystal orientation

and polarity, J. Phys. Chem. C 117 (40) (2013) 20738–20745, https://doi.org/10.1021/jp407120j.
[152] T. Cossuet, H. Roussel, J.M. Chauveau, O. Chaix-Pluchery, J.L. Thomassin, E. Appert, V. Consonni, Well-ordered ZnO nanowires with controllable inclination on semipolar ZnO surfaces by chemical bath deposition, Nanotechnology 29 (47) (2018), 475601, https://doi.org/10.1088/1361-6528/aadf62.
[153] R. Parize, J.D. Garnier, E. Appert, O. Chaix-Pluchery, V. Consonni, Effects of polyethylenimine and its molecular weight on the chemical bath deposition of ZnO nanowires, ACS Omega 3 (10) (2018) 12457–12464, https://doi.org/10.1021/acsomega.8b01641.
[154] Y. Sun, D.J. Riley, M.N.R. Ashfold, Mechanism of ZnO nanotube growth by hydrothermal methods on ZnO film-coated Si substrates, J. Phys. Chem. B 110 (31) (2006) 15186–15192, https://doi.org/10.1021/jp062299z.
[155] D. Cherns, Y. Sun, Defect reduction by epitaxial lateral overgrowth of nanorods in ZnO/(0001) sapphire films, Appl. Phys. Lett. 92 (5) (2008), 051909, https://doi.org/10.1063/1.2841707.
[156] Y.K. Sun, D. Cherns, R.P. Doherty, J.L. Warren, P.J. Heard, Reduction of threading dislocations in ZnO/(0001) sapphire film heterostructure by epitaxial lateral overgrowth of nanorods, J. Appl. Phys. 104 (2) (2008), 023533, https://doi.org/10.1063/1.2957082.
[157] J.B. Baxter, F. Wu, E.S. Aydil, Growth mechanism and characterization of zinc oxide hexagonal columns, Appl. Phys. Lett. 83 (18) (2003) 3797–3799, https://doi.org/10.1063/1.1624467.
[158] S. Kabisch, M. Timpel, H. Kirmse, M.A. Gluba, N. Koch, N.H. Nickel, Polarity of pulsed laser deposited ZnO nanostructures, Appl. Phys. Lett. 108 (8) (2016), 083114, https://doi.org/10.1063/1.4942887.
[159] F. Schuster, B. Laumer, R.R. Zamani, C. Magen, J.R. Morante, J. Arbiol, M. Stutzmann, p-GaN/n-ZnO heterojunction nanowires: optoelectronic properties and the role of interface polarity, ACS Nano 8 (5) (2014) 4376–4384, https://doi.org/10.1021/nn406134e.
[160] V. Sallet, C. Sartel, C. Vilar, A. Lusson, P. Galtier, Opposite crystal polarities observed in spontaneous and vapour-liquid-solid grown ZnO nanowires, Appl. Phys. Lett. 102 (18) (2013), 182103, https://doi.org/10.1063/1.4804254.
[161] N. Rathore, D.V.S. Rao, S.K. Sarkar, Growth of a polarity controlled ZnO nanorod array on a glass/FTO substrate by chemical bath deposition, RSC Adv. 5 (36) (2015) 28251–28257, https://doi.org/10.1039/c5ra00023h.
[162] J.E. Boercker, J.B. Schmidt, E.S. Aydil, Transport limited growth of zinc oxide nanowires, Cryst. Growth Des. 9 (6) (2009) 2783–2789, https://doi.org/10.1021/cg900021u.
[163] J.J. Cheng, S.M. Nicaise, K.K. Berggren, S. Gradečak, Dimensional tailoring of hydrothermally grown zinc oxide nanowire arrays, Nano Lett. 16 (1) (2016) 753–759, https://doi.org/10.1021/acs.nanolett.5b04625.
[164] O. Černohorský, J. Grym, H. Faitová, N. Bašinová, Š. Kučerová, R. Yatskiv, J. Veselý, Modeling of solution growth of ZnO hexagonal nanorod arrays in batch reactors, Cryst. Growth Des. 20 (5) (2020) 3347–3357, https://doi.org/10.1021/acs.cgd.0c00144.
[165] C. Lausecker, B. Salem, X. Baillin, V. Consonni, Modeling the elongation of nanowires grown by chemical bath deposition using a predictive approach, J. Phys. Chem. C 123 (48) (2019) 29476–29483, https://doi.org/10.1021/acs.jpcc.9b08958.
[166] W.J. Li, E.W. Shi, W.Z. Zhong, Z.W. Yin, Growth mechanism and growth habit of oxide crystals, J. Cryst. Growth 203 (1–2) (1999) 186–196, https://doi.org/10.1016/s0022-0248(99)00076-7.
[167] L.E. Greene, B.D. Yuhas, M. Law, D. Zitoun, P.D. Yang, Solution-grown zinc oxide nanowires, Inorg. Chem. 45 (19) (2006) 7535–7543, https://doi.org/10.1021/ic0601900.
[168] B. Liu, H.C. Zeng, Hydrothermal synthesis of ZnO nanorods in the diameter regime of 50 nm, J. Am. Chem. Soc. 125 (15) (2003) 4430–4431, https://doi.org/10.1021/ja0299452.
[169] L. Xu, Y. Guo, Q. Liao, J. Zhang, D. Xu, Morphological control of ZnO nanostructures by electrodeposition, J. Phys. Chem. B 109 (28) (2005) 13519–13522, https://doi.org/10.1021/jp051007b.
[170] J.H. Kim, D. Andeen, F.F. Lange, Hydrothermal growth of periodic, single-crystal ZnO microrods and microtunnels, Adv. Mater. 18 (18) (2006) 2453–2457, https://doi.org/10.1002/adma.200600257.
[171] J. Yahiro, T. Kawano, H. Imai, Nanometric morphological variation of zinc oxide crystals using organic molecules with carboxy and sulfonic groups, J. Colloid Interface Sci. 310 (1) (2007) 302–311, https://doi.org/10.1016/j.jcis.2007.01.072.
[172] Z.R. Tian, J.A. Voigt, J. Liu, B. McKenzie, M.J. McDermott, Biomimetic arrays of oriented helical ZnO nanorods and columns, J. Am. Chem. Soc. 124 (44) (2002) 12954–12955, https://doi.org/10.1021/ja0279545.
[173] D.-F. Zhang, L.-D. Sun, J.-L. Yin, C.-H. Yan, R.-M. Wang, Attachment-driven morphology evolvement of rectangular ZnO nanowires, J. Phys. Chem. B 109 (18) (2005) 8786–8790, https://doi.org/10.1021/jp050631l.
[174] Y. Xi, C.G. Hu, X.Y. Han, Y.F. Xiong, P.X. Gao, G.B. Liu, Hydrothermal synthesis of ZnO nanobelts and gas sensitivity property, Solid State Commun. 141 (9) (2007) 506–509, https://doi.org/10.1016/j.ssc.2006.12.016.
[175] Y. Xi, J. Song, S. Xu, R. Yang, Z. Gao, C. Hu, Z.L. Wang, Growth of ZnO nanotube arrays and nanotube based piezoelectric nanogenerators, J. Mater. Chem. 19 (48) (2009) 9260–9264, https://doi.org/10.1039/B917525C.
[176] G. She, X. Zhang, W. Shi, X. Fan, J.C. Chang, Electrochemical/chemical synthesis of highly-oriented single-crystal ZnO nanotube arrays on transparent conductive substrates, Electrochem. Commun. 9 (12) (2007) 2784–2788, https://doi.org/10.1016/j.elecom.2007.09.019.
[177] F. Li, Y. Ding, P. Gao, X. Xin, Z.L. Wang, Single-crystal hexagonal disks and rings of ZnO: low-temperature, large-scale synthesis and growth mechanism, Angew. Chem. Int. Ed. 43 (39) (2004) 5238–5242, https://doi.org/10.1002/anie.200460783.
[178] J.-S. Na, B. Gong, G. Scarel, G.N. Parsons, Surface polarity shielding and hierarchical ZnO nano-architectures produced using sequential hydrothermal crystal synthesis and thin film atomic layer deposition, ACS Nano 3 (10) (2009) 3191–3199, https://doi.org/10.1021/nn900702e.
[179] A.R. Bielinski, E. Kazyak, C.M. Schlepütz, H.J. Jung, K.N. Wood, N.P. Dasgupta, Hierarchical ZnO nanowire growth with tunable orientations on versatile substrates using atomic layer deposition seeding, Chem. Mater. 27 (13) (2015) 4799–4807, https://doi.org/10.1021/acs.chemmater.5b01624.
[180] S.H. Ko, D. Lee, H.W. Kang, K.H. Nam, J.Y. Yeo, S.J. Hong, C.P. Grigoropoulos, H. J. Sung, Nanoforest of hydrothermally grown hierarchical ZnO nanowires for a high efficiency dye-sensitized solar cell, Nano Lett. 11 (2) (2011) 666–671, https://doi.org/10.1021/nl1037962.
[181] Z.R. Tian, J.A. Voigt, J. Liu, B. McKenzie, M.J. McDermott, M.A. Rodriguez, H. Konishi, H. Xu, Complex and oriented ZnO nanostructures, Nat. Mater. 2 (12) (2003) 821–826, https://doi.org/10.1038/nmat1014.
[182] T. Zhang, W. Dong, M. Keeter-Brewer, S. Konar, R.N. Njabon, Z.R. Tian, Site-specific nucleation and growth kinetics in hierarchical nanosyntheses of branched ZnO crystallites, J. Am. Chem. Soc. 128 (33) (2006) 10960–10968, https://doi.org/10.1021/ja0631596.
[183] T.L. Sounart, J. Liu, J.A. Voigt, M. Huo, E.D. Spoerke, B. McKenzie, Secondary nucleation and growth of ZnO, J. Am. Chem. Soc. 129 (51) (2007) 15786–15793, https://doi.org/10.1021/ja071209g.
[184] J.B. Baxter, C.A. Schmuttenmaer, Conductivity of ZnO nanowires, nanoparticles, and thin films using time-resolved terahertz spectroscopy, J. Phys. Chem. B 110 (50) (2006) 25229–25239, https://doi.org/10.1021/jp064399a.
[185] A.M. Lord, T.G. Maffeis, A.S. Walton, D.M. Kepaptsoglou, Q.M. Ramasse, M. B. Ward, J. Koble, S.P. Wilks, Factors that determine and limit the resistivity of high-quality individual ZnO nanowires, Nanotechnology 24 (43) (2013), 435706, https://doi.org/10.1088/0957-4484/24/43/435706.
[186] C. Opoku, A.S. Dahiya, F. Cayrel, G. Poulin-Vittrant, D. Alquier, N. Camara, Fabrication of field-effect transistors and functional nanogenerators using hydrothermally grown ZnO nanowires, RSC Adv. 5 (86) (2015) 69925–69931, https://doi.org/10.1039/c5ra11450k.
[187] T. Cossuet, F. Donatini, A.M. Lord, E. Appert, J. Pernot, V. Consonni, Polarity-dependent high electrical conductivity of ZnO nanorods and its relation to hydrogen, J. Phys. Chem. C 122 (39) (2018) 22767–22775, https://doi.org/10.1021/acs.jpcc.8b07388.
[188] J. Villafuerte, F. Donatini, J. Kioseoglou, E. Sarigiannidou, O. Chaix-Pluchery, J. Pernot, V. Consonni, Zinc vacancy–hydrogen complexes as major defects in ZnO nanowires grown by chemical bath deposition, J. Phys. Chem. C 124 (30) (2020) 16652–16662, https://doi.org/10.1021/acs.jpcc.0c04264.
[189] L. Wang, S. Guillemin, J.M. Chauveau, V. Sallet, F. Jomard, R. Brenier, V. Consonni, G. Bremond, Characterization of carrier concentration in ZnO nanowires by scanning capacitance microscopy, Phys. Status Solidi C 13 (7–9) (2016) 576–580, https://doi.org/10.1002/pssc.201510268.
[190] Y. Gao, Z.L. Wang, Equilibrium potential of free charge carriers in a bent piezoelectric semiconductive nanowire, Nano Lett. 9 (3) (2009) 1103–1110, https://doi.org/10.1021/nl803547f.
[191] G. Romano, G. Mantini, A. Di Carlo, A. D'Amico, C. Falconi, Z.L. Wang, Piezoelectric potential in vertically aligned nanowires for high output nanogenerators, Nanotechnology 22 (46) (2011), 465401, https://doi.org/10.1088/0957-4484/22/46/465401.
[192] R. Hinchet, S. Lee, G. Ardila, L. Montes, M. Mouis, Z.L. Wang, Performance optimization of vertical nanowire-based piezoelectric nanogenerators, Adv. Funct. Mater. 24 (7) (2014) 971–977, https://doi.org/10.1002/adfm.201302157.
[193] G. Tian, D. Xiong, Y.H. Su, T. Yang, Y.Y. Gao, C. Yan, W. Deng, L. Jin, H.T. Zhang, X.Q. Fan, C.M. Wang, W.L. Deng, W.Q. Yang, Understanding the potential screening effect through the discretely structured ZnO nanorods piezo array, Nano Lett. 20 (6) (2020) 4270–4277, https://doi.org/10.1021/acs.nanolett.0c00793.
[194] A. Janotti, C.G. Van de Walle, Fundamentals of zinc oxide as a semiconductor, Rep. Prog. Phys. 72 (12) (2009), 126501, https://doi.org/10.1088/0034-4885/72/12/126501.
[195] M.D. McCluskey, S.J. Jokela, Defects in ZnO, J. Appl. Phys. 106 (7) (2009), 071101, https://doi.org/10.1063/1.3216464.
[196] A. Janotti, C.G. Van de Walle, Native point defects in ZnO, Phys. Rev. B 76 (16) (2007), 165202, https://doi.org/10.1103/PhysRevB.76.165202.
[197] D.Q. Fang, R.Q. Zhang, Size effects on formation energies and electronic structures of oxygen and zinc vacancies in ZnO nanowires: a first-principles study, J. Appl. Phys. 109 (4) (2011), 044306, https://doi.org/10.1063/1.3549131.
[198] B. Deng, A.L. da Rosa, T. Frauenheim, J.P. Xiao, X.Q. Shi, R.Q. Zhang, M.A. Van Hove, Oxygen vacancy diffusion in bare ZnO nanowires, Nanoscale 6 (20) (2014) 11882–11886, https://doi.org/10.1039/c4nr03582h.
[199] K. Watanabe, T. Nagata, S. Oh, Y. Wakayama, T. Sekiguchi, J. Volk, Y. Nakamura, Arbitrary cross-section SEM-cathodoluminescence imaging of growth sectors and local carrier concentrations within micro-sampled semiconductor nanorods, Nat. Commun. 7 (2016) 10609, https://doi.org/10.1038/ncomms10609.
[200] R.M. Sheetz, I. Ponomareva, E. Richter, A.N. Andriotis, M. Menon, Defect-induced optical absorption in the visible range in ZnO nanowires, Phys. Rev. B 80 (19) (2009), 195314, https://doi.org/10.1103/PhysRevB.80.195314.
[201] Y. Song, N. Wang, M.M. Fadlallah, S. Tao, Y. Yang, Z.L. Wang, Defect states contributed nanoscale contact electrification at ZnO nanowires packed film

surfaces, Nano Energy 79 (2021), 105406, https://doi.org/10.1016/j.nanoen.2020.105406.
[202] A.B. Djurisic, Y.H. Leung, Optical properties of ZnO nanostructures, Small 2 (2006) 944–961, https://doi.org/10.1002/smll.200600134.
[203] M. Willander, O. Nur, J.R. Sadaf, M.I. Qadir, S. Zaman, A. Zainelabdin, N. Bano, I. Hussain, Luminescence from zinc oxide nanostructures and polymers and their hybrid devices, Materials 3 (4) (2010) 2643–2667, https://doi.org/10.3390/ma3042643.
[204] N.E. Hsu, W.K. Hung, Y.F. Chen, Origin of defect emission identified by polarized luminescence from aligned ZnO nanorods, J. Appl. Phys. 96 (8) (2004) 4671–4673, https://doi.org/10.1063/1.1787905.
[205] I. Shalish, H. Temkin, V. Narayanamurti, Size-dependent surface luminescence in ZnO nanowires, Phys. Rev. B 69 (24) (2004), 245401, https://doi.org/10.1103/PhysRevB.69.245401.
[206] D. Li, Y.H. Leung, A.B. Djurisic, Z.T. Liu, M.H. Xie, S.L. Shi, S.J. Xu, W.K. Chan, Different origins of visible luminescence in ZnO nanostructures fabricated by the chemical and evaporation methods, Appl. Phys. Lett. 85 (9) (2004) 1601–1603, https://doi.org/10.1063/1.1786375.
[207] F. Fabbri, M. Villani, A. Catellani, A. Calzolari, G. Cicero, D. Calestani, G. Calestani, A. Zappettini, B. Dierre, T. Sekiguchi, G. Salviati, Zn vacancy induced green luminescence on non-polar surfaces in ZnO nanostructures, Sci. Rep. 4 (2014) 5158, https://doi.org/10.1038/srep05158.
[208] O.W. Kennedy, E.R. White, A. Howkins, C.K. Williams, I.W. Boyd, P. A. Warburton, M.S.P. Shaffer, Mapping the origins of luminescence in ZnO nanowires by STEM-CL, J. Phys. Chem. Lett. 10 (3) (2019) 386–392, https://doi.org/10.1021/acs.jpclett.8b03286.
[209] B. Panigrahy, M. Aslam, D.S. Misra, M. Ghosh, D. Bahadur, Defect-related emissions and magnetization properties of ZnO nanorods, Adv. Funct. Mater. 20 (7) (2010) 1161–1165, https://doi.org/10.1002/adfm.200902018.
[210] A. Kushwaha, M. Aslam, Defect induced high photocurrent in solution grown vertically aligned ZnO nanowire array films, J. Appl. Phys. 112 (5) (2012), 054316, https://doi.org/10.1063/1.4749808.
[211] K.M. Wong, Y.G. Fang, A. Devaux, L.Y. Wen, J. Huang, L. De Cola, Y. Lei, Assorted analytical and spectroscopic techniques for the optimization of the defect-related properties in size-controlled ZnO nanowires, Nanoscale 3 (11) (2011) 4830–4839, https://doi.org/10.1039/c1nr10806a.
[212] E.G. Barbagiovanni, R. Reitano, G. Franzo, V. Strano, A. Terrasi, S. Mirabella, Radiative mechanism and surface modification of four visible deep level defect states in ZnO nanorods, Nanoscale 8 (2) (2016) 995–1006, https://doi.org/10.1039/c5nr05122c.
[213] C. Park, J. Lee, W.S. Chang, Geometrical separation of defect states in ZnO nanorods and their morphology-dependent correlation between photoluminescence and photoconductivity, J. Phys. Chem. C 119 (29) (2015) 16984–16990, https://doi.org/10.1021/acs.jpcc.5b04033.
[214] J.W.P. Hsu, D.R. Tallant, R.L. Simpson, N.A. Missert, R.G. Copeland, Luminescent properties of solution-grown ZnO nanorods, Appl. Phys. Lett. 88 (25) (2006), 252103, https://doi.org/10.1063/1.2214137.
[215] S. Anantachaisilp, S.M. Smith, C. Ton-That, T. Osotchan, A.R. Moon, M. R. Phillips, Tailoring deep level surface defects in ZnO nanorods for high sensitivity ammonia gas sensing, J. Phys. Chem. C 118 (46) (2014) 27150–27156, https://doi.org/10.1021/jp5085857.
[216] J.L. Lyons, J.B. Varley, D. Steiauf, A. Janotti, C.G. Van de Walle, First-principles characterization of native-defect-related optical transitions in ZnO, J. Appl. Phys. 122 (3) (2017), 035704, https://doi.org/10.1063/1.4992128.
[217] A.S. Dahiya, S. Boubenia, G. Franzo, G. Poulin-Vittrant, S. Mirabella, D. Alquier, Photoluminescence study of the influence of additive ammonium hydroxide in hydrothermally grown ZnO nanowires, Nanoscale Res. Lett. 13 (2018) 249, https://doi.org/10.1186/s11671-018-2665-4.
[218] C.G. Van de Walle, Hydrogen as a cause of doping in zinc oxide, Phys. Rev. Lett. 85 (5) (2000) 1012–1015, https://doi.org/10.1103/PhysRevLett.85.1012.
[219] A. Janotti, C.G. Van de Walle, Hydrogen multicentre bonds, Nat. Mater. 6 (1) (2007) 44–47, https://doi.org/10.1038/nmat1795.
[220] M.G. Wardle, J.P. Goss, P.R. Briddon, Theory of Fe, Co, Ni, Cu, and their complexes with hydrogen in ZnO, Phys. Rev. B 72 (15) (2005), 155108, https://doi.org/10.1103/PhysRevB.72.155108.
[221] S.Z. Karazhanov, E.S. Marstein, A. Holt, Hydrogen complexes in Zn deficient ZnO, J. Appl. Phys. 105 (3) (2009), 033712, https://doi.org/10.1063/1.3074304.
[222] J. Kossmann, C. Hattig, Investigation of interstitial hydrogen and related defects in ZnO, Phys. Chem. Chem. Phys. 14 (47) (2012) 16392–16399, https://doi.org/10.1039/c2cp42928d.
[223] F. Herklotz, A. Hupfer, K.M. Johansen, B.G. Svensson, S.G. Koch, E.V. Lavrov, Infrared absorption on a complex comprising three equivalent hydrogen atoms in ZnO, Phys. Rev. B 92 (15) (2015), 155203, https://doi.org/10.1103/PhysRevB.92.155203.
[224] Y.K. Frodason, K.M. Johansen, T.S. Bjorheim, B.G. Svensson, A. Alkauskas, Zn vacancy-donor impurity complexes in ZnO, Phys. Rev. B 97 (10) (2018), 104109, https://doi.org/10.1103/PhysRevB.97.104109.
[225] C.C. Lin, H.P. Chen, H.C. Liao, S.Y. Chen, Enhanced luminescent and electrical properties of hydrogen-plasma ZnO nanorods grown on wafer-scale flexible substrates, Appl. Phys. Lett. 86 (18) (2005), 183103, https://doi.org/10.1063/1.1904715.
[226] X.H. Huang, C.B. Tay, Z.Y. Zhan, C. Zhang, L.X. Zheng, T. Venkatesan, S.J. Chua, Universal photoluminescence evolution of solution-grown ZnO nanorods with annealing: important role of hydrogen donor, CrystEngComm 13 (23) (2011) 7032–7036, https://doi.org/10.1039/c1ce05882g.
[227] A. Kushwaha, M. Aslam, Hydrogen-incorporated ZnO nanowire films: stable and high electrical conductivity, J. Phys. D Appl. Phys. 46 (48) (2013), 485104, https://doi.org/10.1088/0022-3727/46/48/485104.
[228] Q. Zhu, C.S. Xie, H.Y. Li, C.Q. Yang, S.P. Zhang, D.W. Zeng, Selectively enhanced UV and NIR photoluminescence from a degenerate ZnO nanorod array film, J. Mater. Chem. C 2 (23) (2014) 4566–4580, https://doi.org/10.1039/c4tc00011k.
[229] V. Gurylev, C.Y. Su, T.P. Perng, Hydrogenated ZnO nanorods with defect-induced visible light-responsive photoelectrochemical performance, Appl. Surf. Sci. 411 (2017) 279–284, https://doi.org/10.1016/j.apsusc.2017.03.146.
[230] X.H. Huang, Z.Y. Zhan, K.P. Pramoda, C. Zhang, L.X. Zheng, S.J. Chua, Correlating the enhancement of UV luminescence from solution-grown ZnO nanorods with hydrogen doping, CrystEngComm 14 (16) (2012) 5163–5165, https://doi.org/10.1039/c2ce25518a.
[231] Z.N. Urgessa, J.R. Botha, M.O. Eriksson, C.M. Mbulanga, S.R. Dobson, S.R. T. Djiokap, K.F. Karlsson, V. Khranovskyy, R. Yakimova, P.O. Holtz, Low temperature near band edge recombination dynamics in ZnO nanorods, J. Appl. Phys. 116 (12) (2014), 123506, https://doi.org/10.1063/1.4896488.
[232] S. Lautenschlaeger, J. Sann, N. Volbers, B.K. Meyer, A. Hoffmann, U. Haboeck, M. R. Wagner, Asymmetry in the excitonic recombinations and impurity incorporation of the two polar faces of homoepitaxially grown ZnO films, Phys. Rev. B 77 (14) (2008), 144108, https://doi.org/10.1103/PhysRevB.77.144108.
[233] A.M. Lord, V. Consonni, T. Cossuet, F. Donatini, S.P. Wilks, Schottky contacts on polarity-controlled vertical ZnO nanorods, ACS Appl. Mater. Interfaces 12 (11) (2020) 13217–13228, https://doi.org/10.1021/acsami.9b23260.
[234] J. Joo, B.Y. Chow, M. Prakash, E.S. Boyden, J.M. Jacobson, Face-selective electrostatic control of hydrothermal zinc oxide nanowire synthesis, Nat. Mater. 10 (8) (2011) 596–601, https://doi.org/10.1038/nmat3069.
[235] X.H. Huang, C. Zhang, C.B. Tay, T. Venkatesan, S.J. Chua, Green luminescence from Cu-doped ZnO nanorods: role of Zn vacancies and negative thermal quenching, Appl. Phys. Lett. 102 (11) (2013), 111106, https://doi.org/10.1063/1.4798240.
[236] F. Wang, J.-H. Seo, D. Bayerl, J. Shi, H. Mi, Z. Ma, D. Zhao, Y. Shuai, W. Zhou, X. Wang, An aqueous solution-based doping strategy for large-scale synthesis of Sb-doped ZnO nanowires, Nanotechnology 22 (22) (2011), 225602, https://doi.org/10.1088/0957-4484/22/22/225602.
[237] C. Cao, X. Xie, Y. Zeng, S. Shi, G. Wang, L. Yang, C.-Z. Wang, S. Lin, Highly efficient and stable p-type ZnO nanowires with piezotronic effect for photoelectrochemical water splitting, Nano Energy 61 (2019) 550–558, https://doi.org/10.1016/j.nanoen.2019.04.098.
[238] C. Verrier, E. Appert, O. Chaix-Pluchery, L. Rapenne, Q. Rafhay, A. Kaminski-Cachopo, V. Consonni, Effects of the pH on the formation and doping mechanisms of ZnO nanowires using aluminum nitrate and ammonia, Inorg. Chem. 56 (21) (2017) 13111–13122, https://doi.org/10.1021/acs.inorgchem.7b01916.
[239] P. Gaffuri, E. Appert, O. Chaix-Pluchery, L. Rapenne, M. Salaun, V. Consonni, The path of gallium from chemical bath into ZnO nanowires: mechanisms of formation and incorporation, Inorg. Chem. 58 (15) (2019) 10269–10279, https://doi.org/10.1021/acs.inorgchem.9b01413.
[240] C. Verrier, E. Appert, O. Chaix-Pluchery, L. Rapenne, Q. Rafhay, A. Kaminski-Cachopo, V. Consonni, Tunable morphology and doping of ZnO nanowires by chemical bath deposition using aluminum nitrate, J. Phys. Chem. C 121 (6) (2017) 3573–3583, https://doi.org/10.1021/acs.jpcc.6b11104.
[241] A. Hassanpour, P. Guo, S. Shen, P. Bianucci, The effect of cation doping on the morphology, optical and structural properties of highly oriented wurtzite ZnO-nanorod arrays grown by a hydrothermal method, Nanotechnology 28 (43) (2017), 435707, https://doi.org/10.1088/1361-6528/aa849d.
[242] A.H. Rakhsha, H. Abdizadeh, E. Pourshaban, M.R. Golobostanfard, V. R. Mastelaro, M. Montazerian, Ag and Cu doped ZnO nanowires: a pH-controlled synthesis via chemical bath deposition, Materialia 5 (2019), 100212, https://doi.org/10.1016/j.mtla.2019.100212.
[243] S. Limpijumnong, S.B. Zhang, S.-H. Wei, C.H. Park, Doping by large-size-mismatched impurities: the microscopic origin of arsenic- or antimony-doped p-type zinc oxide, Phys. Rev. Lett. 92 (15) (2004), 155504, https://doi.org/10.1103/PhysRevLett.92.155504.
[244] J. Briscoe, D.E. Gallardo, S. Dunn, In situ antimony doping of solution-grown ZnO nanorods, Chem. Commun. 10 (2009) 1273–1275, https://doi.org/10.1039/B820797F.
[245] K.C. Pradel, J. Uzuhashi, T. Takei, T. Ohkubo, K. Hono, N. Fukata, Investigation of nanoscale voids in Sb-doped p-type ZnO nanowires, Nanotechnology 29 (33) (2018), 335204, https://doi.org/10.1088/1361-6528/aac8c8.
[246] N. Rathore, S.K. Sarkar, Dopant induced polarity inversion in polar ZnO nanorods, J. Mater. Sci. Mater. Electron. 27 (12) (2016) 12312–12317, https://doi.org/10.1007/s10854-016-5088-y.
[247] W. Qin, J.C. Hon, D.A. Bonnell, Effect of interface atomic structure on the electronic properties of nano-sized metal-oxide interfaces, Nano Lett. 15 (1) (2015) 211–217, https://doi.org/10.1021/nl503389b.
[248] S.N. Lu, J.J. Qi, S. Liu, Z. Zhang, Z.Z. Wang, P. Lin, Q.L. Liao, Q.J. Liang, Y. Zhang, Piezotronic interface engineering on ZnO/Au-based schottky junction for enhanced photoresponse of a flexible self-powered UV detector, ACS Appl. Mater. Interfaces 6 (16) (2014) 14116–14122, https://doi.org/10.1021/am503442c.
[249] X. Wen, W. Wu, Y. Ding, Z.L. Wang, Piezotronic effect in flexible thin-film based devices, Adv. Mater. 25 (24) (2013) 3371–3379, https://doi.org/10.1002/adma.201300296.
[250] J. Zhou, P. Fei, Y.D. Gu, W.J. Mai, Y.F. Gao, R. Yang, G. Bao, Z.L. Wang, Piezoelectric-potential-control led polarity-reversible Schottky diodes and

switches of ZnO wires, Nano Lett. 8 (11) (2008) 3973–3977, https://doi.org/10.1021/nl802497e.
[251] W.H. Han, Y.S. Zhou, Y. Zhang, C.Y. Chen, L. Lin, X. Wang, S.H. Wang, Z.L. Wang, Strain-gated piezotronic transistors based on vertical zinc oxide nanowires, ACS Nano 6 (5) (2012) 3760–3766, https://doi.org/10.1021/nn301277m.
[252] Y. Zhang, Y. Liu, Z.L. Wang, Fundamental theory of piezotronics, Adv. Mater. 23 (27) (2011) 3004–3013, https://doi.org/10.1002/adma.201100906.
[253] P. Lin, X.Q. Yan, Z. Zhang, Y.W. Shen, Y.G. Zhao, Z.M. Bai, Y. Zhang, Self-powered UV photosensor based on PEDOT:PSS/ZnO micro/nanowire with strain-modulated photoresponse, ACS Appl. Mater. Interfaces 5 (9) (2013) 3671–3676, https://doi.org/10.1021/am4008775.
[254] P.X. Gao, J.H. Song, J. Liu, Z.L. Wang, Nanowire piezoelectric nanogenerators on plastic substrates as flexible power sources for nanodevices, Adv. Mater. 19 (1) (2007) 67–72, https://doi.org/10.1002/adma.200601162.
[255] P. Lin, X.Q. Yan, F. Li, J.L. Du, J.J. Meng, Y. Zhang, Polarity-dependent piezotronic effect and controllable transport modulation of ZnO with multifield coupled interface engineering, Adv. Mater. Interfaces 4 (3) (2017), 1600842, https://doi.org/10.1002/admi.201600842.
[256] T. Li, K.Y. Zeng, Probing of local multifield coupling phenomena of advanced materials by scanning probe microscopy techniques, Adv. Mater. 30 (47) (2018), 1803064, https://doi.org/10.1002/adma.201803064.
[257] Y. Zhang, X.Q. Yan, Y. Yang, Y.H. Huang, Q.L. Liao, J.J. Qi, Scanning probe study on the piezotronic effect in ZnO nanomaterials and nanodevices, Adv. Mater. 24 (34) (2012) 4647–4655, https://doi.org/10.1002/adma.201104382.
[258] M. Parmar, E. Perez, G. Ardila, E. Saoutieff, E. Pauliac-Vaujour, M. Mouis, A demonstration of the mechanical sensing capability of individually contacted vertical piezoelectric nanowires arranged in matrices, Nano Energy 56 (2019) 859–867, https://doi.org/10.1016/j.nanoen.2018.11.088.
[259] P.K. Sahoo, G. Mangamma, A. Rajesh, M. Kamruddin, S. Dash, Identification of polar and nonpolar faces in ZnO nanostructures using conductive atomic force microscopy, Ferroelectrics 519 (1) (2017) 157–163, https://doi.org/10.1080/00150193.2017.1361239.
[260] D.A. Scrymgeour, J.W.P. Hsu, Correlated piezoelectric and electrical properties in individual ZnO nanorods, Nano Lett. 8 (8) (2008) 2204–2209, https://doi.org/10.1021/nl080704n.
[261] A.M. Lord, Q.M. Ramasse, D.M. Kepaptsoglou, J.E. Evans, P.R. Davies, M.B. Ward, S.P. Wilks, Modifying the interface edge to control the electrical transport properties of nanocontacts to nanowires, Nano Lett. 17 (2) (2017) 687–694, https://doi.org/10.1021/acs.nanolett.6b03699.
[262] A.M. Lord, T.G. Maffeis, O. Kryvchenkova, R.J. Cobley, K. Kalna, D. M. Kepaptsoglou, Q.M. Rarnasse, A.S. Walton, M.B. Ward, J. Koble, S.P. Wilks, Controlling the electrical transport properties of nanocontacts to nanowires, Nano Lett. 15 (7) (2015) 4248–4254, https://doi.org/10.1021/nl503743t.
[263] A.M. Lord, A.S. Walton, T.G. Maffeis, M.B. Ward, P. Davies, S.P. Wilks, ZnO nanowires with Au contacts characterised in the as-grown real device configuration using a local multi-probe method, Nanotechnology 25 (42) (2014), 425706, https://doi.org/10.1088/0957-4484/25/42/425706.
[264] J. Briscoe, M. Stewart, M. Vopson, M. Cain, P.M. Weaver, S. Dunn, Nanostructured p-n junctions for kinetic-to-electrical energy conversion, Adv. Energy Mater. 2 (10) (2012) 1261–1268, https://doi.org/10.1002/aenm.201200205.
[265] M.Y. Choi, D. Choi, M.J. Jin, I. Kim, S.H. Kim, J.Y. Choi, S.Y. Lee, J.M. Kim, S. W. Kim, Mechanically powered transparent flexible charge-generating nanodevices with piezoelectric ZnO nanorods, Adv. Mater. 21 (21) (2009) 2185–2189, https://doi.org/10.1002/adma.200803605.
[266] J. Zhou, Y.D. Gu, Y.F. Hu, W.J. Mai, P.H. Yeh, G. Bao, A.K. Sood, D.L. Polla, Z. L. Wang, Gigantic enhancement in response and reset time of ZnO UV nanosensor by utilizing Schottky contact and surface functionalization, Appl. Phys. Lett. 94 (19) (2009), 191103, https://doi.org/10.1063/1.3133358.
[267] T.Y. Wei, P.H. Yeh, S.Y. Lu, Z. Lin-Wang, Gigantic enhancement in sensitivity using schottky contacted nanowire nanosensor, J. Am. Chem. Soc. 131 (48) (2009) 17690–17695, https://doi.org/10.1021/ja907585c.
[268] C.F. Pan, R.M. Yu, S.M. Niu, G. Zhu, Z.L. Wang, Piezotronic effect on the sensitivity and signal level of schottky contacted proactive micro/nanowire nanosensors, ACS Nano 7 (2) (2013) 1803–1810, https://doi.org/10.1021/nn306007p.
[269] Y. Liu, S.M. Niu, Q. Yang, B.D.B. Klein, Y.S. Zhou, Z.L. Wang, Theoretical study of piezo-phototronic nano-LEDs, Adv. Mater. 26 (42) (2014) 7209–7216, https://doi.org/10.1002/adma.201402328.
[270] Q. Yang, W.H. Wang, S. Xu, Z.L. Wang, Enhancing light emission of ZnO microwire-based diodes by piezo-phototronic effect, Nano Lett. 11 (9) (2011) 4012–4017, https://doi.org/10.1021/nl202619d.
[271] Y. Qiu, H.Q. Zhang, L.Z. Hu, L.N. Wang, B. Wang, D.C. Yang, G.Q. Liu, J.Y. Ji, X. Liu, J.F. Lin, Y. Lang, F. Li, S.J. Han, Improving the quality of Schottky contacts on ZnO microwires using Cu-contained silver paste electrode, Micro Nano Lett. 7 (6) (2012) 592–595, https://doi.org/10.1049/mnl.2012.0269.
[272] Z.L. Wang, Piezopotential gated nanowire devices: piezotronics and piezo-phototronics, Nano Today 5 (6) (2010) 540–552, https://doi.org/10.1016/j.nantod.2010.10.008.
[273] S. Jeong, M.W. Kim, Y.R. Jo, T.Y. Kim, Y.C. Leem, S.W. Kim, B.J. Kim, S.J. Park, Crystal-structure-dependent piezotronic and piezo-phototronic effects of ZnO/ZnS core/shell nanowires for enhanced electrical transport and photosensing performance, ACS Appl. Mater. Interfaces 10 (34) (2018) 28736–28744, https://doi.org/10.1021/acsami.8b06192.
[274] J.I. Sohn, S.N. Cha, B.G. Song, S. Lee, S.M. Kim, J. Ku, H.J. Kim, Y.J. Park, B. L. Choi, Z.L. Wang, J.M. Kim, K. Kim, Engineering of efficiency limiting free carriers and an interfacial energy barrier for an enhancing piezoelectric generation, Energy Environ. Sci. 6 (1) (2013) 97–104, https://doi.org/10.1039/c2ee23404a.
[275] J.Y. Zheng, Y.L. Zhou, Y.M. Zhang, L.J. Li, Y. Zhang, C-V characteristics of piezotronic metal-insulator-semiconductor transistor, Sci. Bull. 65 (2) (2020) 161–168, https://doi.org/10.1016/j.scib.2019.11.001.
[276] X.Q. Liao, X.Q. Yan, P. Lin, S.G. Lu, Y. Tian, Y. Zhang, Enhanced performance of ZnO piezotronic pressure sensor through electron-tunneling modulation of MgO nano layer, ACS Appl. Mater. Interfaces 7 (3) (2015) 1602–1607, https://doi.org/10.1021/am5070443.
[277] Z. Zhang, Q.L. Liao, Y.H. Yu, X.D. Wang, Y. Zhang, Enhanced photoresponse of ZnO nanorods-based self-powered photodetector by piezotronic interface engineering, Nano Energy 9 (2014) 237–244, https://doi.org/10.1016/j.nanoen.2014.07.019.
[278] J. Liu, P. Fei, J.H. Song, X.D. Wang, C.S. Lao, R. Tummala, Z.L. Wang, Carrier density and Schottky barrier on the performance of DC nanogenerator, Nano Lett. 8 (1) (2008) 328–332, https://doi.org/10.1021/nl0728470.
[279] I. Hussain, M.Y. Soomro, N. Bano, O. Nur, M. Willander, Systematic study of interface trap and barrier inhomogeneities using I-V-T characteristics of Au/ZnO nanorods Schottky diode, J. Appl. Phys. 113 (23) (2013), 234509, https://doi.org/10.1063/1.4810924.
[280] M. Hussain, M.A. Abbasi, Z.H. Ibupoto, O. Nur, M. Willander, The improved piezoelectric properties of ZnO nanorods with oxygen plasma treatment on the single layer graphene coated polymer substrate, Phys. Status Solidi A 211 (2) (2014) 455–459, https://doi.org/10.1002/pssa.201300330.
[281] S.R. Anton, H.A. Sodano, A review of power harvesting using piezoelectric materials (2003–2006), Smart Mater. Struct. 16 (3) (2007) R1–R21, https://doi.org/10.1088/0964-1726/16/3/r01.
[282] Y. Hu, Y. Zhang, C. Xu, L. Lin, R.L. Snyder, Z.L. Wang, Self-powered system with wireless data transmission, Nano Lett. 11 (6) (2011) 2572–2577, https://doi.org/10.1021/nl201505c.
[283] Z. Wang, X. Pan, Y. He, Y. Hu, H. Gu, Y. Wang, Piezoelectric nanowires in energy harvesting applications, Adv. Mater. Sci. Eng. 2015 (2015), 165631, https://doi.org/10.1155/2015/165631.
[284] R. Yang, Y. Qin, C. Li, G. Zhu, Z.L. Wang, Converting biomechanical energy into electricity by a muscle-movement-driven nanogenerator, Nano Lett. 9 (3) (2009) 1201–1205, https://doi.org/10.1021/nl803904b.
[285] T.I. Lee, W.S. Jang, E. Lee, Y.S. Kim, Z.L. Wang, H.K. Baik, J.M. Myoung, Ultrathin self-powered artificial skin, Energy Environ. Sci. 7 (12) (2014) 3994–3999, https://doi.org/10.1039/C4EE02358G.
[286] Z. Li, G. Zhu, R. Yang, A.C. Wang, Z.L. Wang, Muscle-driven in vivo nanogenerator, Adv. Mater. 22 (23) (2010) 2534–2537, https://doi.org/10.1002/adma.200904355.
[287] Y. Hu, C. Xu, Y. Zhang, L. Lin, R.L. Snyder, Z.L. Wang, A nanogenerator for energy harvesting from a rotating tire and its application as a self-powered pressure/speed sensor, Adv. Mater. 23 (35) (2011) 4068–4071, https://doi.org/10.1002/adma.201102067.
[288] L. Lin, Y. Hu, C. Xu, Y. Zhang, R. Zhang, X. Wen, Z. Lin Wang, Transparent flexible nanogenerator as self-powered sensor for transportation monitoring, Nano Energy 2 (1) (2013) 75–81, https://doi.org/10.1016/j.nanoen.2012.07.019.
[289] S.N. Cha, J.-S. Seo, S.M. Kim, H.J. Kim, Y.J. Park, S.-W. Kim, J.M. Kim, Sound-driven piezoelectric nanowire-based nanogenerators, Adv. Mater. 22 (42) (2010) 4726–4730, https://doi.org/10.1002/adma.201001169.
[290] G. Zhu, A.C. Wang, Y. Liu, Y. Zhou, Z.L. Wang, Functional electrical stimulation by nanogenerator with 58 V output voltage, Nano Lett. 12 (6) (2012) 3086–3090, https://doi.org/10.1021/nl300972f.
[291] X. Wang, J. Liu, J. Song, Z.L. Wang, Integrated nanogenerators in biofluid, Nano Lett. 7 (8) (2007) 2475–2479, https://doi.org/10.1021/nl0712567.
[292] Y. Qin, X. Wang, Z.L. Wang, Microfibre–nanowire hybrid structure for energy scavenging, Nature 451 (7180) (2008) 809–813, https://doi.org/10.1038/nature06601.
[293] V. Nguyen, R. Zhu, R. Yang, Environmental effects on nanogenerators, Nano Energy 14 (2015) 49–61, https://doi.org/10.1016/j.nanoen.2014.11.049.
[294] D. Hu, M. Yao, Y. Fan, C. Ma, M. Fan, M. Liu, Strategies to achieve high performance piezoelectric nanogenerators, Nano Energy 55 (2019) 288–304, https://doi.org/10.1016/j.nanoen.2018.10.053.
[295] C. Xu, X. Wang, Z.L. Wang, Nanowire structured hybrid cell for concurrently scavenging solar and mechanical energies, J. Am. Chem. Soc. 131 (16) (2009) 5866–5872, https://doi.org/10.1021/ja810158x.
[296] C. Xu, Z.L. Wang, Compact hybrid cell based on a convoluted nanowire structure for harvesting solar and mechanical energy, Adv. Mater. 23 (7) (2011) 873–877, https://doi.org/10.1002/adma.201003696.
[297] D. Choi, K.Y. Lee, M.-J. Jin, S.-G. Ihn, S. Yun, X. Bulliard, W. Choi, S.Y. Lee, S.-W. Kim, J.-Y. Choi, J.M. Kim, Z.L. Wang, Control of naturally coupled piezoelectric and photovoltaic properties for multi-type energy scavengers, Energy Environ. Sci. 4 (11) (2011) 4607–4613, https://doi.org/10.1039/C1EE02080C.
[298] B. Kumar, S.-W. Kim, Energy harvesting based on semiconducting piezoelectric ZnO nanostructures, Nano Energy 1 (3) (2012) 342–355, https://doi.org/10.1016/j.nanoen.2012.02.001.
[299] A. Yu, P. Jiang, Z. Lin Wang, Nanogenerator as self-powered vibration sensor, Nano Energy 1 (3) (2012) 418–423, https://doi.org/10.1016/j.nanoen.2011.12.006.
[300] D. Zhu, Y. Fu, W. Zang, Y. Zhao, L. Xing, X. Xue, Piezo/active humidity sensing of CeO_2/ZnO and SnO_2/ZnO nanoarray nanogenerators with high response and

large detecting range, Sens. Actuators B Chem. 205 (2014) 12–19, https://doi.org/10.1016/j.snb.2014.08.060.
[301] W. Deng, L. Jin, B. Zhang, Y. Chen, L. Mao, H. Zhang, W. Yang, A flexible field-limited ordered ZnO nanorod-based self-powered tactile sensor array for electronic skin, Nanoscale 8 (36) (2016) 16302–16306, https://doi.org/10.1039/C6NR04057H.
[302] A.S. Dahiya, F. Morini, S. Boubenia, K. Nadaud, D. Alquier, G. Poulin-Vittrant, Organic/inorganic hybrid stretchable piezoelectric nanogenerators for self-powered wearable electronics, Adv. Mater. Technol. 3 (2) (2018), 1700249, https://doi.org/10.1002/admt.201700249.
[303] A. Bouvet-Marchand, A. Graillot, J. Volk, R. Dauksevicius, C. Sturm, M. Grundmann, E. Saoutieff, A. Viana, B. Christian, V. Lebedev, J. Radó, I. E. Lukács, Q.K. N, D. Grosso, C. Loubat, Design of UV-crosslinked polymeric thin layers for encapsulation of piezoelectric ZnO nanowires for pressure-based fingerprint sensors, J. Mater. Chem. C 6 (3) (2018) 605–613, https://doi.org/10.1039/C7TC04153E.
[304] K.C. Pradel, W. Wu, Y. Ding, Z.L. Wang, Solution-derived ZnO homojunction nanowire films on wearable substrates for energy conversion and self-powered gesture recognition, Nano Lett. 14 (12) (2014) 6897–6905, https://doi.org/10.1021/nl5029182.
[305] X. Wang, L. Dong, H. Zhang, R. Yu, C. Pan, Z.L. Wang, Recent progress in electronic skin, Adv. Sci. 2 (10) (2015), 1500169, https://doi.org/10.1002/advs.201500169.
[306] Z.L. Wang, Nanopiezotronics, Adv. Mater. 19 (6) (2007) 889–892, https://doi.org/10.1002/adma.200602918.
[307] J. Zhou, Y. Gu, P. Fei, W. Mai, Y. Gao, R. Yang, G. Bao, Z.L. Wang, Flexible piezotronic strain sensor, Nano Lett. 8 (9) (2008) 3035–3040, https://doi.org/10.1021/nl802367t.
[308] X. Wang, J. Zhou, J. Song, J. Liu, N. Xu, Z.L. Wang, Piezoelectric field effect transistor and nanoforce sensor based on a single ZnO nanowire, Nano Lett. 6 (12) (2006) 2768–2772, https://doi.org/10.1021/nl061802g.
[309] W. Wu, X. Wen, Z.L. Wang, Taxel-addressable matrix of vertical-nanowire piezotronic transistors for active and adaptive tactile imaging, Science 340 (6135) (2013) 952–957, https://doi.org/10.1126/science.1234855.
[310] J. Song, Y. Zhang, C. Xu, W. Wu, Z.L. Wang, Polar charges induced electric hysteresis of ZnO nano/microwire for fast data storage, Nano Lett. 11 (7) (2011) 2829–2834, https://doi.org/10.1021/nl2011966.
[311] W. Wu, Z.L. Wang, Piezotronic nanowire-based resistive switches as programmable electromechanical memories, Nano Lett. 11 (7) (2011) 2779–2785, https://doi.org/10.1021/nl201074a.
[312] S. Niu, Y. Hu, X. Wen, Y. Zhou, F. Zhang, L. Lin, S. Wang, Z.L. Wang, Enhanced performance of flexible ZnO nanowire based room-temperature oxygen sensors by piezotronic effect, Adv. Mater. 25 (27) (2013) 3701–3706, https://doi.org/10.1002/adma.201301262.
[313] R. Yu, C. Pan, J. Chen, G. Zhu, Z.L. Wang, Enhanced performance of a ZnO nanowire-based self-powered glucose sensor by piezotronic effect, Adv. Funct. Mater. 23 (47) (2013) 5868–5874, https://doi.org/10.1002/adfm.201300593.
[314] R. Yu, C. Pan, Z.L. Wang, High performance of ZnO nanowire protein sensors enhanced by the piezotronic effect, Energy Environ. Sci. 6 (2) (2013) 494–499, https://doi.org/10.1039/C2EE23718K.
[315] F. Xue, L. Zhang, W. Tang, C. Zhang, W. Du, Z.L. Wang, Piezotronic effect on ZnO nanowire film based temperature sensor, ACS Appl. Mater. Interfaces 6 (8) (2014) 5955–5961, https://doi.org/10.1021/am500993p.
[316] Z.L. Wang, W. Wu, Piezotronics and piezo-phototronics: fundamentals and applications, Natl. Sci. Rev. 1 (1) (2013) 62–90, https://doi.org/10.1093/nsr/nwt002.

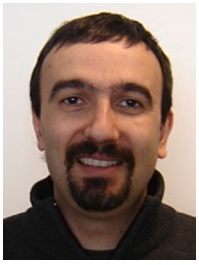

Dr. Vincent Consonni is a Senior Research Scientist in CNRS. He obtained his Ph.D. in Materials Science and Engineering in 2008 from Université Grenoble Alpes after research works carried out in CEA-LETI. He then spent post-doctoral stays in Paul-Drude-Institut in Berlin and in LTM in Grenoble to develop an expertize on semiconducting nanowires. He joined LMGP in Grenoble in 2011, where he leads the NanoMAT team. His research focuses on the development of semiconducting nanowires with a special emphasis on the issues of chemical synthesis, doping, polarity, and related heterostructures for piezoelectric and optoelectronic devices.

Dr. Alex M. Lord received his Ph.D. from Swansea University, UK in 2014. He is a Sêr Cymru II senior research fellow at the Centre for NanoHealth, Swansea University. His research focusses on the physical, electrical, and chemical properties of metal oxide nanomaterials and surfaces, and techniques for measuring these materials at the atomic- and nano-scale.